

Design of Mechanically Stabilized Tire Derived Aggregate (MSTDA) Retaining Walls



California Department of Resources Recycling and Recovery

Spring 2021

Contractor's Report
Prepared By:



University of California, San Diego
Jacobs School of Engineering, Department of Structural Engineering
John S. McCartney, Ph.D., P.E.
CalRecycle DRR #21023, GHD #12561260

STATE OF CALIFORNIA

Edmund G Brown Jr.
Governor


John Laird
Secretary, California Natural Resources Agency

DEPARTMENT OF RESOURCES RECYCLING AND RECOVERY

Caroll Mortensen
Director

Department of Resources Recycling and Recovery
Public Affairs Office
1001 I Street (MS 22-B)
P.O. Box 4025
Sacramento, CA 95812-4025
www.calrecycle.ca.gov/Publications/
1-800-RECYCLE (California only) or (916) 341-6300

Publication # DRR-21023

-  To conserve resources and reduce waste, CalRecycle reports are produced in electronic format only. If printing copies of this document, please consider use of recycled paper containing 100 percent postconsumer fiber and, where possible, please print images on both sides of the paper.

Copyright © 2015 by the California Department of Resources Recycling and Recovery (CalRecycle). All rights reserved. This publication, or parts thereof, may not be reproduced in any form without permission.

Prepared as part of contract number DRR 21023, GHD #12561260

The California Department of Resources Recycling and Recovery (CalRecycle) does not discriminate on the basis of disability in access to its programs. CalRecycle publications are available in accessible formats upon request by calling the Public Affairs Office at (916) 341-6300. Persons with hearing impairments can reach CalRecycle through the California Relay Service, 1-800-735-2929.

Disclaimer: This report was produced under contract by GHD Inc. The statements and conclusions contained in this report are those of the contractor and not necessarily those of the Department of Resources Recycling and Recovery (CalRecycle), its employees, or the State of California and should not be cited or quoted as official Department policy or direction.

The state makes no warranty, expressed or implied, and assumes no liability for the information contained in the succeeding text. Any mention of commercial products or processes shall not be construed as an endorsement of such products or processes.

Design of Mechanically Stabilized Tire Derived Aggregate (MSTDA) Retaining Walls



Department of Structural Engineering
University of California San Diego
Spring 2021

Executive Summary

Waste tires have been used in a variety of forms in civil engineering applications as a lightweight fill, insulation layer, or drainage layer. This approach to recycling and reusing waste tires has significant environmental benefits over other methods of disposal or incineration due to the quantity of waste tires generated by society. Although many civil engineering applications have used waste tire shreds mixed with mineral soils, there are advantages to using shredded tires in monolithic layers. For example, a greater number of waste tires can be recycled when using monolithic layers and there are lower construction costs associated with avoiding mixing with soils. Further, monolithic layers of tire shreds have similar shearing properties to soils, superior thermal insulating properties, excellent drainage, and high damping ratio. When shredded tires are used in a monolithic layer a civil engineering application they are referred to as tire-derived aggregate (TDA). This report focuses on the use of TDA as a backfill material in the construction of internally stabilized retaining walls referred to as “Mechanically Stabilized TDA” or MSTDA retaining walls. The objectives of this report are to present a design methodology for MSTDA retaining walls, guidance on material property selection, and an overview of lessons learned from MSTDA retaining walls recently constructed in California.

The first chapter of this report includes a discussion on the reasons behind using TDA in civil engineering infrastructure, along with examples of successful civil engineering projects using TDA over the past 40 years. This chapter also includes a discussion on the most common type of TDA being used in practice. Specifically, TDA with large particle sizes ranging from 150 to 300 mm (referred to as Type B TDA) has the lowest processing cost and is less susceptible to self-heating. Further, the first chapter also has a discussion on the design constraints placed on the use of TDA to ensure safe long-term performance. Specifically, monolithic layers of TDA should be limited in height and encapsulated with inorganic mineral soil to avoid conditions that could contribute to exothermic reactions. The second chapter summarizes the material properties for TDA needed in the design of MSTDA walls, with a focus on the material properties of Type B TDA. The material properties were determined using a large-scale shearing device developed at the University of California San Diego. Specifically, this device was used for measuring the properties governing internal shear strength of Type B TDA as well as interface shear strength of Type B TDA with concrete, geosynthetic reinforcements, and different types of soils. This device was also used to infer the load-settlement characteristics of Type B TDA and to perform cyclic simple shear tests to measure the secant modulus and damping coefficient. In addition to presenting the material properties of Type B TDA required for the MSTDA design methods, parameters are provided for advanced constitutive models used in finite element analyses. The third chapter summarizes the design methods used to evaluate the internal and external stability of MSTDA walls under both static and seismic conditions, and to understand service limits associated with displacements. These design methods build upon those used for Mechanically Stabilized Earth (MSE) walls, but with considerations for TDA overbuild and compaction along with TDA’s nonlinear stress-dependency. The fourth chapter presents a design example that integrates the properties from the third chapter with the design methodology in the second chapter. The fifth chapter presents the details of several case studies of MSTDA wall projects. While field measurements on the performance of these MSTDA walls are not available, it is useful to learn from the construction strategies used for placement of TDA, internal reinforcements, and retaining wall facing elements. The sixth chapter provides a summary of construction procedures for MSTDA walls.

Table of Contents

Executive Summary	ES-i
Chapter 1: Introduction.....	1
Chapter 2: Review of Engineering Properties of TDA and Interaction with other Materials.....	7
General Characteristics of Type B TDA in MSTDA Walls	7
Compaction and Compression Response of TDA.....	8
Internal and Interface Shear Strength of Type B TDA.....	14
Cyclic Shearing Response of Type B TDA	18
Pullout of Geosynthetic Reinforcements from Type B TDA.....	20
Calibration of Advanced Constitutive Models for Finite Element Modeling	23
Chapter 3: Design Methodology for MSTDA Retaining Walls	27
Overview of MSTDA Design Philosophy.....	27
MSTDA Design Procedure Overview	27
Establishing Initial Project Requirements and Material Parameters	29
Initial MSTDA Design Configuration.....	29
Strength Properties of Geosynthetic Reinforcements.....	31
Pullout of Geosynthetic Reinforcements from TDA and Granular Backfill	32
LRFD Load Factors and Load Combinations	33
External Stability Analysis	35
Sliding.....	36
Limiting Eccentricity	37
Bearing Capacity and Settlement of Subgrade under MSTDA Wall	37
Internal Stability Analysis.....	39
Rupture Check and Vertical Spacing Definition	40
Pullout Check	41
Facing Connection Strength Check	41
Considerations for TDA Compression: Overbuild	42
Drainage in MSTDA Walls	44
Global Stability Analyses	45
Extreme Event (Seismic) Stability Analyses.....	45
Chapter 4: Example Calculations for Design of an MSTDA Retaining Wall.....	49
Chapter 5: Case Histories of MSTDA Retaining Walls in California	59
Case 1: Ortega Ridge Road (Santa Barbara County, CA)	59
Case 2: Italian Bar Road, Site 3 (Tuolumne County, CA)	74
Case 3: Italian Bar Road, Site 6 (Tuolumne County, CA)	83
Chapter 6: Proposed Construction Procedures for MSTDA Walls	91
References.....	93

Tables

Table 2.1: Shear Failure Envelope and Displacement Parameters (Ghaaowd et al. 2017, 2020).....	17
Table 2.2: Geogrid Characteristics used in the Pullout Tests of Ghaaowd and McCartney (2020)	21
Table 2.3: Type B TDA parameters for the modified Duncan-Chang hyperbolic model.....	25
Table 3.1: Suggested Load Factors for MSTDA walls (Berg et al. 2009; AASHTO 2020)	34
Table 4.1: Initial Design Configuration Data for the Wall (Note that the reinforcement length and the gabion length are different than in Figure 4.1 as they were modified during design).....	50
Table 4.2: Overbuild Calculations for the TDA Lifts	51
Table 4.3: Geosynthetic Characteristics.....	52
Table 4.4: Load Factors and Definition of Key Forces	52
Table 4.5: Seismic Characteristics of the Hypothetical MSTDA Wall Location	55
Table 5.1: Material Parameters Used in the Stability Analysis	62
Table 5.2: Global Stability Results for the MSTDA Wall and Surrounding Embankment.....	63

Figures

Figure 1.1: MSTDA configurations considered in this report: (a) Vertical facing; (b) Battered facing	4
Figure 2.1: Particle size range for Type B TDA with actual Type B TDA from Ghaaowd et al. (2020)	7
Figure 2.2: Total Unit Weight of TDA After Applied Vertical Normal Stress: (a) Imperial; (b) Metric	10
Figure 2.3: Compression Curves for Type B TDA: (a) Imperial; (b) Metric.....	11
Figure 2.4: Compression Indices with initial Unit Weight: (a) Compression Index; (b) Recompression Index.....	11
Figure 2.5: Overbuild Chart for TDA (Humphrey 2008, ASTM D6270-20)	12
Figure 2.6: Creep Compression Response of TDA with Small Particle Sizes (Wartman et al. 2007): (a) Range of Vertical Strains Due to Post Construction Creep Observed in the Literature; (b) Comparison of Creep Response of TDA with that of Sand and TDA-Sand Mixtures.....	13
Figure 2.7: Type B TDA Direct Shear Results: (a) Stress Displacement Curves: Imperial; (b) Stress-Displacement Curves: Metric; (c) Secant Friction Angle Mobilization Curves: Imperial; (d) Secant Friction Angle Mobilization Curves: Metric; (e) Volumetric Strain vs. Displacement Curves: Imperial; (f) Volumetric Strain vs. Displacement Curves: Metric	16
Figure 2.8: Shear Failure Envelopes for Internal Type B TDA and Interfaces Between Type B TDA with Different Materials (Ghaaowd et al. 2017, 2020)	17
<i>Note:</i> The symbol ϕ is used for both internal and interface friction angles	17
Figure 2.9: Comparisons Between the Secant Friction Angle and Dilation Angle Measured for Type B TDA Over a Range of Normal Stresses (Ghaaowd et al. 2017): (a) Imperial; (b) Metric.....	18
Figure 2.10: Cyclic Shearing Response of Type B TDA Under Different Vertical Stresses and Cyclic Shear Strain Amplitudes (McCartney et al. 2017): (a) Shear Modulus; (b) Damping Ratio	19
Figure 2.11: Modulus Reduction Curves for Type B TDA (McCartney et al. 2017): (a) Fitted Curves to Measured Data; (b) Normalized Modulus Reduction Curves	20
Figure 2.12: Geogrid pullout force-displacement curves for Type B TDA (Ghaaowd and McCartney 2020): (a) GGA; (b) GGB; (c) GGC	21
Figure 2.13: Maximum Pullout Force vs. Vertical Normal Stress for Different Geogrids in Type B TDA (Ghaaowd and McCartney 2020)	22

Figure 2.14: Synthesized Pullout Test Results (Ghaaowd and McCartney 2020): (a) Pullout Factor for Different Geogrids from Type B TDA as a Function of the Confining Stress; (b) Pullout Displacement at the Peak Pullout Force	23
Figure 2.15: Hyperbolic Model Fitting Results: (a) Stress-Displacement Curves for Type B TDA; (b) Initial Shear Stiffness Values for Type B TDA and Type B TDA-Concrete Interfaces	25
Figure 3.1: Definition of Key Geometric Variables of MSTDA Walls	30
Figure 3.2: Internal Stability Modes in MSTDA Walls	33
Figure 3.3: Definition of Nominal Loads for an MSTDA Wall (same definitions for an MSTDA wall with a batter)	35
Figure 3.4: External Stability Modes for MSTDA walls: (a) Sliding; (b) Limiting Eccentricity; (c) Bearing Capacity; (d) Example of Global Stability (note that the critical failure surface for global stability may also go through the MSTDA wall)	36
Figure 3.5: Compression Curve of Type B TDA from Laboratory Experiments	42
Figure 3.6: Sample Overbuild Calculations for MSTDA Walls with a Maximum TDA Thickness of 3 m and Different Granular Fill Layer Thicknesses: (a) cumulative; (b) Individual Lift Values.....	43
Figure 3.7: Distribution in Final Total Unit Weight of the TDA after Compression Under Overbuild.....	43
Figure 4.1: Initial Configuration of an MSTDA Wall Considered in the Design Example	49
Figure 4.2: Final MSTDA Wall Configuration Accounting for all Design Checks.....	57
Figure 5.1: Map of the Project Location	59
Figure 5.2: Drawing Shown in the Area of Existing Soil Removed	60
Figure 5.3: Drawing Showing the Area Replaced with an MSTDA Wall.....	60
Figure 5.4: General Drawing of the MSTDA Wall.....	61
Figure 5.5: Detailed Drawing of the MSTDA Wall.....	61
Figure 5.6: Gabion Facing Connection Detail.....	61
Figure 5.7: Elevation View of the Wall Height Along the Length of the Road	62
Figure 5.8: Global Stability Analysis Results for Static Conditions Showing the Most Critical Global Failure Surface	63
Figure 5.9: Global Stability Analysis Results for Pseudo-Static Conditions Showing the Most Critical Global Failure Surface	63
Figure 5.10: Overview of Internal Stability Analysis for the Ortega Ridge MSTDA Wall	64
Figure 5.11: Results of Internal Stability Analysis for the Ortega Ridge MSTDA Wall	65
Figure 5.12: Failed Roadway Embankment on Ortega Ridge Road Prior to Remediation.....	65
Figure 5.13: Initial Excavation of the Failed Embankment	66
Figure 5.14: Excavation of the Failed Embankment Material.....	66
Figure 5.15: Placement of TDA Within the Excavation	67
Figure 5.16: Placement of the First Above-Ground Gabion And Preparation of the Reinforcement layer to be stretched across the TDA.....	67
Figure 5.17: Placement of the Second Above-Ground TDA Lift.....	68
Figure 5.18: Picture Showing the Geosynthetic Wrapped Around the Facing while a TDA Lift Is Being Placed By an excavator	68
Figure 5.19: Photo Showing the Compaction of the TDA Using a Vibratory Sheepfoot Roller	69
Figure 5.20: Picture of the Third Above-Ground TDA Lift Being Placed	69
Figure 5.21: Placement of Crushed Rock into the Next Gabion Layer	70
Figure 5.22: Picture of the Separator Geotextile Being Placed Between the Crushed Rock and TDA ...	70
Figure 5.23: Preparation for Geogrid Placement at the Top of a TDA Lift.....	71

Figure 5.24: Picture of a Utility Line Running though the TDA Along with a Highlight of the Separator Geotextile Between the Crushed Rock and TDA, and the Biaxial Geogrid Placed Within the Gabions for Improved Retention of Rock Within the Gabions.....	71
Figure 5.25: Placement of the Fourth Above-Ground TDA Lift and Checks on the Batter of the Gabion Wall Facing	72
Figure 5.26: Final MSTDA Wall at Ortega Ridge Road from the North	72
Figure 5.27: Final MSTDA Wall at Ortega Ridge Road from the South	73
Figure 5.28: Location of Italian Bar Road Site 3 in Tuolumne County, CA	74
Figure 5.29: General Schematic of the MSTDA Wall.....	75
Figure 5.30: Plan View of the MSTDA Wall Construction	75
Figure 5.31: Design Calculation of the MSTDA Wall Internal and Global Stability	76
Figure 5.32: Global Stability Analysis for the MSTDA Wall	76
Figure 5.33: Results from the MSTDA Internal and External Stability Checks	77
Figure 5.34: Standard Gabion/Reinforcement Details from Hilfiker	77
Figure 5.35: Standard Gabion/Reinforcement Details from Hilfiker	78
Figure 5.36: Italian Bar Road Site 3 Prior to Construction with Severe Shoulder Erosion.....	79
Figure 5.37: Excavation of the Existing Slope	79
Figure 5.38: Placement of First Lift of TDA	80
Figure 5.39: Facing Detail of the Metallic Hilfiker Mesh Layers, with Nonwoven Geotextile Atop Metallic Reinforcement	80
Figure 5.40: Placement of Third Lift of TDA.....	81
Figure 5.41: Placement of Granular Bearing Layer	81
Figure 5.42: Photo of the Completed Wall and Roadway from the West	82
Figure 5.43: Photo of the Completed Wall and Roadway from the East.....	82
Figure 5.44: Location of Italian Bar Road Site 6 in Tuolumne County, CA	83
Figure 5.45: Elevation View of the MSTDA Wall at Italian Bar Road Site 6	83
Figure 5.46: Plan View Schematic of the MSTDA Wall.....	84
Figure 5.47: Internal Stability Calculations of the MSTDA Wall at Italian Bar Road Site 6	84
Figure 5.48: Global Stability Calculations for the Wall at Italian Bar Road Site 6.....	84
Figure 5.49: Italian Bar Road Site 6 Before Construction.....	85
Figure 5.50: Initial Excavation and Placement of the First Welded Wire Mesh Reinforcement/Facing Unit.....	85
Figure 5.50: Placement of the First Lift of TDA	86
Figure 5.51: Encapsulation of TDA in Nonwoven Geotextile	86
Figure 5.52: Placement of Gravel Near The Facing.....	87
Figure 5.53: Italian Bar Road Site 6 Before Construction.....	87
Figure 5.54: Placement of a TDA lift	88
Figure 5.55: Placement of a TDA lift	88
Figure 5.56: Final MSTDA Wall at Italian Bar Road Site 6 from North	89
Figure 5.57: Final MSTDA Wall at Italian Bar Road Site 6 from South	89
Figure 5.58: Final Unpaved Road atop the MSTDA Wall at Italian Bar Road Site 6 From South Showing Position of the Guard Rail in the Gravel Within the Top Gabion	90

Chapter 1: Introduction

There is an urgent need for sustainable reuse options for waste tires due to the large number of tires being generated by society and the lack of environmentally friendly disposal options. USTMA (2020) reported that 263 million passenger tire equivalents were generated in 2019, while CalRecycle (2020) reported that 51.8 million were generated in California in 2019. The number of waste tires generated each year in the US has increased steadily by approximately 18% over the past decade (USTMA 2020). Historically, these waste tires would be sent to stockpiles as they are not accepted by most landfills. However, stockpiles are not a sustainable disposal approach due to risks associated with tire fires and creating a breeding ground for disease spreading insects and rodents. Tires are combustible and can be used as fuel source when mixed with coal. Approximately 14% of the tires discarded in California in 2019 were burned at permitted facilities in the state as an alternate fuel source and an additional 22% was exported out of state to be used as fuel (CalRecycle 2020). However, this is not an environmentally friendly fuel source as burning tires release toxic air pollutants including acetaldehyde, benzene, dioxins, formaldehyde, furans, hexavalent chromium, several heavy metals, and PAHs (Cheng et al. 2021). Because of the concerns with stockpiling and burning waste tires, California has the goal of recycling and reusing 75% of waste tires (CalRecycle 2017).

An effective and environmentally friendly approach for reducing tire stockpiles and reusing waste tires has been the incorporation of waste tires as an alternative backfill material in civil engineering applications (Geisler et al. 1989; Ahmed and Lovell 1993; Bosscher et al. 1993; Bosscher et al. 1997; Hoppe 1998; Dickson et al. 2001; Tandon et al. 2007; Finney and Maeda 2016; Mahgoub and El Naggar 2019) and retaining walls (Humphrey et al. 1992, 1993, 1998; Humphrey 2008; Tweedie et al. 1998a, 1998b; Xiao et al. 2012). Specific civil engineering applications include use as a lightweight embankment fill, in landslide repair/slope stabilization, as insulation layers for landfill clay liners, as alternative drainage layers in landfills, as a retaining wall backfill, as stress reduction backfill over pipes, as storm water infiltration gallery media, and as vibration mitigation layers for foundations and railroads. Through the reuse of waste tires in civil engineering applications, the quantity of stockpiled waste tires has reduced from approximately 800 million in the mid-1990's to 200 million today (Cheng et al. 2021). Approximately 5.1% of waste tires were reused in civil engineering applications in the US (USTMA 2020), while 3.0% were reused in civil engineering applications in California (CalRecycle 2020). Comparison with data from CalRecycle (2019), the amount of waste tires reused in civil engineering applications in California increased by 2% from 2018 to 2019, which indicates that this reuse option is growing in popularity.

Waste tires have been used in civil engineering applications in the form of shreds, bales, and strips. An advantage of reusing waste tires in civil engineering applications is that both older tires from stockpiles and freshly recycled tires are suitable. In many civil engineering applications tire shreds are mixed with soils, but the cost associated with mixing and the reduction in the volume of tires reused affects the economic practicality of this approach. Accordingly, the most common form of waste tires reused in civil engineering applications is as a monolithic layer of shredded tires. In this case the shredded tires are referred to as tire-derived aggregate (TDA) to emphasize that they are similar to a granular aggregate. Due to the growing popularity of reusing waste tires in the form of TDA, ASTM D6270-20 was initially developed in 1998 to provide guidance on the

classification of TDA and how it should be used in different civil engineering applications. This standard has been updated on a regular basis with new information on TDA performance.

The use of TDA as backfill in civil engineering applications not only helps reduce stockpiles and reuse waste tires, TDA also has favorable engineering properties. For example, the total unit weight of TDA is 5 to 9 kN/m³ (32 to 57 pcf), which is about one-third to one-half that of most granular backfill soils. Despite this low total unit weight that is less than that of water (9.8 kN/m³ or 62.4 pcf), the tire shreds are heavier than water (specific gravity of approximately 1.15) and will not float when submerged. The low total unit weight of TDA makes it favorable for use as a fill above deformable subgrade soil or on soils with global stability issues. In addition to the lower unit weight, TDA has shear strengths that are comparable to soils (Ghaaowd et al. 2017), a hydraulic conductivity of 0.01 m/s (on the same order of magnitude to gravel), a thermal conductivity of approximately 0.17 W/mK, which is approximately 8 times smaller than most soils, and a high damping ratio that provide TDA with favorable vibration properties (McCartney et al. 2017). Differences between TDA and granular backfills are that TDA may deform more than soils upon external loading, and that the displacement at peak shear strength is greater than in dense backfill soils. These differences in deformation response require careful consideration in the construction of civil engineering infrastructure to accommodate the more flexible response of TDA to external loading but can be overcome with careful planning and design.

The creation of TDA from waste tires requires specialized cutting equipment to minimize the amount of exposed steel in the tire particles. Exposed steel may corrode (or oxidize) which may result in exothermic reactions (Finney 2018). The sources of steel in tires are derived from the bead wire used to reinforce the tire/rim connection and cord wire embedded in the driving surface of the tire, both of which imply that iron will be present in all type of TDA. Humphrey (1996) studied the occurrence of exothermic reactions in TDA used as backfill for two road embankments in Washington and in a gravity-type retaining wall in Colorado. The fills evaluated had heights up to 60 m, free access to both air and water, and did not have careful quality control on the amount of exposed steel. While Humphrey (1996) noted that self-heating may occur due to oxidation of both the exposed steel and wires as well as microbial activity, Finney (2018) summarized several following studies that concluded that oxidation of the steel was the primary source of exothermic reactions. The rate of the exothermic reactions due to steel oxidation increases with the presence of water as well as the cation or salt concentration in the water. To address the risks of exothermic reactions, ASTM D6270-20 provides guidance on the different categories of TDA suitable for use in civil engineering applications, as well as limitations on TDA fill heights and encapsulation requirements to minimize risks of exothermic reactions. Two categories of TDA are permitted in ASTM D6270, and are defined based on their particle size distributions: Type A TDA, with particle sizes ranging from 75 to 100 mm, and Type B TDA, with particle sizes ranging from 150 to 300 mm (ASTM D6270). Both types of TDA have limits on the amount of sidewall tire pieces and the quantity of particles having different lengths of exposed steel wire. However, Type B TDA requires less processing than Type A TDA and is therefore more cost effective for earth fill applications. Type B TDA also has less exposed steel due to the larger particle sizes. ASTM D6270-20 limits the height of fills constructed using Type B TDA to 3 m (approximately 10 ft), while it limits the height of fills constructed using Type A TDA to 1 m (3 ft). Further, ASTM D6270-20 requires that monolithic layers of TDA be encapsulated with inorganic mineral soil to help dissipate heat and isolate the TDA from exposure to water.

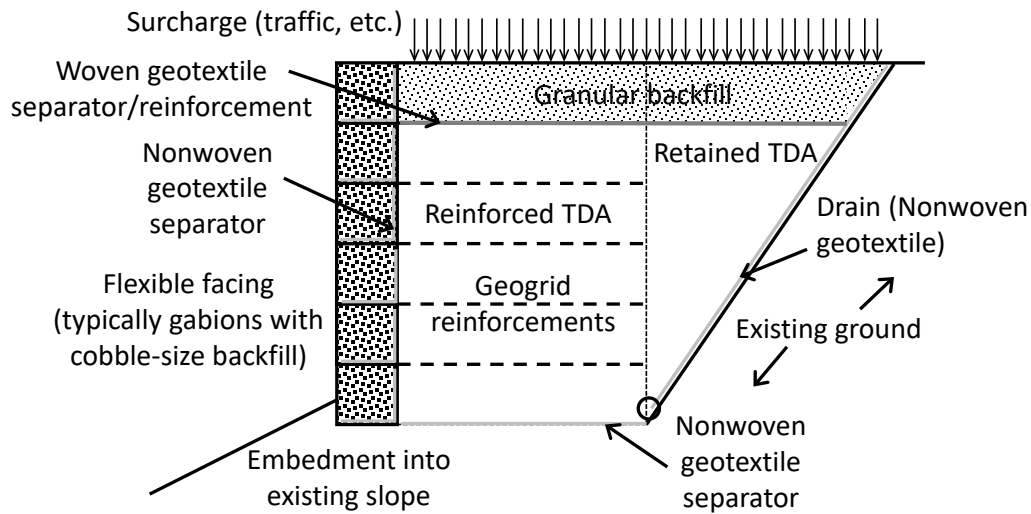
Cheng et al. (2021) reviewed several studies that assessed the environmental impacts of using TDA in civil engineering applications and concluded that it has minimal effects on the environment. They summarized the results from Toxicity Characterization Leaching Procedure (TCLP) experiments on TDA in different types of fluids. The TCLP metals analyzed by the TCLP include arsenic, barium, cadmium, chromium, copper, lead, mercury, selenium, and silver, and key volatile organic compounds and semi-volatile organic compounds that are of concern in groundwater pollution. Cheng et al. (2021) noted that for neutral pH groundwater negligible concentrations of these metals and contaminants were recorded in the leachate. Higher aqueous concentrations of metals formed when leaching in acidic conditions while higher aqueous concentrations of organics formed when leaching in basic conditions. Even then, the metal and organic component concentrations were well below the TCLP standards set by the USEPA. While all laboratory testing performed to date indicates that TDA leachate does not exhibit toxic characteristics, most of the civil engineering applications where TDA is used are above the groundwater table and regular exposure to water is limited.

TDA has been widely used as a backfill in traditional gravity-type, reinforced concrete retaining walls (Tweedie et al. 1998a, 1998b; Humphrey et al. 1998). These include a gravity-type retaining wall constructed on California Route 91 by Humphrey et al. (2008). These walls generally had good performance in terms of lateral earth pressures exerted on the retaining wall. However, recent civil engineering applications in California that will be presented in Chapter 5 have explored the approach of creating internally reinforced TDA walls that are similar to Mechanically Stabilized Earth (MSE) walls, referred to herein as Mechanically Stabilized TDA (MSTDA) walls. Internally reinforced retaining walls have lower material costs and faster construction times as they do not incorporate significant amounts of reinforced concrete. Like MSE walls, MSTDA walls are fill-type retaining walls that are used when there is a change in grade, a lane widening, or for repair of slope instability issues. MSTDA walls have a unique feature over gravity-type reinforced concrete retaining walls in that the weight of the TDA backfill will not induce as large of a stress on the underlying subgrade material. This can be advantageous in areas with subgrade soils having high compressibility or when there is global instability influenced by the weight of the retaining wall.

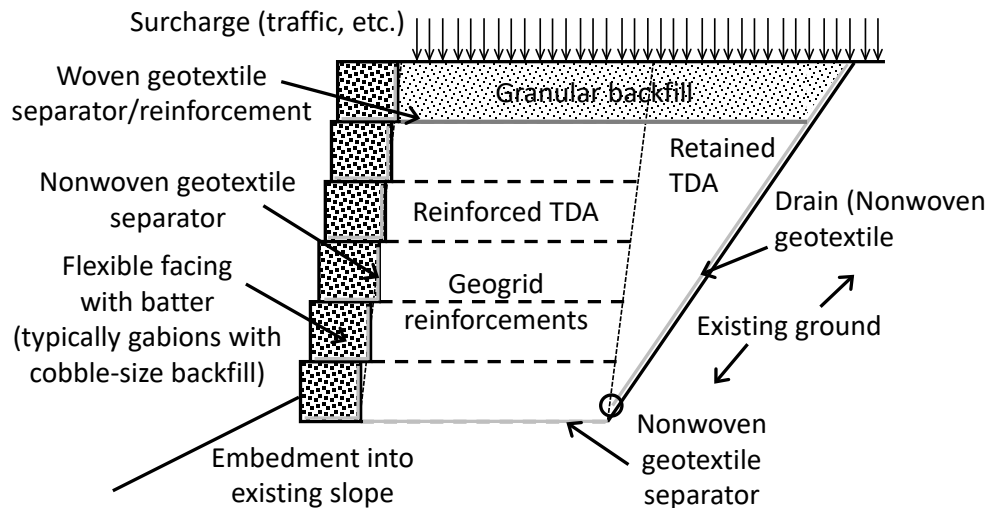
This report focuses on internally reinforced retaining wall applications built with MSTDA and focuses on material property selection and design principles. The design principles will follow the load-resistance factor design (LRFD) approach used in the FHWA design manual for MSE walls (Berg et al. 2009) and the AASHTO Bridge Manual (AASHTO 2020). While the limit state design concepts for internal and external stability of the MSTDA walls are very similar to those for MSE walls, the service limit state design concepts will consider the greater settlements encountered during compression of TDA compared to those encountered in granular backfill.

Like MSE walls, MSTDA walls have a wide range of possible geometric configurations, facing types, reinforcement types, and heights. However, for simplicity and to reflect current practice in California, this report focuses on MSTDA walls with a horizontal back-slope used to support a roadway, flexible gabion-style facing elements, extensible geosynthetic reinforcements, and granular backfill within the gabions and overlying the reinforced TDA, as shown in Figures 1.1(a) and 1.1(b). Although the wall height is typically a major design choice in MSE walls, this report focuses on MSTDA walls that have a height governed by a reinforced TDA layer having a maximum thickness of 3 m (10 ft) overlain by a granular soil layer having a thickness of 0.8 to 2.0 m

according to recommendations in ASTM D6270-20, with a total wall height of 3.8 to 5.0 m (12.5 to 16.4 ft). It is possible to construct a taller MSTDA wall by including multiple layers of TDA separated by granular backfill layers, an approach used in a TDA embankment at the Dixon Landing Interchange in Milpitas, CA (Humphrey 2008). However, this report focuses on MSTDA walls with a single reinforced TDA layer like those recently constructed in California that are described in Chapter 5 of this report.



(a)



(b)

Figure 1.1: MSTDA configurations considered in this report: (a) Vertical facing; (b) Battered facing

The granular layers shown in Figure 1.1 play several roles in the MSTDA wall, including separating the TDA from the environment, animals, and humans, providing a heat sink for any heat generated within the TDA layer, providing drainage, and providing a bearing layer for

overlying pavements. The thickness of this granular layer was defined in ASTM D6270-20 to be great enough that typical compaction specifications for granular fill (e.g., 95% of the standard Proctor dry unit weight) could be reached during construction. Humphrey and Nickels (1997) found that a minimum granular layer thickness of 0.5 was necessary so that tensile stresses are not generated at the bottom of the granular soil layer during typical vehicle loading, but that greater thicknesses may be needed for heavy vehicle loading. A leveling pad is not needed for MSTDA walls with gabion-type facing units, but the toe of the wall may be embedded. Berg et al. (2009) noted that walls in areas with scour potential should be embedded by at least 0.6 m (2 ft). Although some of the MSTDA walls in California were constructed with inextensible metallic reinforcements, geosynthetic reinforcements are recommended due concerns about corrosion of metallic reinforcements and associated effects on TDA self-heating. Berg et al. (2009) provides guidelines for mechanically stabilized walls with inextensible reinforcement types, inclined back-slopes, and other facing types (e.g., precast concrete panels or segmental blocks).

This page is intentionally left blank

Chapter 2: Review of Engineering Properties of TDA and Interaction with other Materials

General Characteristics of Type B TDA in MSTDA Walls

Type B TDA is recommended for use in MSTDA walls because its larger maximum particle size requires less processing and therefore has lower costs associated with reusing a given number of tires and a lower exposure of steel wires. ASTM D6270 describes the limits on the particle size distribution of Type B TDA, which are shown in Figure 2.1. An example of an actual Type B TDA obtained from a California processing plant and characterized by Ghaaowd et al. (2020) is shown in this figure as well. ASTM D6270-20 notes that the maximum dimension in any direction of a tire shred in Type B TDA is 450 mm (18 inches), and that only 16% by weight can be greater in dimension in any direction than 300 mm (12 inches). There is also a restriction on the smallest particle size, with only 1% smaller than 4.75 mm (0.187 inches). The reasons behind the particle size range are to encourage the use of larger tire shreds in TDA as they are less susceptible to self-heating due to the fewer exposed steel wires, but to still provide a well graded particle size distribution to promote interlocking and easy of spreading the TDA into flat compaction lifts.

ASTM D6270-20 also states that the tire shreds should not include pieces that have a tread connected to sidewall pieces on either side (i.e., pieces having a horseshoe shape). These horseshoe-shaped pieces will not lie flat during compaction, so ASTM D6270-20 states that shreds can only have tread pieces connected to a sidewall on one side. Finally, ASTM D6270-20 limits the length of exposed steel in the tire shred pieces to minimize risks of corrosion and self-heating but also for handling purposes, with less than 10% of the shreds having exposed steel wires with lengths of 50 mm (2 inches) and less than 25% of the shreds having exposed steel wires with lengths of 25 mm (1 inch). When determining the particle size distribution of Type B TDA to be used in a MSTDA wall, ASTM D6270-20 recommends using a similar approach to ASTM C136/C136M but with a larger sample size of Type B TDA ranging from 16 to 23 kg. Due to the relatively flat particles with large planar dimensions, the particle size distribution can also be determined by manual identification and sorting of particles by size as demonstrated by Ghaaowd et al. (2018). The requirements on the particle size distribution, particle shape, and steel wire exposed are typically achieved by a TDA manufacturer by using a shearing device instead of a tearing device and by passing larger shreds through the shearing device twice.

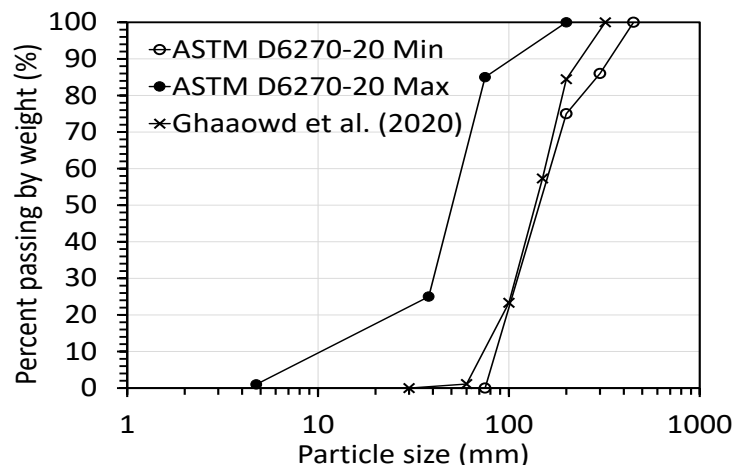


Figure 2.1: Particle size range for Type B TDA with actual Type B TDA from Ghaaowd et al. (2020)

In addition to guidance on the particle size distribution and exposed steel, ASTM D6270-20 provides guidance on the condition of the Type B TDA used in backfill applications to minimize risks of self-heating encountered in early TDA embankments. First, the TDA should be free from flammable contaminants like oil or fuel, the TDA should never have been subjected to a fire, and the TDA should be free from fibrous organic materials. There should be no direct contact between TDA and soil containing organic materials like topsoil. Finally, the TDA should be separated from surrounding soils (including the granular backfill overlying the TDA and within the gabions) using a geotextile. Finney (2018) notes that there have been no cases of exothermic reactions in TDA fills constructed according to ASTM D6270-20, and that the requirements in the standard may be overconservative. Finney performed experiments on TDA layers with a height up to 6 m and found that negligible self-heating was observed in dry TDA layers. TDA fills with heights of 3 m (10 ft) experienced an increase in temperature 13 °C when wetted with freshwater and 35 °C when wetted with saltwater, both of which are not sufficient to result in combustion. Both woven and nonwoven geotextiles have been used to provide separation in different MSTDA applications, although nonwoven geotextiles have an advantage of providing filtration and lateral drainage capabilities. It is important that any roadway constructed above the MSTDA wall have appropriate gradation to permit surface drainage away from the reinforced fill, and that a drainage layer be installed at the base of the retained and reinforced fill to carry away any groundwater. As mentioned, the TDA has high permeability, so water that does enter the MSTDA wall during extreme events can be drained as long as the granular backfill in the gabion facing elements does not contain an appreciable fines content (less than 12% fines is recommended).

Another important variable in characterizing the deformation response of TDA is the specific gravity of the particles G_s (defined as the unit weight of the particles divided by the unit weight of water). The specific gravity of crumb rubber ranges from 1.10 to 1.20 (FHWA 1998), although studies on tire shreds have reported values ranging from 1.02 to 1.27 (Bressette 1984; Humphrey et al. 1992; Humphrey and Manion 1992; Ahmed 1993). It would be expected that the specific gravity of tire shreds should be larger than that of crumb rubber due to the presence of steel wire within the shreds. Ghaaowd et al. (2017) estimated the average specific gravity of Type B TDA pieces having a variety of sizes by placing them within a porous plastic bag, then weighing the bag of TDA in air and after being submerged in water. Using this approach, they reported a specific gravity of 1.15, which is greater than the minimum specific gravity of crumb rubber.

Compaction and Compression Response of TDA

It is important to discuss the compaction and compression response of TDA prior to discussing the shear strength and stiffness parameters of TDA used in MSTDA wall design. During compaction of Type B TDA, a clear densification will occur when using appropriately sized vibratory compactors and when appropriately sized lifts are used. TDA is typically placed in lifts with a maximum thickness of 300 mm (1 ft). During compaction of TDA, voids will close, and tire shreds will rearrange and align so that their flat dimension is close to horizontal. Humphrey and Manion (1992) characterized the compaction response of Type A TDA with a maximum particle size of 75 mm (3 inches) using impact compaction and were able to reach initial dry unit weights after compaction of 6 to 6.8 kN/m³ (38 to 43 pcf). They also found that the water content of the TDA has negligible effect on the unit weight achieved through compaction, and that when using impact compaction varying the compaction effort (number of blows or weight of the hammer) does not necessarily lead to a significant increase in unit weight. Despite the lack of trend in unit

weight with compaction effort observed by Humphrey and Manion (1992), anecdotal evidence from contractors indicates that heavier compactors, use of vibration, and the lateral restraint conditions (compacting into an excavation vs. compacting next to a flexible facing) may lead to greater initial unit weights of TDA in the field.

Humphrey (1998) noted that TDA in the field may contain some water due to environmental interactions, and recommends that if the amount of water is not measured, that a gravimetric water content of $w=4\%$ be assumed. The total unit weight γ_t is related to the gravimetric water content and dry unit weight γ_d as follows:

$$\gamma_t = \frac{\gamma_d}{1 + w} \quad (2.1)$$

Similar to soils, deformation of TDA is expected to follow the effective stress principle. Skempton (1961) derived the following relationship for the effective stress in porous materials:

$$\Delta p' = \Delta p - \left(1 - \frac{C_s}{C}\right) \Delta u_w \quad (2.2)$$

where $\Delta p'$ is the increment in mean effective stress, Δp is the increment in mean total stress, Δu_w is the increment in pore water pressure, C_s is the compressibility of solid particles, and C is the compressibility of the “skeleton” of the porous material. Like soils, the compressibility of the TDA “skeleton” can be assumed to be much greater than the compressibility of the individual tire shred particles due to the void space in the TDA. In this case, the ratio C_s/C is close to zero, and Equation 2.2 reduces to Terzaghi’s effective stress definition:

$$\Delta p' = \Delta p - \Delta u_w \quad (2.3)$$

MSTDA walls should be designed with appropriate drainage so the TDA will not be in submerged conditions. Accordingly, pore water pressure effects do not need to be considered in the calculation of effective stress in the design of MSTDA walls. For dry TDA, the effective stress is the same as the total stress. As there is no evidence that the water in unsaturated TDA will contribute to capillary effects, the effective stress in unsaturated TDA can be assumed to be the same as that of dry TDA. Accordingly, when vertical stress or normal stress is used in this report, it is assumed that the effective stress is equal to the total stress and there are no pore water pressure effects regardless of the presence of water as noted by Humphrey (2008). However, it the total unit weight of TDA will be affected by the gravimetric water content, which will affect the calculated vertical stress in a TDA layer without an overlying surcharge as follows:

$$\sigma_v = \gamma_t z = \frac{\gamma_d}{1+w} z \quad (2.4)$$

where z is the depth from the TDA surface. For dry TDA, the total and dry unit weights are equal.

The application of external stresses to compacted TDA will result in a further densification, including from the self-weight stresses associated with overlying lifts of TDA and granular backfill. For example, the dry Type B TDA characterized by Ghaaowd et al. (2017) in large-scale direct shear tests was compacted to a total unit weight of approximately 5 kN/m^3 (31.8 pcf) using a small-scale vibratory compactor but experienced an increase in total unit weight of up to 8 kN/m^3 (51 pcf) during application of vertical stresses up to 76.7 kPa (1602 psf), as shown in Figure 2.2. The lower initial total unit weight after compaction obtained by Ghaaowd et al. (2017) compared to Humphrey and Manion (1992) could be due to the use of the small-scale vibratory compactor but also the larger particle size of the Type B TDA.

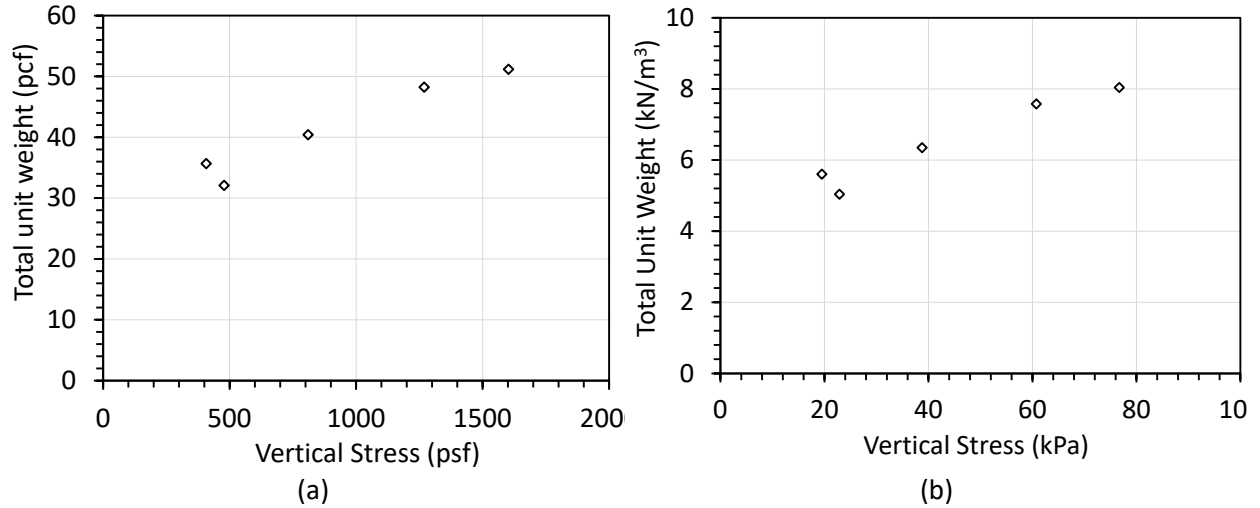


Figure 2.2: Total Unit Weight of TDA After Applied Vertical Normal Stress: (a) Imperial; (b) Metric

The trends in unit weight with normal stress can be used to define the compression curve for Type B TDA, as shown in Figure 2.3 in both imperial and metric units. The void ratio, e was calculated using from the total unit weights of the TDA in Figure 2.2 assuming $\gamma_d = \gamma_t$ as follows:

$$e = \frac{G_s \gamma_w}{\gamma_d} - 1 \quad (2.5)$$

where the specific gravity G_s is 1.15 and γ_w is the unit weight of water. The compression curve for Type B TDA obtained from the data in Figure 2.2 is shown in Figure 2.3. The compression curve includes the average initial unit weight of Type B TDA after compaction of 5 kN/m³ (31.8 pcf), which corresponds to an initial void ratio of 1.26. For comparison, the compression curve for a specimen of Type A TDA with a similar initial unit weight of 5.1 kN/m³ (32.1 pcf) (specimen NY2) reported by Humphrey (2008) is also shown in this figure. The compression curves of both types of TDA are highly nonlinear. For the purposes of design, a bilinear envelope can be used for TDA as shown in Figure 2.3, with a recompression index of C_r of 0.1 for both TDA Type A and Type B, and a compression index of $C_c = 0.45$ for Type A TDA and $C_c = 1.26$ for Type B TDA. The intersection of the recompression and compression curves is an apparent yield stress, which is 2 kPa (42 psf) for Type A TDA and 20 kPa (418 psf) for Type B TDA. The apparent yield stress may change if the initial void ratio of the TDA after compaction is different than the values shown in Figure 2.3. The results of Humphrey (2008) shown in Figure 2.4 indicate that the compression index C_c for Type A TDA decreases slightly with increasing initial dry unit weight, while the recompression index C_r is not sensitive to the initial dry unit weight.

It is important to note that the initial void ratios from laboratory testing shown in Figure 2.3 correspond to dry unit weights of approximately 5.0 kN/m³ (32 pcf) that are smaller than those encountered after compaction in MSTDA walls of 7.0 to 7.5 kN/m³ (45 to 48 pcf). An approach will be shown in Chapter 3 that uses the same values of C_r and C_c for Type B TDA in Figure 2.3, but a larger apparent yield stress to account for the lower initial void ratio associated with greater compaction. Regardless, the calculation of the change in void ratio due to application of overlying layer in an MSTDA wall will follow the same approach. For the MSTDA wall geometry in Figure 1.1, each lift will always have an initial vertical stress (defined at the center of a lift) that is smaller

than the yield stress in Figure 2.3. However, the final stress due to application of overlying layers may be less than or greater than the yield stress. In these cases, the change in void ratio for each layer can be calculated as follows:

$$\Delta e = \begin{cases} -C_r \log \left(\frac{\sigma_v'_{final}}{\sigma_v'_{initial}} \right), & \sigma_v'_{final} < \sigma_v'_{yield} \\ -C_r \log \left(\frac{\sigma_v'_{yield}}{\sigma_v'_{initial}} \right) - C_c \log \left(\frac{\sigma_v'_{final}}{\sigma_v'_{yield}} \right), & \sigma_v'_{final} > \sigma_v'_{yield} \end{cases} \quad (2.6)$$

where $\sigma_v'_{initial}$ is the initial vertical effective stress (calculated at the center of a TDA lift), $\sigma_v'_{yield}$ is the yield stress, and $\sigma_v'_{final}$ is the final vertical effective stress due to the weight of overlying layers or a surcharge (equal to the initial vertical stress plus the change in stress). The negative sign in Equation 2.6 implies that a decrease in void ratio will occur during an increase in vertical effective stress. During unloading, the TDA will rebound on a curve with a log-linear slope of C_r . It should be noted that the compression index C_c for Type B TDA is larger than that of most soils. For example, using the correlation developed by Terzaghi and Peck (1948) ($C_c = 0.009(LL-10)$) for a clay with a liquid limit of $LL = 50$, the value of C_c is 0.36.

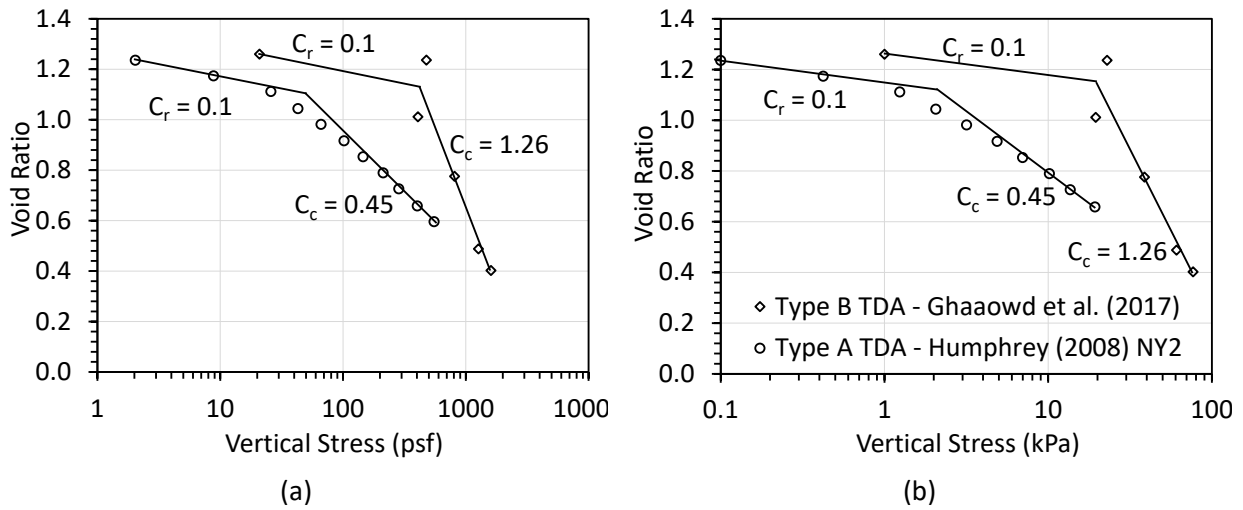


Figure 2.3: Compression Curves for Type B TDA: (a) Imperial; (b) Metric

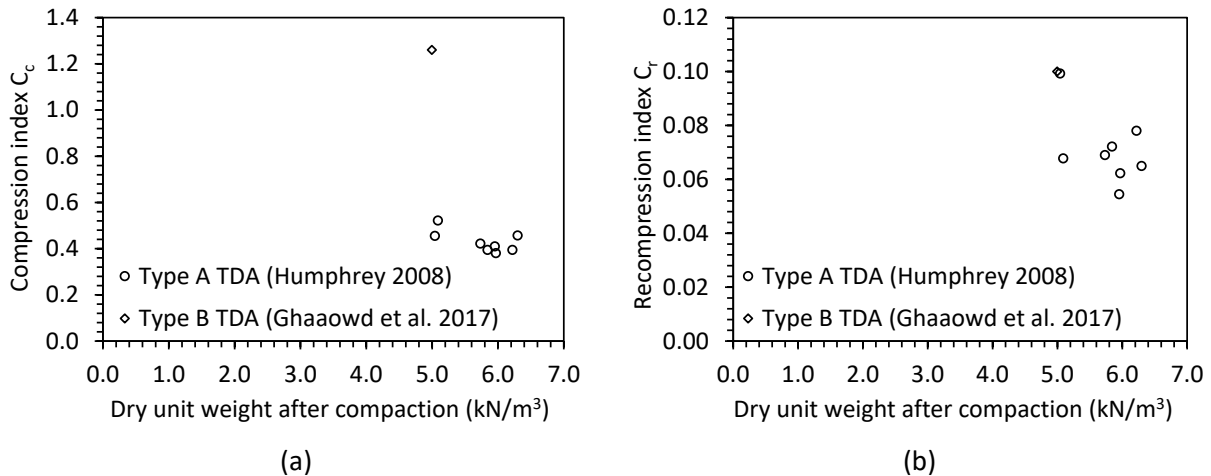


Figure 2.4: Compression Indices with initial Unit Weight: (a) Compression Index; (b) Recompression Index

The compression curves in Figure 2.3 will be used in Chapter 3 to calculate the required initial thickness of each lift in a MSTDA wall so that the final lift thickness after placement of overlying layers will be at the target elevation. The change in thickness of a layer due to the placement of overlying layers or a surcharge ΔH_s can be calculated as:

$$\Delta H_s = \frac{-H_0}{1 + e_0} \Delta e \quad (2.7)$$

where H_0 is the initial TDA fill height, e_0 is the initial void ratio (after compaction), and the negative sign indicates that a decrease in thickness is defined as positive. The compression curves in Figure 2.3 capture the range of vertical stresses encountered in MSTDA walls. For MSTDA wall heights of 3.8 to 5.0 m (12.5 to 16.4 ft), and assuming an upper bound TDA unit weight of 9 kN/m^3 and a granular backfill unit weight of 17 kN/m^3 , the vertical stresses due to self-weight of the materials at the bottom of the wall can range from 40-60 kPa (835 to 1250 psf). The addition of extra TDA to each lift so that the final elevations are at the desired locations is referred to as “overbuild” and is critical in MSTDA walls as the geosynthetic reinforcements should be horizontal after wall construction, as shown in Figure 1.1. An example of an overbuild chart developed by Humphrey (2008) based on compression data for Type A TDA is shown in Figure 2.5. For a 3 m (10 ft) MSTDA wall overlain by a granular fill with a total unit weight of 15.75 kN/m^3 and a thickness of 2 m (6 ft) and a traffic section with a surcharge of 8 kPa, the intersection of the uppermost line in Figure 2.5 with a vertical stress of 39.5 kPa (824 psf) gives a overbuild slightly greater than 0.8 ft or 0.24 m. This is one of the scenarios investigated in Chapter 3.

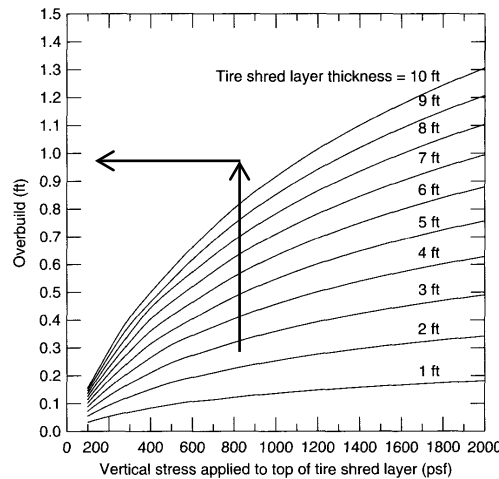
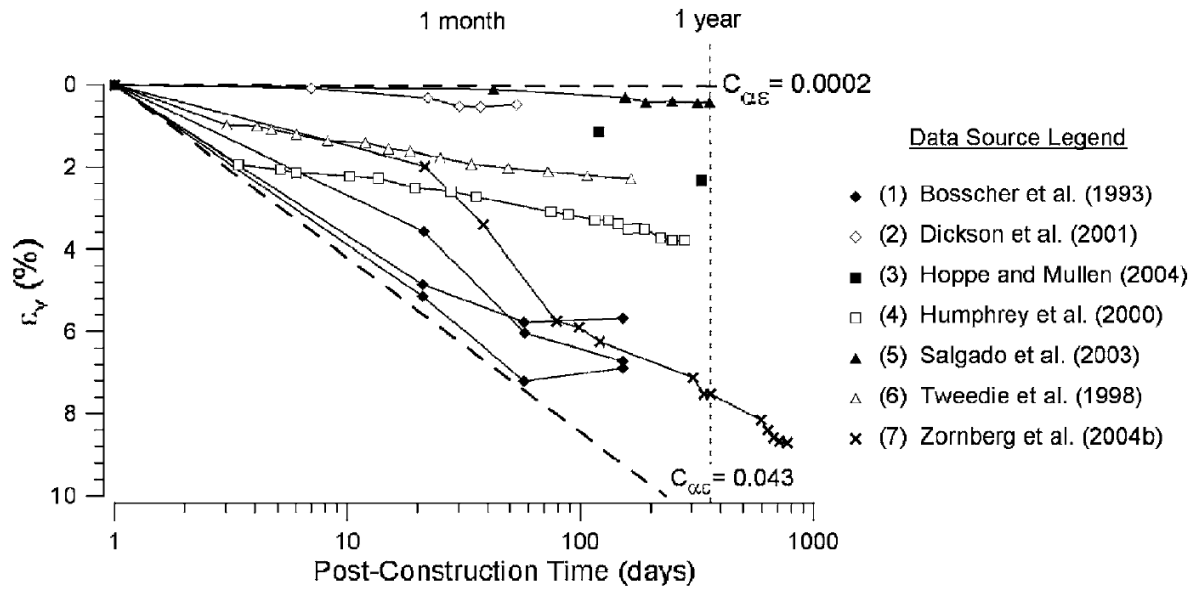


Figure 2.5: Overbuild Chart for TDA (Humphrey 2008, ASTM D6270-20)

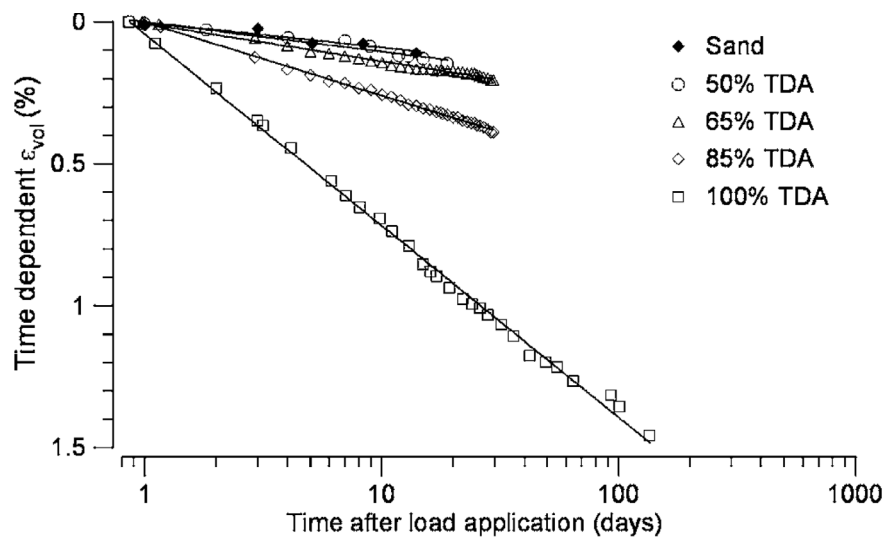
One further challenge with the compression of TDA is the likelihood of creep deformations after construction is complete. This may require a modification to the overbuild calculation shown in Figure 2.6. A summary of the vertical strains due to creep presented by Wartman et al. (2007) is shown in Figure 2.5. Although the results in Figure 2.6 are not for Type B TDA, similar behavior is expected, and the results indicate greater creep strains for TDA compared to soils. The change in thickness of a TDA layer due to creep ΔH_c can be calculated as follows:

$$\Delta H_c = H_0 C_{\alpha \varepsilon} \log(t_1/t_2) \quad (2.8)$$

where t_1 is the start of creep (assume 1 day), t_2 is the time after a certain number of days, and $C_{\alpha\varepsilon}$ is the modified secondary compression index. ASTM D6270-20 recommends using a modified secondary compression index of 0.0065 for TDA fills. Geosyntec (2008) assumed that the total change in thickness of a TDA layer is equal to the sum of ΔH_s and ΔH_c .



(a)



(b)

Figure 2.6: Creep Compression Response of TDA with Small Particle Sizes (Wartman et al. 2007): (a) Range of Vertical Strains Due to Post Construction Creep Observed in the Literature; (b) Comparison of Creep Response of TDA with that of Sand and TDA-Sand Mixtures

Internal and Interface Shear Strength of Type B TDA

The understanding of the shearing behavior of TDA, specifically that of Type B TDA with large particle sizes, is a topic that has evolved over time. While some studies used triaxial compression tests to study the shear shearing behavior of crumb rubber and TDA with small particle sizes (Bressette 1984; Ahmed 1993; Benda 1995; Masad et al. 1996; Wu et al. 1997; Lee et al. 1999; Yang et al. 2002; Jeremić et al. 2004), most studies have used direct shear tests to characterize TDA with larger particle studies. Early studies like Humphrey and Sandford (1993); Humphrey et al. (1993), Foote et al. (1996) and Bernal et al. (1997) used relatively small direct shear devices with maximum areal dimensions of 300 mm and were limited in the displacement range that could be achieved (smaller than 90 mm) and the maximum particle size that could be characterized (smaller than 150 mm). Later studies like Gebhardt (1997) and Xiao et al. (2013) used larger boxes with maximum areal dimensions of 910 and 800, respectively, but were still limited in the maximum displacement range that could be achieved (230 and 180 mm, respectively) and the maximum particle size that could be characterized (432 and 75 mm, respectively). As the direct shear devices used in these studies could not always reach the peak shear strength within the maximum displacement, it was often difficult to consistently interpret the shear strength parameters of TDA. Ghaaowd et al. (2017) reviewed the shear strength parameters of TDA from the studies mentioned above (primarily Type A TDA) and found that the friction angle varied between 19 and 38 degrees. The studies reporting a low friction angle also reported apparent cohesion intercepts, reflecting that a linear relationship was fitted to a nonlinear failure envelope. In addition to not being able to consistently reach the peak shear strength of TDA occurring at large displacements, early studies did not consider the nonlinearity in the failure envelope for TDA over the range of vertical stresses encountered in MSTDA walls.

To address the uncertainty in the shear strength parameters of TDA mentioned above and to permit the characterization of the shearing response of Type B TDA to large displacements over a wide range of normal stresses, Fox et al. (2018) developed a large-scale shearing device that could either be operated in direct shear mode or simple shear mode. This device was used to characterize the internal shear strength of TDA and the shear strength of TDA-concrete interfaces by Ghaaowd et al. (2017), the cyclic shearing response by McCartney et al. (2017), the shear strength of TDA interfaces with different soils by Ghaaowd et al. (2020), and the pullout of geosynthetic reinforcements from TDA by Ghaaowd and McCartney (2020). This report uses the results from these studies to provide guidance on material properties for MSTDA wall design.

The area-corrected shear stress-displacement curves from direct shear tests on Type B TDA reported by Ghaaowd et al. (2017) in Imperial and Metric units are shown in Figures 2.7(a) and 2.7(b), respectively. The initial normal stresses shown in these figures bracket the range expected in MSTDA walls. Due to the changes in normal stress that occur during direct shear tests, the curves in Figures 2.7(a) and 2.7(b) are not ideal for defining the point of shear failure. Instead, the plots of the mobilized secant friction angle in Imperial and Metric units shown in Figures 2.7(c) and 2.7(d), respectively, are more suitable for interpreting the point of shear failure. At the peak of each of these curves the TDA has mobilized the maximum frictional resistance. Two observations can be drawn from these figures – a decrease in the peak secant friction angle with increasing initial normal stress indicating a nonlinear failure envelope, and a relatively large displacement at peak ranging from 337 to 439 mm (13.3 to 17.3 inches). These values indicate that TDA has a very ductile shearing response. Direct shear tests area always

performed in drained conditions, which is suitable for characterizing the shearing behavior of TDA as it has high permeability and any shear-induced pore water pressures will drain rapidly. However, volume changes may occur during drained shearing of TDA, which are important to characterize for the development of advanced constitutive models. The vertical strain vs. horizontal displacement curves for Type B TDA measured during the direct shear tests are shown in Imperial and Metric units in Figures 2.7(e) and 2.7(f), respectively. Type B TDA tends to dilate after displacements of 131 to 284 mm (5.2 to 11.2 inches). Ghaaowd et al. (2017) also performed direct shear tests with different displacement rates and found that the shear strength was not sensitive to the shear displacement rate.

The shear failure envelopes for the Type B TDA internal direct shear test results from Ghaaowd et al. (2017) with the points at failure obtained from the maximum mobilized secant friction angle curves in Figures 2.7(c) and 2.7(d) are summarized in Figures 2.8(a) and 2.8(b) in Imperial and Metric units, respectively. In addition, the failure envelopes for interfaces between Type B TDA and concrete measured by Ghaaowd et al. (2017) and interfaces between Type B TDA and different soils measured by Ghaaowd et al. (2020) are also included in these figures for reference. The interfaces with different soils measured by Ghaaowd et al. (2020) all had separation geotextiles consistent with recommendations in ASTM D6270-20, although it should be noted that the TDA was observed to interact with the underlying soil through the separation geotextile. The shear strength of the Type B TDA is consistently higher than the interfaces with the other materials. As there was no source of apparent cohesion in the Type B TDA or the interfaces with different materials, nonlinear failure envelopes were fitted to each of the data sets in this figure using the shear strength model of Duncan et al. (1980):

$$\tau_f = \sigma_f \tan(\phi_{sec}(\sigma_f)) \quad (2.9)$$

where τ_f is the shear strength defined at the point of maximum mobilized secant friction angle, σ_f is the vertical normal stress at failure, and $\phi_{sec}(\sigma_f)$ is the stress-dependent secant friction angle. The stress-dependent secant friction angle can be calculated using the following equation:

$$\phi_{sec}(\sigma_f) = \Delta\phi \log\left(\frac{\sigma_f}{P_{atm}}\right) + \phi_0 \quad (2.10)$$

where P_{atm} is atmospheric pressure (101.3 kPa or 2116 psf) and $\Delta\phi$ and ϕ_0 are fitting parameters that denote the change in secant friction angle with normal stress and the secant friction angle at a normal stress equal to the atmospheric pressure, respectively. For materials with a linear failure envelope, the value of $\Delta\phi$ is zero, and $\phi_{sec} = \phi_0$.

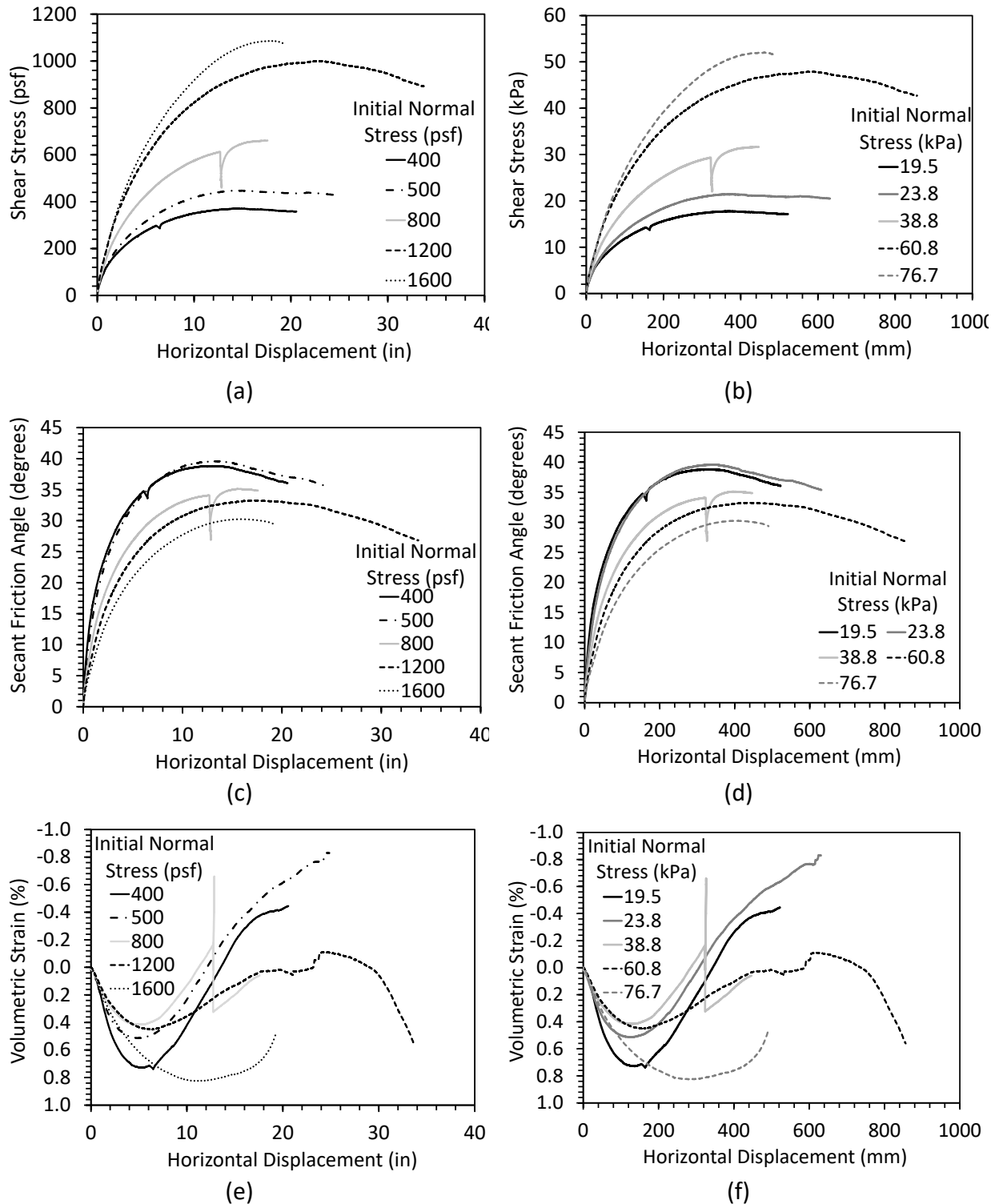


Figure 2.7: Type B TDA Direct Shear Results: (a) Stress Displacement Curves: Imperial; (b) Stress-Displacement Curves: Metric; (c) Secant Friction Angle Mobilization Curves: Imperial; (d) Secant Friction Angle Mobilization Curves: Metric; (e) Volumetric Strain vs. Displacement Curves: Imperial; (f) Volumetric Strain vs. Displacement Curves: Metric

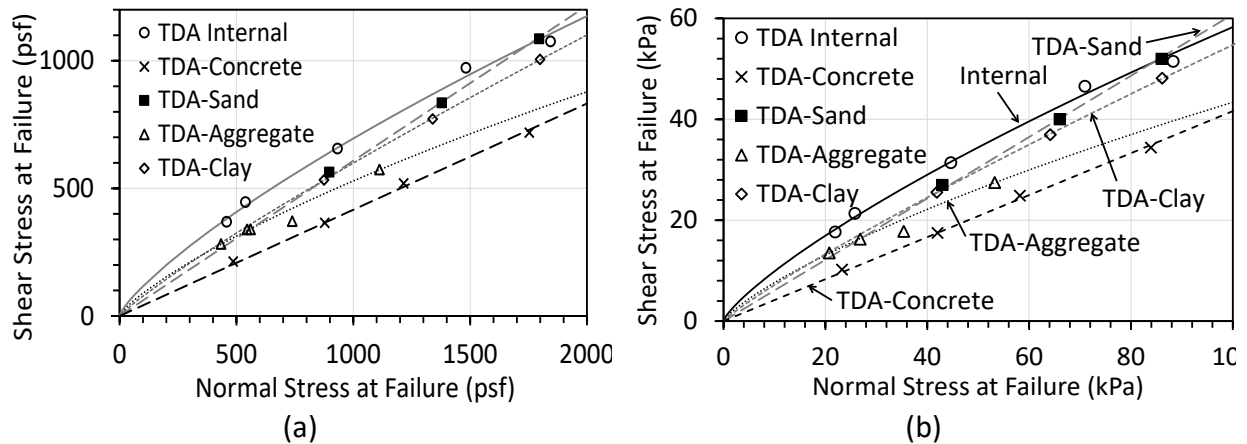


Figure 2.8: Shear Failure Envelopes for Internal Type B TDA and Interfaces Between Type B TDA with Different Materials (Ghaaowd et al. 2017, 2020)

The parameters for the different failure envelopes are shown in Table 2.1. The value of ϕ_0 is the secant friction angle at a normal stress of $P_a = 101$ kPa while the value of $\Delta\phi$ describes how the secant friction angle decreases with the logarithm of normal stress. The Type B TDA itself had a nonlinear response, with a friction angle consistent with granular materials. For the range of vertical stresses in MSTDA walls of 27 to 45 kPa, the secant friction angle calculated with the ϕ_0 and $\Delta\phi$ parameters in Equation 2.10 ranges from 35 to 39°. The interfaces between Type B TDA and clay and Type B TDA and aggregate were both nonlinear, while the interfaces between Type B TDA and concrete and Type B TDA and sand were both linear. A major difference between the failure envelopes shown in Table 2.1 and those for granular backfills used in MSE walls is the displacement at the peak failure conditions obtained from the curves in Figures 2.7(c) and 2.7(d). These displacements at peak are much greater than granular backfill soils, which typically reach a peak within the extents of a standard direct shear box for soils having a maximum displacement of 50 mm (2 inches).

Table 2.1: Shear Failure Envelope and Displacement Parameters (Ghaaowd et al. 2017, 2020)

Interface	Separation Geotextile	ϕ_0 (degrees)	$\Delta\phi$ (degrees)	Ave. Displacement at Peak (mm)	Ave. Displacement at Peak (inches)
TDA Internal	None	30.2	-14.4	385	15.2
TDA-Concrete	None	22.6	0.0	180	7.1
TDA-Aggregate	Woven	23.4	-13.9	244	9.6
TDA-Sand	Nonwoven	31.3	0.0	340	13.4
TDA-Clay	Nonwoven	28.7	-7.0	283	11.1

Note: The symbol ϕ is used for both internal and interface friction angles

The dilation angle ψ is used to quantify the dilation (volumetric expansion) that occurs during shearing, and for the case of direct shear tests can be defined as follows:

$$\psi = \sin^{-1} \left(\frac{\tan(\delta_v/\delta_h)}{2 + \tan(\delta_v/\delta_h)} \right) \quad (2.11)$$

where δ_v is the vertical displacement and δ_h is the horizontal displacement. For the results shown in Figures 2.7(e) and 2.7(f), δ_v is the product of the volumetric strain and the height of the TDA layer (approximately 1500 mm), and the slope δ_v/δ_h should be defined after the initial compression when there is a tendency toward negative volumetric strains (i.e., for the test at a vertical stress of 19.5 kPa or 400 psf, the slope should be defined between displacements of 200 and 400 mm or 8 and 16 inches). The Type B TDA also shows a small amount of dilation during shearing, as shown in Figures 2.7(e) and 2.7(f) and summarized in Figures 2.9(a) and 2.9(b).

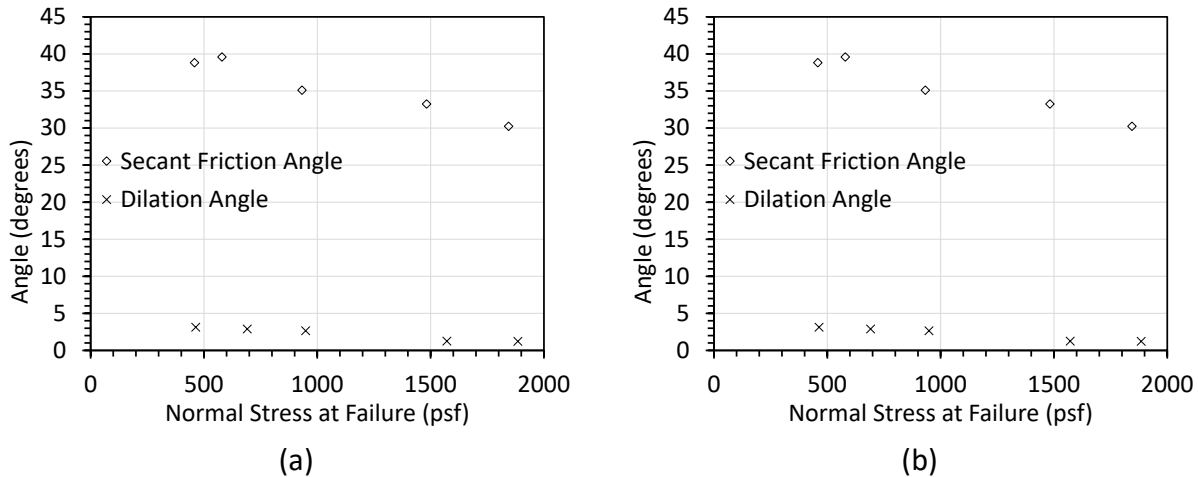


Figure 2.9: Comparisons Between the Secant Friction Angle and Dilation Angle Measured for Type B TDA Over a Range of Normal Stresses (Ghaaowd et al. 2017): (a) Imperial; (b) Metric

The dilation angle of TDA is relatively low and decreases with normal stress, with an average value of 2.2 degrees. The curves in Figures 2.7(e) and 2.7(f) indicate that the onset of dilation typically does not occur until relatively large displacements that approximately half that required to reach the peak shear strength. The MSTDA design guidelines do not consider dilation as they are based on limit equilibrium methods that assume the TDA is at the point of peak shear failure, but the dilation angle may be relevant when performing more advanced finite element analyses.

Cyclic Shearing Response of Type B TDA

The effects of earthquakes are typically considered in MSE wall design through a pseudo-static analysis, where an equivalent horizontal force is applied to a wall in a limit equilibrium analysis (Berg et al. 2009). Accordingly, an understanding of the cyclic shearing properties of TDA is not necessary in the design of MSTDA walls. Nonetheless, the dynamic properties of TDA may be useful when performing advanced seismic analyses of the wall. The large-scale shearing device developed by Fox et al. (2018) can be configured to perform cyclic simple shear tests to determine the dynamic properties of TDA. McCartney et al. (2017) presented the results from cyclic simple shear tests on Type B TDA specimens in this device under different constant vertical stresses subjected to cyclic simple shear strain amplitudes ranging from 0.1 to 10%. The main outcome from these cyclic simple shear tests is the hysteretic shear stress vs. shear strain curve, which can be used to quantify the secant shear modulus and damping ratio as a function of the vertical stress and cyclic shear strain amplitude. The shear modulus was observed to increase nonlinearly with the vertical stress, as shown in Figure 2.10(a), but decrease nonlinearly with

increasing shear strain amplitude. Figure 2.10(a) also includes power law relationships that were fitted to the secant shear modulus G vs. vertical stress σ_v data, having the following general form:

$$G = A \left(\frac{\sigma_v}{P_a} \right)^n \quad (2.12)$$

where P_a is the atmospheric pressure, and A and n are empirical fitting parameters. The damping ratios calculated from the area within the hysteretic shear stress vs. shear strain curves are shown in Figure 2.10(b). The damping ratios shown in this figure are greater than most granular soils, and a decreasing-increasing trend is observed with increasing shear strain amplitude instead of a monotonically increasing trend typically observed for soils.

The results in Figure 2.10(a) can be used to define a shear modulus reduction curve, which is a commonly used relationship in dynamic analyses. The shear modulus reduction curve model of Darandelli (2001) was fitted to the shear modulus data plotted as a function of the cyclic shear strain in Figure 2.11(a). This model has the following form:

$$\frac{G}{G_{max}} = \left[1 + \left(\frac{\gamma_a}{\gamma_0 (\sigma_v / P_a)^m} \right)^a \right]^{-1} \quad (2.13)$$

where G_{max} is the maximum secant shear modulus for a given vertical stress, γ_a is the cyclic shear strain amplitude, γ_0 is a reference shear strain, and a and m are fitting parameters. McCartney et al. (2020) estimated the relationship between G_{max} and σ_v using parameters $A = 3800$ kPa and $n = 0.51$, and used values of $a = 0.75$, $\gamma_0 = 0.6$, and $m = 0.55$ to fit Equation 2.13 to the secant shear modulus vs. cyclic shear strain amplitude data in Figure 2.11(a). Normalized G/G_{max} versions of the modulus reduction curves are shown in Figure 2.11(b). Although dynamic analyses typically require both a modulus reduction curve and a damping ratio vs. cyclic shear strain curve, the nonlinear shape of the damping ratio relationship in Figure 2.10(b) is difficult to capture with a fitting relationship. Instead, it is recommended to use an average value of damping ratio over the expected cyclic shear strain amplitude in advance dynamic analyses of MSTDA walls.

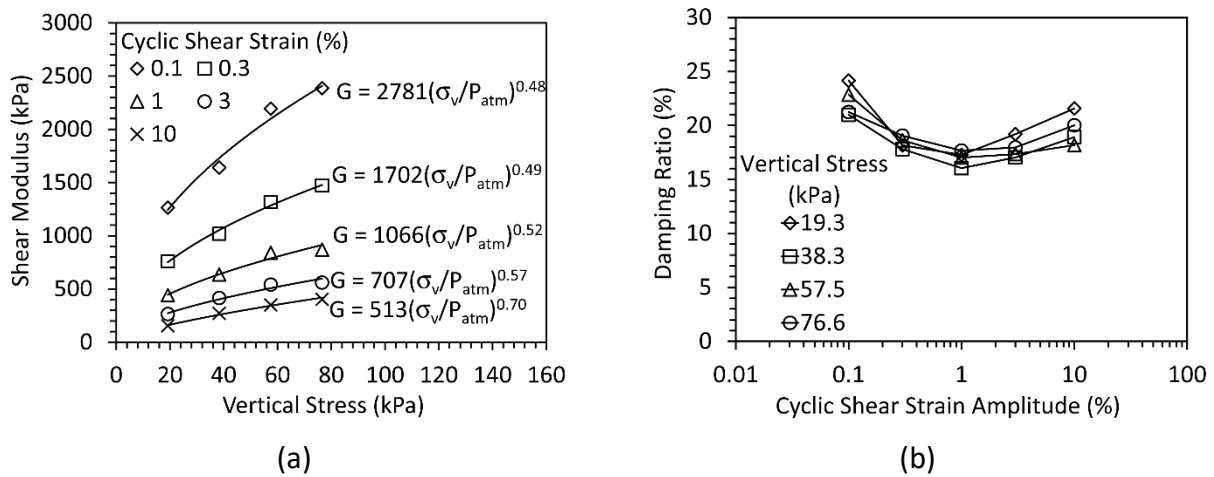


Figure 2.10: Cyclic Shearing Response of Type B TDA Under Different Vertical Stresses and Cyclic Shear Strain Amplitudes (McCartney et al. 2017): (a) Shear Modulus; (b) Damping Ratio

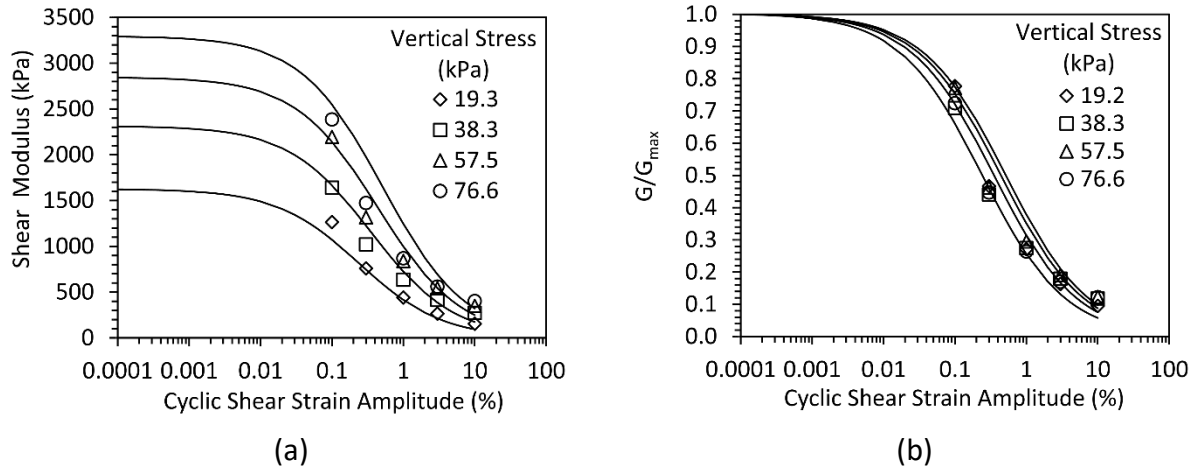


Figure 2.11: Modulus Reduction Curves for Type B TDA (McCartney et al. 2017): (a) Fitted Curves to Measured Data; (b) Normalized Modulus Reduction Curves

Pullout of Geosynthetic Reinforcements from Type B TDA

As mentioned, geosynthetic reinforcements are recommended for use in MSTDA walls as they are not prone to corrosion like metallic reinforcing grids or strips. They have also been widely used in MSE wall applications. The pullout test is typically used to characterize the interaction between a backfill material and a reinforcement. Ghaaowd and McCartney (2020) converted the large-shearing device of Fox et al. (2018) into a pullout device to characterize the pullout response of three geogrids from Type B TDA. Specifically, they characterized the pullout force-displacement curves for the geogrids defined at the face of the box as well as the mobilization of displacements along the length of the geogrids during pullout. Geogrids are considered extensible reinforcements as they stretch during the pullout process. The details of the three geogrids considered by Ghaaowd and McCartney (2020) are summarized in Table 2.2. These geogrids are typical for those used in MSTDA applications in California and represent both uniaxial geogrids and biaxial geogrids. Uniaxial geogrids are generally used as the primary reinforcement type in MSE walls due to their high tensile strength and stiffness, but biaxial geogrids are used near corners where the direction of loading may not be perpendicular to the wall face. The geogrids all had a width of 610 mm and an embedded length of 1245 mm within the TDA layer. As pullout typically occurs under lower confining stresses, the range of vertical stresses considered in the pullout tests was smaller than that considered in the direct shear tests. The pullout vs. face displacement curves for a range of vertical stresses are shown in Figures 2.12(a), 2.12(b), and 2.12(c) for the three geogrids in Type B TDA. It was possible to pull the two uniaxial geogrids out of the Type B TDA under vertical normal stresses up to 58.1 kPa, but the biaxial grid, which had lower tensile strength, ruptured during pullout under a lower vertical normal stress of 29.3 kPa. The three geogrids have different behavior as the aperture sizes and material lead to different interaction mechanisms with the TDA. Geogrid GGA is made from high density polyethylene, which has a relatively smooth surface. Geogrid GGB is made of polyester yarns with PVC coating, and interacted very well with the TDA. Geogrid GGC was made from polypropylene and had smaller openings and thicker junctions between ribs that interacted well with the TDA. A general observation from the pullout curves is that the displacement at peak was

relatively large, ranging from 100 to 350 mm. GGB experienced partial tensile rupture at the highest normal stresses of 47.9 and 58.1 kPa, while GGC ruptured at a normal stress of 29.3 kPa.

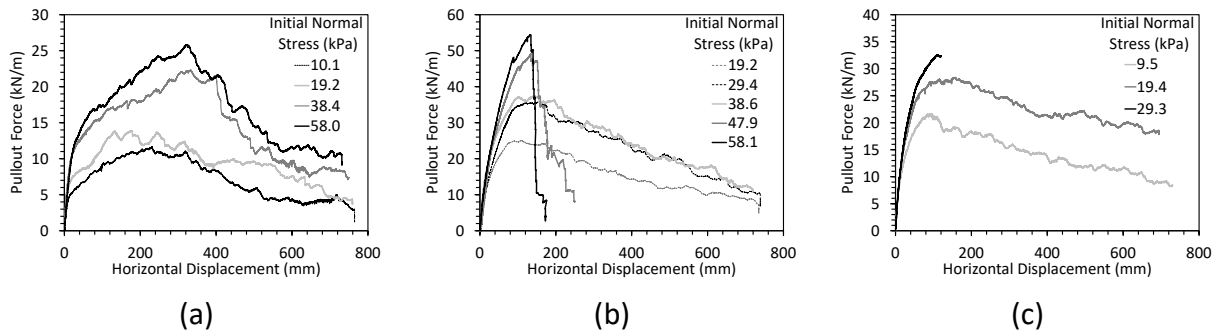


Figure 2.12: Geogrid pullout force-displacement curves for Type B TDA (Ghaaowd and McCartney 2020): (a) GGA; (b) GGB; (c) GGC

Table 2.2: Geogrid Characteristics used in the Pullout Tests of Ghaaowd and McCartney (2020)

Geogrid	Product Name (polymer)	Type	Aperture dimensions (mm)	Maximum tensile load (kN/rib)	Maximum tensile load (kN/m)
GGA	Tensar UX1100 (HDPE)	Uniaxial	424 (machine) × 17 (cross-machine)	1.2	53.3
GGB	Miragrid 5XT (PET)	Uniaxial	22 (machine) × 25 (cross-machine)	1.9	71.6
GGC	Tensar BX1500 (Polypropylene)	Biaxial	25 (machine) × 31 (cross-machine)	1.2	36.8

The maximum pullout force per unit width of the geogrid vs. vertical stress for the three geogrids is shown in Figure 2.13. Although approximately linear relationships are observed, the data in this plot cannot be directly used in a pullout analysis as the pullout force is related to the friction on either side of the geogrid and the interaction between the TDA and the apertures. Accordingly, it is more common to interpret the pullout results in terms of a pullout factor, F defined using the following relationship:

$$F = \frac{P_r}{\alpha \sigma_v C L} \quad (2.14)$$

where P_r is the maximum pullout force, α is a scale correction factor, L is the embedded length in the TDA specimen in the pullout box (equal to 1.245 m for all the tests in Figure 2.13), C is the geogrid effective unit perimeter (equal to 2.0 to consider interaction with both the top and bottom of the geogrid). The value of α is assumed to equal 0.8, which is the value assumed by Elias et al. (2001) for extensible geogrids.

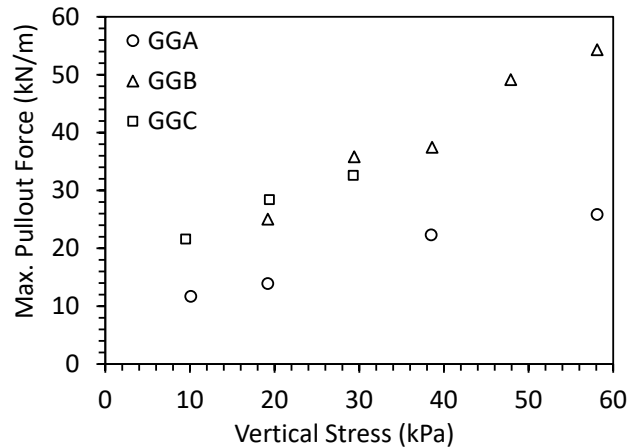


Figure 2.13: Maximum Pullout Force vs. Vertical Normal Stress for Different Geogrids in Type B TDA (Ghaaowd and McCartney 2020)

The pullout factors for the three geogrids are shown in Figure 2.14(a). A nonlinear decreasing trend is observed for all three geogrids, so a power law relationship was fitted to each data set. This relationship can be used directly in the MSTDA design calculations in Chapter 3, or an average value can be used to simplify calculations. The average values of F are 0.37 for GGA (for vertical stresses between 10.1 to 58.1 kPa only), 0.55 for GGB (for vertical stresses between 19.2 and 58.1 kPa only), and 0.81 for GGC (for vertical stresses between 9.5 and 29.3 kPa only). These results indicate that that pullout factor is not correlated with the tensile strength of the geogrid as long as the tensile strength is greater than the pullout strength. The pullout factor is more sensitive to the frictional interaction between the TDA and the geogrid and the amount of interlocking between the TDA and the geometric features (openings) of the geogrids. For example, the HDPE uniaxial geogrid GGA is smoother than the other two geogrids and has thinner openings, so the overall interaction between the geogrid and TDA was lower during pullout. The other two geogrids have square openings which may lead to more interlocking with the TDA. The decreasing trends in F with increasing vertical stress could be due to the nonlinear shearing response of the TDA as well as a change in the interlocking mechanisms with increased vertical stress due to TDA particle rearrangement. An additional consideration is the large displacement at the maximum pullout force, summarized in Figure 2.14(b). The displacements in this figure are consistent with the displacements at peak shear strength of the Type B TDA shown in Table 2.1, indicating that the MSTDA wall may experience large deformations before the geogrids are able to pull out of the Type B TDA.

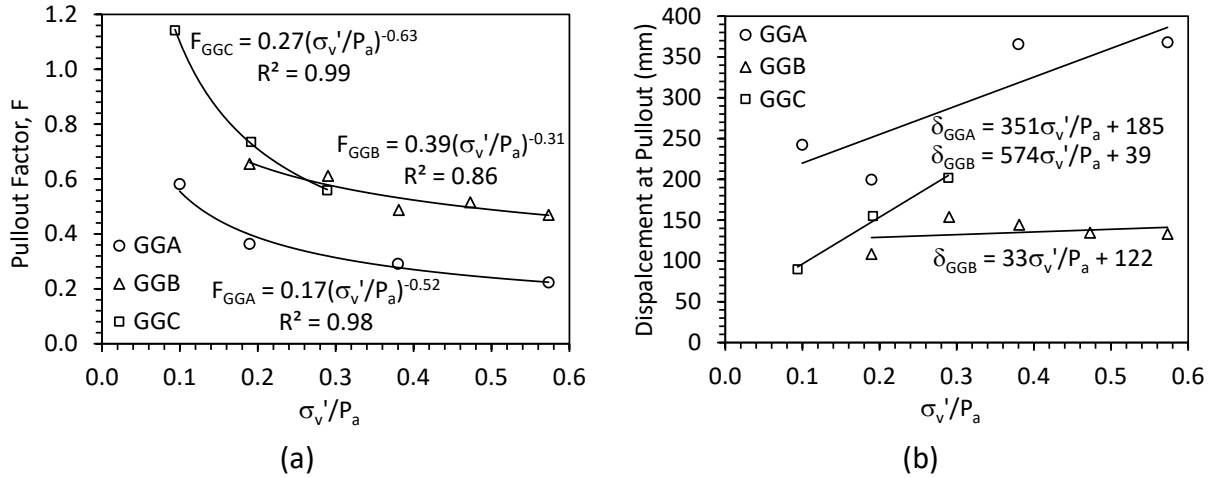


Figure 2.14: Synthesized Pullout Test Results (Ghaaowd and McCartney 2020): (a) Pullout Factor for Different Geogrids from Type B TDA as a Function of the Confining Stress; (b) Pullout Displacement at the Peak Pullout Force

Although they are not recommended in MSTDA walls due to corrosion and self-heating risks, metallic grids have been used in MSTDA walls, so it is relevant to understand their pullout response. Youwei et al. (2004) presenting the pullout response of metallic grids with hexagonal openings from tire shreds with a maximum particle size of 60 mm. They presented pullout factors for the metallic grids from ranging from 0.72 to 0.85. These pullout factors are on the high side of the range of factors measured for the geogrids in Type B TDA shown in Figure 2.13(a). It is important that the TDA has direct contact with the metallic grid to rely upon interlocking effects.

Calibration of Advanced Constitutive Models for Finite Element Modeling

While the shear strength failure envelopes presented earlier in this chapter are sufficient to perform the limit equilibrium analyses necessary for MSTDA design, additional material properties are necessary to perform advanced analyses of the deformation response and stress distribution in MSTDA walls. These advanced analyses are typically performed in practice using a finite element or finite difference software. The collection of material properties that describe the stress-strain response of a geomaterial is typically referred to as a constitutive model.

The simplest constitutive model used in limit equilibrium analyses is the perfectly plastic model, in which there are no deformations until reaching the yield or failure criteria for the geomaterial, which for TDA is given by Equation 2.9. A limit equilibrium analysis cannot provide any information on the deformations of an MSTDA wall, but instead assumes that the entire MSTDA mass is at the point of failure. The most common constitutive model used in geotechnical engineering analysis is the elastic-perfectly plastic model, which combines a linear elastic stress-strain model with a yield or failure criteria (typically the Mohr-Coulomb failure criterion). Equation 2.9 is a modified form of the Mohr-Coulomb relationship that does not include a cohesion parameter but includes a vertical stress-dependent secant friction angle. However, this constitutive model is not capable of capturing the nonlinear shear stress-displacement response exhibited by the Type B TDA in Figure 2.7.

This section summarizes the calibration of a modified form of the Duncan-Chang hyperbolic model to capture the vertical stress-dependent shear stress-displacement curves for Type B TDA. The Duncan-Chang hyperbolic model described by Duncan et al. (1980) is typically calibrated using triaxial compression test results presented in terms of deviatoric stress-axial strain curves. Direct shear tests like those presented in Figure 2.7 are always presented in terms of displacement, so it is not possible to define stress-dependent moduli that are necessary in finite element analyses. However, the results are suitable to define stress-dependent stiffness values that may be modified in some cases into modulus values for finite element analyses. In the modified form of the Duncan-Chang hyperbolic model, the shear stress-displacement curve is given as follows:

$$\tau = \frac{\delta}{\left(\frac{1}{J_i} + \frac{\delta}{\tau_f / RF}\right)} \quad (2.15)$$

where τ is the shear stress, δ is the horizontal displacement, J_i is the stress-dependent initial shear stiffness, τ_f is the shear strength defined by Equation 2.9, and RF is a reduction factor to account for nonlinearity. In the conventional Duncan-Chang model, the shear stress is the deviator stress, the horizontal displacement is the axial strain, and the initial shear stiffness is the initial elastic modulus. In Equation 2.15, the stress-dependent initial stiffness can be defined as follows:

$$J_i = k_s P_a \left(\frac{\sigma_{v, failure}}{P_a} \right)^{n_s} \quad (2.16)$$

where k_s and n_s are fitting parameters, and $\sigma_{v, failure}$ is the value of vertical normal stress at failure from a direct shear test. The initial stiffness J_i has SI units of kPa/m, which is different from the initial modulus E_i in the conventional Duncan-Chang model that has units of kPa. The vertical normal stress changes during a direct shear test, so it is important to use the experimental values of vertical stress at failure when defining the parameters of the model in Equations 2.15 and 2.16. However, in a simulation of a MSTDA wall the values of vertical normal stress at a location of interest can be used in Equation 2.16 to define the value of J_i as the vertical normal stress in the field is not expected to change during shearing. The value of RF in Equation 2.15 represents the nonlinearity of the shear stress-displacement curve. A value closer to 1.0 will be nonlinear and will follow the shape of a hyperbola, while a value closer to zero will be closer to an elastic-perfectly plastic material. A fit of Equation 2.15 to the direct shear tests on Type B TDA is shown in Figure 2.15(a), which indicate a good fit to the experimental data. The parameters for Type B TDA in the modified Duncan-Chang model are summarized in Table 2.3. The value of RF for Type B TDA is relatively high, reflecting the nonlinear response of this material. The initial stiffness values from the model are shown in Figure 2.15(b), along with values for the TDA-concrete interface which are at least twice as stiff as the TDA. The values shown in Table 2.3 should be used with caution when interpreted to perform finite element analyses that are performed in terms of shear stress vs. shear strain but may be a useful starting point in these analyses.

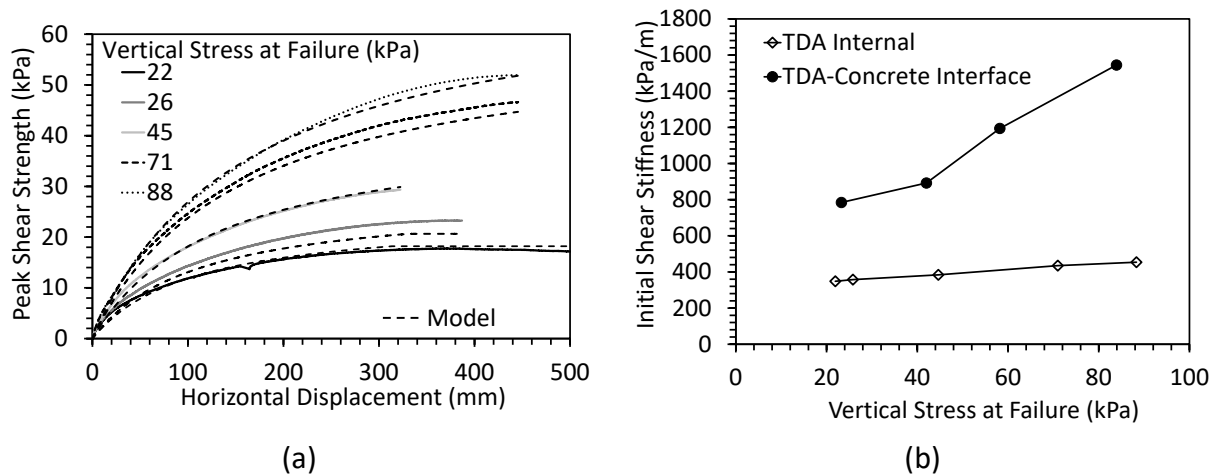


Figure 2.15: Hyperbolic Model Fitting Results: (a) Stress-Displacement Curves for Type B TDA; (b) Initial Shear Stiffness Values for Type B TDA and Type B TDA-Concrete Interfaces

Table 2.3: Type B TDA parameters for the modified Duncan-Chang hyperbolic model

Parameter	Symbol	Value	Units
Secant friction angle at $P_a = 100$ kPa	ϕ_0	30.2	Degrees
Change in secant friction angle with normal stress	$\Delta\phi$	-14.2	Degrees
Reduction factor	RF	0.75	
Reference shear stiffness	k_s	4.56	1/m
Shear stiffness exponent	n_s	0.45	

This page is intentionally left blank

Chapter 3: Design Methodology for MSTDA Retaining Walls

Overview of MSTDA Design Philosophy

The design methodology for MSTDA walls builds upon the well-established FHWA design methodology for MSE walls (Berg et al. 2009). The FHWA design methodology for MSE walls developed by Berg et al. (2009) is based on the concept of load-resistance factor design (LRFD) and is an update of an earlier design methodologies developed by Elias et al. (2001) and Christopher et al. (1996) that were based on Allowable Stress Design (ASD). LRFD accounts for uncertainty in the applied load and material resistance separately through load factors Γ_i and resistance factors Φ_i , respectively, while ASD combines all uncertainty into a factor of safety. In the LRFD framework, the behavior of the MSTDA wall should be considered under four groups of limit states: (1) strength limit states; (2) serviceability limit state; (3) extreme event limit states, and (4) fatigue limit states. As this report is developed based on the experience on MSTDA walls in California, the effects of earthquakes will be considered as an extreme event limit state, but other types of extreme events like vehicular impacts and flood events are not discussed and the reader is referred to Berg et al. (2009) for more details. The load and resistance factors depend on a given limit state being considered, but in general load factors are typically greater than 1.0 and increase the applied loads for design purposes while resistance factors less than 1.0 and reduce the material resistance for design purposes. There are some cases where the load factor is less than 1.0 to account for the possibility that vertical stresses are not as great as expected, which could reduce the confinement of geosynthetic reinforcements and affect the stability. As information on the uncertainty associated with MSTDA walls has not been well characterized, the load and resistance factors used for MSE walls are adopted for MSTDA walls in this report until more information becomes available. The specific checks for the strength limit states required for MSTDA wall design include external stability (limiting eccentricity, sliding, bearing resistance, and global/compound stability) and internal stability (tensile resistance of reinforcements, pullout resistance of reinforcements, structural resistance of facing-reinforcement connections). The specific checks for service limit states include vertical wall movements including overbuild and creep deformation estimates and lateral wall movements during compaction.

MSTDA Design Procedure Overview

The following steps should be followed when designing an MSTDA wall. These are essentially the same as those developed by Berg et al. (2009), with an additional step included to consider overbuild requirements for each TDA lift to ensure horizontal reinforcement layers. Although the global stability check in Step 9 is an external stability check, it is performed after the internal stability check as it should incorporate the final reinforcement spacing and reinforcement strength. Seismic events also have effects on both the external and internal stability, but it is performed at the end as the static design is used to provide a baseline configuration that can be refined to account for seismic effects.

Step 1: Establish project requirements:

- Define site topography and extents of the MSTDA wall.
- Define the expected static surcharge loads, pseudo-static transient loads (i.e., traffic surcharge), and pseudo-static seismic loads (i.e., equivalent horizontal earth pressure coefficient to account for expected site-specific earthquake loading).
- Define the thickness of the granular fill layer depending on the expected traffic loading.
- Define any additional performance criteria or construction constraints beyond those set in ASTM D6270-20.

Step 2: Establish project material parameters:

- Perform a site investigation to characterize subsurface layers and define their representative mechanical properties for design (total unit weight, gravimetric water content, friction angle, and apparent cohesion).
- Define the depth of the water table and ensure that it is below the MSTDA wall base.
- Define properties of the TDA backfill and granular bearing layer (total unit weight, gravimetric water content, friction angle), as well as properties governing interactions with any interfaces (interface shear strength or geosynthetic pullout factors).

Step 3: Establish the initial design configuration:

- Select an embedment depth for the MSTDA wall for a given toe slope.
- Select the height for the tallest section of the MSTDA wall.
- Define the batter of the MSTDA wall.
- Estimate the initial length of the geosynthetic reinforcements.

Step 4: Characterize allowable tensile strength of reinforcements and resistance factors

Step 5: Define nominal loads, load combinations, and load factors

Step 6: Evaluation of external stability

- Sliding
- Limiting eccentricity
- Bearing capacity of foundation soil beneath MSTDA wall

Step 7: Evaluate internal stability for MSTDA wall with geosynthetic reinforcements

- Define unfactored loads for critical failure surface expected for extensible geosynthetic reinforcements.
- Establish vertical spacing of geosynthetic reinforcements.
- Calculate factored horizontal stress and maximum tension at each reinforcement level.
- Calculate nominal and factored long-term tensile resistance of geosynthetic reinforcements.
- Select a geosynthetic reinforcement with the required tensile strength.
- Calculate nominal and factored pullout resistance of soil reinforcements and check spacing.
- Check connection resistance requirements at facing.

Step 8: Service limit state checks on TDA deformations

- Calculate TDA layer thicknesses using overbuild calculations that will result in the desired final lift heights and horizontal geosynthetic reinforcements.
- Estimate lateral wall movements.

Step 9: Global and compound stability (at service limit state)

Step 10: Check effects of seismic events (and other extreme events)

- External stability check
- Internal stability check

Step 11: Design wall drainage system

- Subsurface drainage.
- Surface drainage.

Establishing Initial Project Requirements and Material Parameters

The location selection of an MSTDA wall is typically driven by the need to repair a slope stability issue, widen a roadway lane, and/or to provide a change of grade. The MSTDA walls in California discussed in Chapter 5 were constructed for the purposes of repairing slope stability issues and to provide lane widening. A conventional gravity-type retaining wall with MSTDA was used to provide a lane widening and a change in grade along Route 91 in Riverside, CA (Humphrey 2008). After obtaining the initial site topology, the extents of the MSTDA wall should be defined. In most MSTDA walls used to repair slope instability issues, the height of the wall may not be uniform along the longitudinal extent of the wall, so it is important to identify the critical section for detailed design calculations. This is typically the section with the greatest height.

While the parameters for Type B TDA in Chapter 2 can be used in the design of MSTDA walls, the properties of the existing subgrade soils at the site should be characterized through a geotechnical site investigation. The extents of the geotechnical site investigation should be thorough enough to characterize the global stability of the MSTDA wall. They are also necessary to identify any geotechnical hazards including seismic hazards. Although there are many approaches for seismic site hazard analysis, for consistency with the design of MSE walls, the seismic hazard class should be characterized according to the AASHTO LRFD Bridge Design Specifications (AASHTO 2020). Other geotechnical hazards like liquefaction, global slope stability problems, etc. should be addressed but are not the scope of this report.

Two design variables that should be selected in this stage are the expected traffic surcharge load on the MTDA wall, and the thickness of the granular fill layer overlying the MSTDA wall. These two variables are linked and are based on the type of traffic loading. The minimum magnitude of a traffic surcharge recommended by AASHTO (2020) is a uniform load equivalent to 0.6 m (2 ft) of soil with a unit weight of 17 kN/m^3 (110 pcf) over the traffic lanes. This corresponds to a traffic surcharge of 10.2 kPa (220 psf). A typical traffic surcharge for heavier traffic loading is 17 kPa (350 psf). Although a minimum of 0.8 m of granular fill layer is permitted for unpaved roads, a greater thickness of 1 m or more should be selected for paved roads. Another consideration is to match the thickness of the granular fill layer with the gabion height used in the wall for ease of construction. For example, if a 0.6 m-tall gabion are being used, then a granular fill height of 1.2 m would be optimal so that it would extend through two gabion layers.

Initial MSTDA Design Configuration

One of the first steps in the detailed design of an MSTDA wall is to establish the initial geometric configuration of the wall, including the wall height, reinforcement type and length,

embedment depth, and facing batter angle. These key geometric features of an MSTDA wall are shown in Figure 3.1. Like MSE walls, MSTDA walls potentially have a wide range of geometric configurations, reinforcement types, and facing types. However, to be consistent with MSTDA walls constructed in California and recommendations in ASTM D6270-20, this report focuses on MSTDA walls with a single reinforced TDA layer with a maximum height of $H_{TDA} = 3 \text{ m}$ (10 ft) overlain by a granular fill material with a thickness ranging from $H_G = 0.8$ to 2 m , a horizontal back-slope, a flexible gabion-style facing with or without a batter, and extensible geosynthetic reinforcements. The height of the MSTDA wall used in internal and external stability calculations includes the TDA layer and the overlying granular fill material layer, and thus ranges from $H = 3.8$ to 5.0 m . The length and vertical spacing of the geosynthetic reinforcements are defined through an internal stability analysis that considers both the tensile resistance of the selected reinforcement, the structural resistance of the face elements and associated connections, and the pullout capacities of the reinforcement from TDA and granular backfill (if applicable). However, to start the design process, the minimum length of reinforcement can be estimated based on the total height of the MSTDA wall. For example, for MSE walls with horizontal backfill and static loading conditions, Berg et al. (2009) recommends a minimum reinforcement length L to wall height H ratio of $L/H = 0.7$. However, for seismic conditions, Berg et al. (2009) recommends a minimum L/H ratio of 0.8 to 1.1 . As mentioned, the toe of the MSTDA wall should be embedded a minimum of 0.6 m (2 ft) into the subgrade to minimize risks of scour. Greater embedment depths may be required for MSTDA walls on a slope. For example, Berg et al. (2009) recommends a minimum embedment of $H/7$ for walls on a $2H:1V$ slope and $H/5$ for walls on a $1.5H:1V$ slope. For more complex MSTDA wall configurations with different facing types or inextensible metallic reinforcements, the reader is referred to Berg et al. (2009) for guidance.

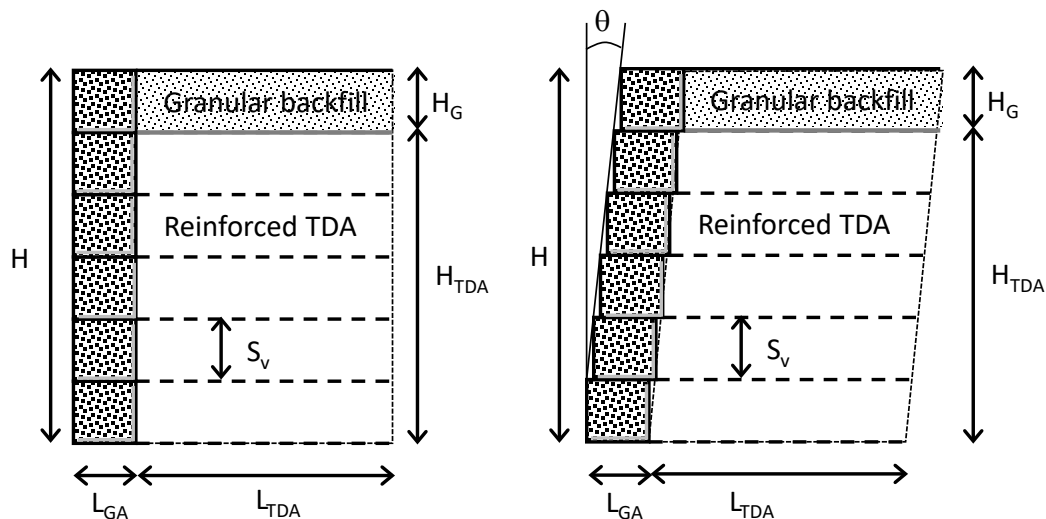


Figure 3.1: Definition of Key Geometric Variables of MSTDA Walls

The schematics in Figure 3.1 show horizontal dashed lines representing the geosynthetic reinforcements extending through the reinforced TDA. It is important to emphasize that the geosynthetic reinforcements should be horizontal after construction of the wall so that stresses in the TDA are effectively transferred to the geosynthetic reinforcements. The geosynthetic reinforcements can carry tensile stresses while the TDA cannot. Shear stresses are transferred

from the TDA to the geosynthetic reinforcements via friction and interlocking, mobilizing tensile stresses in the geosynthetic reinforcement. In this way, the TDA and geosynthetics in an MSTDA wall act as a composite material. If the geosynthetic reinforcements dip downwards due to settlement of the TDA (which would occur if overbuild is not considered), the stress transfer in the MSTDA wall may not be as expected.

Strength Properties of Geosynthetic Reinforcements

The geosynthetic reinforcement used in MSTDA walls could be affected by creep, installation damage, and durability issues. Durability issues may arise due to chemical degradation of the polymer. Elevated temperatures may affect both the creep process and the chemical degradation process. The available long-term tensile strength T_{al} of a geosynthetic reinforcement in terms of force per unit width is defined as:

$$T_{al} = \frac{T_{ult}}{RF_{ID} \times RF_{CR} \times RF_D} \quad (3.1)$$

where T_{ult} is the measured geosynthetic ultimate tensile strength (in terms of force per unit width) determined from a wide-width tensile test, RF_{ID} is the installation damage reduction factor, RF_{CR} is the creep reduction factor, and RF_D is the durability reduction factor. While the reduction in tensile strength of the geogrid will decrease immediately due to installation damage, the reductions in tensile strength due to creep and durability processes will occur over the entire design life of the MSTDA walls (which is targeted to be at least 75 years). Background on the characterization of the reduction factors is provided in Berg et al. (2009) and this report focuses on details relevant to geosynthetics in TDA).

Selection of the installation damage reduction factor for geosynthetic reinforcement in TDA is complex as a study has not been performed on the tensile strength of geosynthetic reinforcements before and after placement into Type B TDA. The installation damage of geosynthetics in TDA is expected to be less than the installation damage of geosynthetics in granular backfill as the vertical stresses in TDA are smaller and the TDA particles are less angular and are deformable. However, exposed steel wires may puncture or cut the geogrids. Installation damage can thus be mitigated by minimizing the amount of exposed steel wire and ensuring that there is at least 0.15 m (6 inches) of TDA covering the geosynthetics before driving a compactor over the lift. Berg et al. (2009) provides a Table of installation damage reduction factors for geosynthetics in different granular backfill soils that range from 1.1 to 1.45 for HDPE uniaxial geogrids (GGA) and polypropylene biaxial geogrids (GGC), and 1.1 to 1.85 for PVC coated PET geogrids (GGB). In the absence of additional data and assuming good quality control in minimizing the quantity of exposed steel, the lower bound on the installation damage reduction factor of 1.1 reported by Berg et al. (2009) can be used in design due to the characteristics of TDA.

The creep of geosynthetics in TDA is expected to be the same as observed for geosynthetics in soils. The creep reduction factor is mainly a function of the geosynthetic polymer and the geometric configuration of the geosynthetic. Berg et al. (2009) reported values of the creep reduction factors of 2.6 to 5 (average of 3.8) for HDPE (GGA), 1.6 to 2.5 (average of 2.05) for PET (GGB), and 4 to 5 (average of 4.5) for polypropylene.

The durability reduction factor for geogrids is complex and depends on the environment within the reinforced fill. Berg et al. (2009) noted that the durability reduction factor for most

geosynthetics ranges from 1.1 to 2.0. Many of the same variables that cause internal heating of TDA also affect the durability of geosynthetics, so following the guidelines in D6270-20 to reduce the effects of self-heating may help to minimize the susceptibility of geosynthetics to chemical attack, oxidation, or attack by microorganisms. Polypropylene and HDPE are both susceptible to oxidation, which requires the presence of oxygen. Berg et al. (2009) noted that the percentage of oxygen in reinforced fills with high porosity like TDA is similar to the percentage of oxygen in the environment. As noted, Finney (2018) noted increases in temperature of about 13° in TDA fills when wetted with fresh water, which could represent a worst case scenario for elevated temperatures in TDA fills constructed according to ASTM D6270-20. Due to the possibility for elevated temperatures, it is recommended to use the higher durability reduction factor of 2.0 for polypropylene and HDPE in conventional MSE walls reported by Berg et al. (2009) until further information is collected from long-term field experiments. Berg et al. (2009) reported that Polyester (PET) geosynthetics should only be used in lower pH environments, and that its durability reduction factor ranges from 1.15 to 1.3. Berg et al. (2009) recommend using a default durability reduction factor for PET of 1.3 unless more information is available.

Based on the preceding discussion, the total reduction factor obtained by multiplying the installation damage reduction factor of 1.1, average creep factors, and recommended durability reduction factors would be $1.1 \times 3.8 \times 2.0 = 8.4$ for HDPE, $1.1 \times 4.5 \times 2.0 = 9.9$ for polypropylene and $1.1 \times 2.05 \times 1.3 = 5.2$ for PET. Berg et al. (2009) recommends using a total reduction factor of 7 for the case that no information is available, and notes that geosynthetic- and site-specific testing may help reduce the total reduction factor to 3 to 6. Due to the uncertainty about geosynthetic interaction with TDA, it may be advisable to use the higher total reduction factors for HDPE and polypropylene geogrids until additional information is available. In LRFD, the available long term tensile strength is further reduced by a resistance factor Φ to account for the potential of local overstress due to load nonuniformity and uncertainties in the long-term strength. Berg et al. (2009) recommends using a resistance factor of $\Phi = 0.9$ for geosynthetic reinforcements.

Pullout of Geosynthetic Reinforcements from TDA and Granular Backfill

At the strength limit state of the wall, a failure surface will form through the wall, which can be represented by the Rankine failure surface as shown in Figure 3.2 (the inclination and potential nonlinearity of this failure surface will be discussed later). The materials to the left of the failure surface will want to slide downward while the materials to the right of the failure surface will stay stationary. It is possible that the reinforcements may either rupture when reaching the tensile strength discussed in the previous section, or they may pull out of the fill material. The pullout resistance of the geosynthetic reinforcement is defined by the ultimate tensile load required to generate outward sliding of the reinforcement through the reinforced soil zone. The pullout resistance can be defined by rearranging Equation 2.14 as follows:

$$P_r = F\alpha\sigma_v CL \quad (3.2)$$

where F is the pullout factor that depends on the vertical stress as shown in Figure 2.14, L_e is the length of embedment in the resistive zone behind the failure surface as shown in Figure 3.3, $C = 2$ for planar reinforcements, σ_v is the vertical stress at the depth of the soil-reinforcement interface, and $\alpha = 0.8$ for geogrids. Because the pullout resistance will increase with increasing vertical stress (which increases with depth in the wall), it is more likely that pullout will occur in the upper part of the wall). When defining the value of F in Equation 3.2, it is recommended to

use the experimental results in Figure 2.14 instead of using empirical or theoretical equations like those for granular backfills presented in Berg et al. (2009) due to the unique interaction between geosynthetic reinforcements and TDA. An exception would be the case where a woven geotextile reinforcement is used at the interface between TDA and the overlying granular backfill soil. In this case, the pullout resistance factor can be estimated as follows:

$$F = \tan \phi_{TDA-geotextile} \quad (3.3)$$

where $\phi_{TDA-geotextile}$ can be estimated from the shear failure envelope for TDA-aggregate in Table 2.1 for the vertical stress range of interest. This is reasonable as a nonwoven geotextile was used for separation and slippage occurred at the TDA-geotextile interface. Accordingly, using this value of F for both sides of the woven geotextile is conservative. Also, for woven geotextile reinforcements the value of $\alpha = 0.6$.

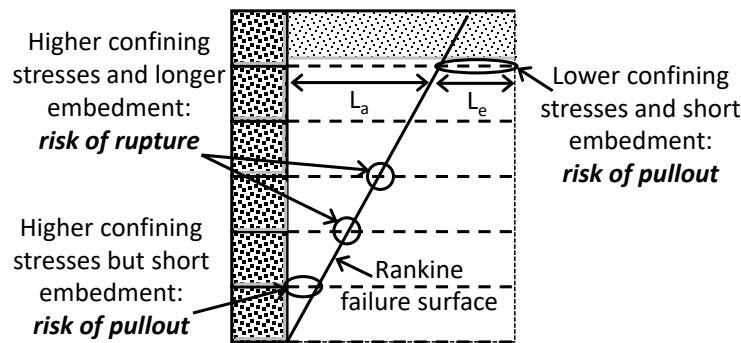


Figure 3.2: Internal Stability Modes in MSTDA Walls

LRFD Load Factors and Load Combinations

The main loads in MSTDA walls are the vertical loads associated with the self-weight of the TDA, granular fill, and traffic loading, and the horizontal loads associated with the earth pressure from the retained backfill and any pseudostatic earthquake forces. Based on the configuration of the MSTDA walls shown in Figures 1.1 and 3.1, the main permanent loads on an MSTDA wall are the horizontal dead load from the retained backfill (EH), the vertical dead load from the self-weight of the fill (TDA and granular backfill) (EV), and any permanent surcharge dead load (ES), while the main live loads are the earthquake live load (EQ) and the vehicular live load (LL). An example of a permanent surcharge dead load would be a pavement layer and granular base course that overlie the granular fill layer (which is included as part of the MSTDA wall fill). In this report, it is assumed that there are no permanent spread footings, live load surcharges, or vehicular collision forces in the design of MSTDA walls in this report, but they are considered in Berg et al. (2009). Load factors reported by Berg et al. (2020) for MSE walls defined based on recommendations from AASHTO (2020) are summarized in Table 3.1. Different load factors are applied to the different loads when investigating the wall at the strength limit state, the extreme event (seismic) limit state, and the service limit state. Further, many of the load factors have minimum and maximum values. The minimum load factors should be used when the load contributes positively to stability, and the maximum load factors should be used when the load contributes negatively to stability. For example, Berg et al. (2009) noted that in sliding analyses, the vertical dead loads ES and EV contribute positively to the friction developed at the base of the MSTDA wall, so the minimum load factors should be used, while the horizontal

dead load EH contributes negatively to the sliding resistance so the maximum load factor should be used. In a bearing capacity analysis, both the vertical dead load(s) and the horizontal dead load(s) contribute negatively so the maximum load factors should be used.

Table 3.1: Suggested Load Factors for MSTDA walls (Berg et al. 2009; AASHTO 2020)

Limit State	EH	ES	EV	LL	EQ
Strength Limit State	0.9 to 1.5	0.75 to 1.5	1.0 to 1.35	1.75	-
Extreme Event (Seismic) Limit State	0.9 to 1.5	0.75 to 1.5	1.0 to 1.35	Γ_{EQ}	1.0
Global Stability	-	1.0	1.0	—	-
Service Limit State	1.0	1.0	1.0	-	-

Note: GEQ is the load factor for live load applied simultaneously with the seismic load

A schematic with the definitions of the nominal loads (i.e., the loads before application of any load factors) is shown in Figure 3.3. The friction angles and unit weights are shown for the three material types in the MSTDA wall, the TDA, the granular fill layer, and the gabion fill material. The active earth pressure coefficient for the backfill is defined as follows:

$$K_{ab} = \begin{cases} \tan^2 \left(45 - \frac{\phi_b}{2} \right) \\ \frac{\sin^2(\theta + \phi_b)}{\sin^3(\theta) \left[1 + \frac{\sin\phi}{\sin\theta} \right]} \end{cases} \quad (3.4)$$

where the subscript b is for either the granular fill layer or the TDA, the top form of the equation is from the Rankine theory and should be used for vertical walls, and the bottom form of the equation should be used for walls with a batter angle greater than $\theta=10^\circ$. Tweedie et al. (1998a, 1998b) measured the value of K_{aTDA} in experiments on Type A TDA next to rigid concrete retaining walls and found that for horizontal wall deflections of 1% of the wall height the value of K_{aTDA} ranged from 0.22 to 0.25. For the geometry of the MSTDA wall shown in Figure 1.1 with a 1.2 m-thick granular fill layer, the value of ϕ_{sec} for Type B TDA will vary from 36.2° at the toe of the wall to 39.5° at the top of the TDA layer. Using these values of secant friction angles, the calculated values of K_{aTDA} range from 0.257 at the toe to 0.222 at the top of the TDA layer, which are close to the range of values reported by Tweedie et al. (1998a, 1998b). Accordingly, it is reasonable to calculate the values of K_{aTDA} used in stability analyses using Equation 3.4. For simplicity, in the design calculations for stability calculations, it is assumed that the earth pressure in the TDA layer increases linearly with depth, corresponding to a constant average friction angle. For the scenario mentioned above, this corresponds to an average friction angle of 37.8° for the Type B TDA layer.

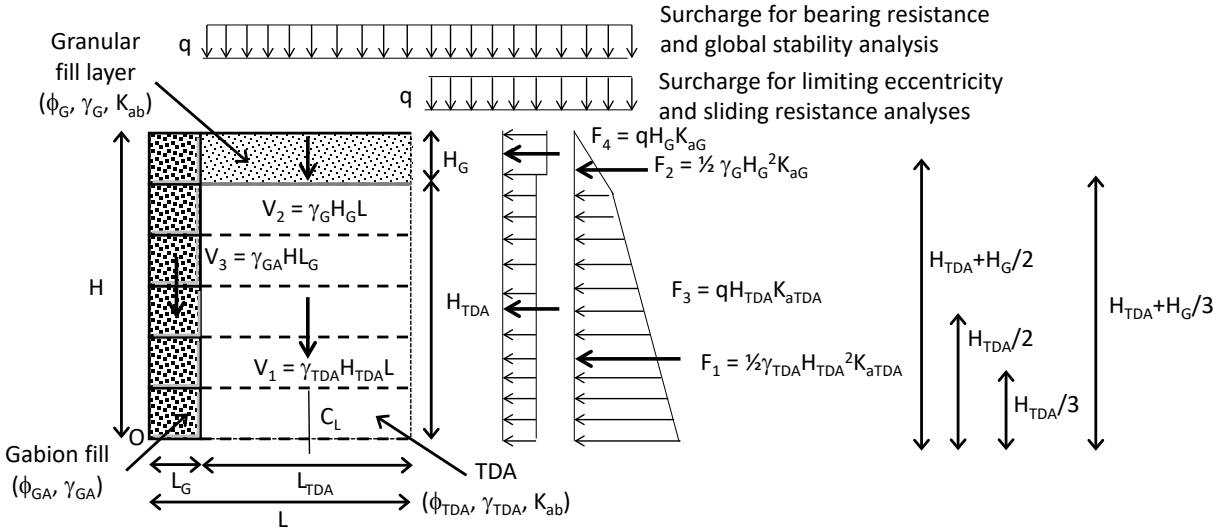


Figure 3.3: Definition of Nominal Loads for an MSTDA Wall (same definitions for an MSTDA wall with a batter)

External Stability Analysis

The reinforced fill (both TDA and the overlying granular backfill layer) in an MSTDA wall is assumed to act as a rigid body for the purposes of assessing the external stability of the MSTDA wall. Four main external stability modes are considered in this section and are summarized in Figure 3.4. The external stability modes include sliding along the base of the wall, overturning, which is referred to as limiting eccentricity, bearing capacity of the material underneath the wall, and global stability of the material surrounding the wall. The resistance factors are different for each of the external stability modes as different materials are involved in each mode. In the sliding mode, the resistance is related to the interface shear strength between the TDA and the subgrade, and the resistance factor is equal to 1.0. In the bearing resistance mode, the shear strength of the subgrade soil must be considered which has a greater uncertainty than the backfill materials. Accordingly, the resistance factor for bearing resistance is 0.65. For the global stability mode, the shear strength of the subgrade soil is also considered. When the geotechnical properties of the subgrade are well characterized or when the slope does not support a structural element, the resistance factor can be set at 0.75, while in the case that the geotechnical properties are based on limited information, or the slope supports a structure a lower resistance factor is set at 0.65. In the limiting eccentricity mode, the moment equilibrium of the horizontal and vertical loads is considered so the material resistance does not need to be considered.

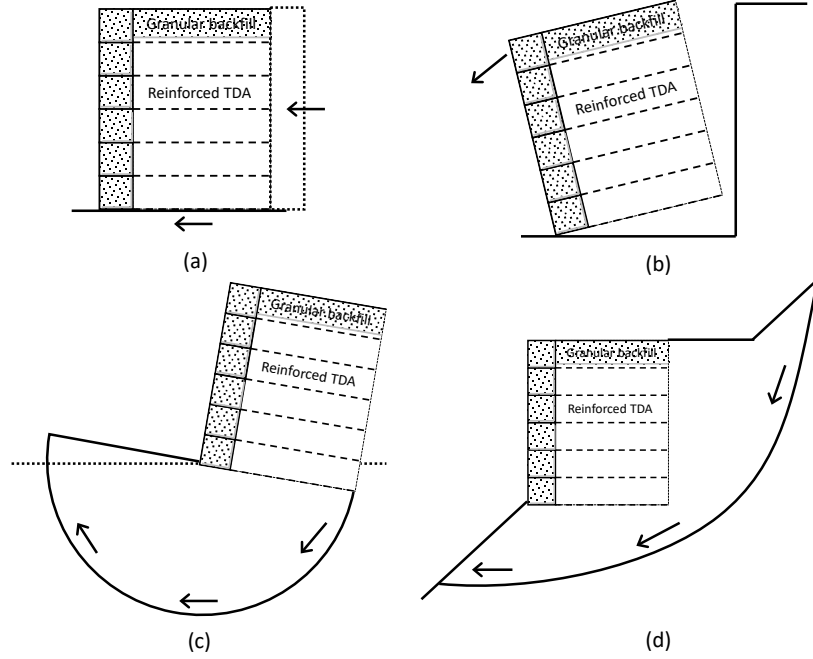


Figure 3.4: External Stability Modes for MSTDA walls: (a) Sliding; (b) Limiting Eccentricity; (c) Bearing Capacity; (d) Example of Global Stability (note that the critical failure surface for global stability may also go through the MSTDA wall)

Sliding

Sliding may occur when the horizontal stresses induced by the retained backfill and the effects of the surcharge are greater than the frictional resistance along the base of the MSTDA wall. The factored resistance R_f against failure by sliding can be calculated as follows:

$$R_f = \Phi \left[\frac{\Gamma_{EV}(V_1 + V_2 + V_3)}{L \times 1} \right] (L \times 1) \tan \phi_{TDA-Soil} \quad (3.5)$$

where the resistance factor is $\Phi = 1.0$, L is the total length of the MSTDA wall (including the length of the reinforced backfill L_{TDA} and the length of the gabion L_{GA}), the load factor Γ_{EV} is 1.0 (as the vertical self-weight leads to an increase in frictional sliding resistance), V_1 , V_2 , and V_3 are defined in Figure 3.3, and $\phi_{TDA-soil}$ is the friction angle between the TDA and a given soil separated by a nonwoven geotextile. Table 2.1 includes friction angles between TDA, sand and aggregate base, which could be used as preliminary estimates for $\phi_{TDA-soil}$. Although the interface shear strength between the gabion and the subgrade will be higher than that between the TDA and subgrade, the value of $\phi_{TDA-soil}$ can be used for the entire base width of the MSTDA wall to be conservative. The passive reaction caused by the embedment of the gabion should be ignored. In the case that the interface is nonlinear, the secant friction angle at the normal stress associated with the vertical stress (the term in bracket) can be defined. The factored load F_f contributing to failure by sliding is defined as follows:

$$F_f = \Gamma_{EH}(F_1) + \Gamma_{EH}(F_2) + \Gamma_{LS}(F_3) + \Gamma_{LS}(F_4) \quad (3.6)$$

where the dead load factor is $\Gamma_{EH} = 1.5$, the live load factor is $\Gamma_{LS} = 1.75$, and F_1 , F_2 , F_3 , and F_4 are defined in Figure 3.3. If the value of R_f is less than F_f , then a greater length of the reinforced zone L should be selected, and the calculations should be repeated.

Limiting Eccentricity

The check on limiting eccentricity essentially evaluates the moment stability of the MSTDA wall about the point O shown in Figure 3.3. The eccentricity e_c is the distance between the resultant downward foundation load and the center line (C_L) of the reinforced zone. The value of e_c should be less than $e_{c,max} = L/4$ for a soil subgrade or less than $e_{c,max} = 3L/8$ for a rock subgrade (Berg et al. 2009). If e_c is greater than $e_{c,max}$, a greater value of L (and thus L_{TDA}) is required and the external stability checks should be repeated. The value of e_c can be calculated as follows:

$$e_c = \frac{\Sigma M_D - \Sigma M_R}{\Sigma V} \quad (3.7)$$

where ΣM_D is the sum of driving moments, ΣM_R is the sum of resisting moments, and ΣV is the sum of vertical forces acting on a reinforced mass. To be conservative, the resisting moments are neglected in the eccentricity calculation. Accordingly, for the force diagram shown in Figure 3.3, the factored eccentricity can be calculated as follows:

$$e_c = \frac{\Gamma_{EH}(F_1)\left(\frac{H_{TDA}}{3}\right) + \Gamma_{EH}(F_2)\left(H_{TDA} + \frac{H_G}{3}\right) + \Gamma_{LS}(F_3)\left(\frac{H_{TDA}}{2}\right) + \Gamma_{LS}(F_4)\left(H_{TDA} + \frac{H_G}{2}\right)}{\Gamma_{EV}V_1 + \Gamma_{EV}V_2 + \Gamma_{EV}V_3} \quad (3.8)$$

where the load factors for the horizontal loads are the maximum values in Table 3.1 while the load factors for the vertical loads are the minimum values in Table 3.1. An MSTDA wall with a battered face will have a smaller eccentricity than a MSTDA wall with a vertical face, and the centroids of the vertical forces in Equation 3.8 should be used for the driving moment calculations.

Bearing Capacity and Settlement of Subgrade under MSTDA Wall

The bearing capacity of the subgrade soil beneath the MSTDA wall depends on the characteristics of the subsurface soils and has both strength limit state implications (bearing failure of the subgrade) as well as service limit state implications (excessive settlements of the subgrade). Regarding the strength limit state, the factored vertical stress applied on the subgrade by the MSTDA wall should be less than the factored bearing resistance. The bearing stress per unit width of the wall can be calculated as follows:

$$\sigma_{v,bearing} = \frac{\Gamma_{EV}V_1 + \Gamma_{EV}V_2 + \Gamma_{EV}V_3 + \Gamma_{LS}qL_{TDA}}{L - 2e_B} \quad (3.9)$$

where the eccentricity e_B is different from that calculated in Equations 3.6 and 3.7 as the impact of the surcharge should be included in the denominator. This definition of the vertical stress

indicates that the vertical stress distribution due to an eccentrically loaded structure can be approximated by a uniform stress distribution acting over a reduced area at the base of the wall. The total width L of the MSTDA wall is used in the bearing capacity calculation because of the relatively large weight of the gabion compared to the weight of the TDA backfill. The value of eccentricity for bearing capacity is given as follows:

$$e_B = \frac{\Gamma_{EH}(F_1)\left(\frac{H_{TDA}}{3}\right) + \Gamma_{EH}(F_2)\left(H_{TDA} + \frac{H_G}{3}\right) + \Gamma_{LS}(F_3)\left(\frac{H_{TDA}}{2}\right) + \Gamma_{LS}(F_4)\left(H_{TDA} + \frac{H_G}{2}\right)}{\Gamma_{EV}V_1 + \Gamma_{EV}V_2 + \Gamma_{EV}V_3 + \Gamma_{LS}qL_{TDA}} \quad (3.10)$$

where the value of Γ_{EV} should be the maximum value of 1.35 in Table 3.1. The resisting moments are neglected in the definition of e_B , and only positive values of e_B are used in Equation 3.6.

The nominal ultimate bearing resistance q_{ult} of the subgrade soil depends on whether it will act in an undrained or drained manner during the duration of the construction of the MSTDA wall. For example, saturated clays will typically behave in an undrained manner where the shear strength of the subgrade does not depend on the applied vertical stress (i.e., $\tau_f = c_{u,subgrade}$, where τ_f is the shear stress at failure and $c_{u,subgrade}$ is the undrained shear strength of the subgrade), while sands and gravels will behave in a drained manner where the shear strength of the subgrade increases with the applied vertical stress (i.e., $\tau_f = c'_{subgrade} + \sigma'_v \tan \phi'_{subgrade}$, where $c'_{subgrade}$ and $\phi'_{subgrade}$ are the effective cohesion and friction angle of the subgrade, respectively). The value of q_{ult} for drained subgrade soils assuming a horizontal toe slope can be defined as follows:

$$q_{ult,drained} = c'_{subgrade}N_c + q_D N_q + 0.5\gamma_{subgrade}N_\gamma \quad (3.11)$$

where N_c , N_q , and N_γ are bearing capacity factors that depend on the friction angle of the subgrade and can be defined using different relationships available in the literature (see Berg et al. 2009, AASHTO 2020, or most foundation engineering textbook), q_D is the surcharge due to the wall embedment, and $\gamma_{subgrade}$ is the unit weight of the subgrade. This equation assumes that all shape factors, depth factors, and other factors are equal to 1.0. Berg et al. (2009) assumes that $q_D = 0$ to be conservative, so the second term on the right-hand side drops out. Many drained soils do not have a cohesion value unless they are cemented or unsaturated, so care should be taken in the choice of $c'_{subgrade}$. The value of q_{ult} for undrained soils can be defined as follows:

$$q_{ult,undrained} = c_{u,subgrade}N_c \quad (3.12)$$

where $N_c = 5.14$. In the case that the subgrade is rock, an advanced bearing capacity analysis may be necessary, and the reader is referred to a textbook on Rock Mechanics.

A resistance factor of 0.65 should be applied to the nominal ultimate bearing capacity values for the subgrade soils to compare it with the factored vertical stress from Equation 3.6 (Berg et al. 2009). If the factored ultimate bearing capacity value is smaller than the factored vertical stress, then the length of the reinforced fill zone should be increased. However, Berg et al. (2009) notes that increasing L may not lead to major improvements, so they recommended performing additional testing on the subgrade soil. It may be possible to perform ground improvement to address the bearing capacity issues. Finally, the settlement of the subgrade soil should be

calculated using a version of the factored vertical stress in Equation 3.6 that uses the load factors at the service limit state (all are equal to 1.0). The settlement analysis for an areal fill may be used as part of this calculation. This analysis uses Equations 2.6 and 2.7 to estimate the change in height of the subgrade layer, with the values of C_c , C_r , and the yield stress for the subgrade soil. A consolidation analysis should be performed to ensure that these settlements will not take longer than the time of construction to apply, as the final height of the wall can be adjusted during construction. If it is anticipated that large settlements will occur after the end of construction then techniques like preloading, wick drains, or stone columns could be used. In general, it is anticipated that MSTDA walls will lead to lower subgrade settlements than conventional MSE walls due to the lower unit weight of TDA. However, if large settlements are calculated using the uniform vertical stress defined in Equation 3.6, this may imply that differential settlements may occur as the gabion fill material will be heavier than the TDA. If this is the case, then ground improvement may be necessary.

Internal Stability Analysis

The two modes of failure in an internal stability analysis in an MSTDA wall are when the geosynthetic reinforcements rupture or elongate excessively or when the geosynthetic reinforcements pull out of the TDA or granular backfill layer. The main outcomes of the internal stability analyses are checks on the reinforcement length and a selection of the reinforcement vertical spacing S_v . The first step in the internal stability analysis is to identify the critical failure surface in the MSTDA wall. While the failure surface in the TDA will likely be nonlinear due to the shape of the failure surface for Type B TDA shown in Figure 2.8, this report will assume a linear Rankine failure surface like that in Figure 3.2 for simplicity. This failure surface is inclined from vertical at an angle in degrees of $45-\phi/2$. Rankine's active earth pressure theory assumes lateral pressure is independent of backfill slope and interface friction. The average friction angle of Type B TDA corresponding to the unfactored permanent vertical stresses (i.e., the thickness of the granular fill layer and the TDA layer) in an MSTDA wall should be used in this case. For the granular layer thicknesses ranging from 0.8 to 2.0 m and typical unit weights for Type B TDA and granular fill, this corresponds to average friction angles for Type B TDA of 40° to 35° , respectively. These values of average friction angle are given for example only, and the actual average value considering the actual thickness and total unit weight of the granular fill layer as well as the increase in unit weight of the TDA after compression should be used in defining the average friction angle of Type B TDA. It should also be noted that for the critical slip surface to form in the TDA layer that relatively large displacements will need to occur (approximately 0.8 m as noted in Figure 2.6). Application of the load and resistance factors in the internal stability analysis will ensure that the shear stresses in the TDA mass will not approach failure, which will limit the deformations observed. If there are concerns about shear-induced TDA deformations due to the formation of a critical shear plane, a lower resistance factor than that used in MSE walls ($\Phi=0.9$ for static loading) can be used in MSTDA walls to reduce the magnitude of expected shear stresses in the TDA mass. However, until more information is available, it is recommended to use the same resistance factor for MSE walls especially as the gabion facing will provide an additional stabilizing force to the TDA mass that is not considered in the internal stability analysis.

Rupture Check and Vertical Spacing Definition

The next step is to establish the vertical layout of reinforcements in the MSTDA wall by comparing the induced tensile stresses in the reinforcement and the factored tensile resistance of the reinforcements. The geosynthetic reinforcements will provide tensile reinforcement both to the TDA layer as well as the overlying granular fill layer. The minimum vertical spacing S_v of the geosynthetic reinforcements is the compaction lift thickness adjusted to consider the effects of overbuild that will be discussed in the next section. The most common compaction lift thickness for TDA based on experience from Humphrey (2008) is 0.15 m (6 inches). Berg et al. (2009) notes that the most typical vertical spacings of tensile reinforcements are 1, 2, or 3 times the compaction lift thickness. It is most common to place and compact a lift of fill, then place a tensile reinforcement, then continue placing lifts of fill. Berg et al. (2009) also notes that the maximum vertical spacing permitted in MSE walls is 0.8 m (32 inches). Another consideration in MSTDA walls is the height of an individual gabion layer. It is common in gabion walls that the level of each gabion coincides with a layer of geosynthetic reinforcement, so that the geosynthetics can be connected between the gabion layers. However, it is possible to add additional secondary reinforcements between the levels of the gabions if necessary for design. Berg et al. (2009) notes that MSE walls with granular backfill and a gabion facing have been constructed with a vertical spacing equal to gabion heights up to 0.9 m (3ft), which is larger than the maximum spacing mentioned above. However, Berg et al. (2009) notes that the length of the gabion L_{GA} improves the internal stability by preventing bulging. Nonetheless, due to the large deformations possible in TDA, this practice is not recommended for MSTDA walls and the vertical spacing calculated from an internal stability analysis should be used (rounded down to the nearest lift thickness).

The next step in analyzing the internal stability is to calculate the factored horizontal stress at the depth of in each reinforcement layer, as follows:

$$\sigma_h = \Gamma_{EV}(\sigma_v K_{ab} + q K_{ab}) \quad (3.13)$$

where the tensile force is assumed to equal the active horizontal stress at the level of each reinforcement, the load factors for both live loads and dead loads are defined as the maximum value for the vertical loads (1.35) and the vertical stress at a given depth is calculated according to the self-weight of the granular backfill layer and the TDA. It is important to note that when calculating the vertical stress, the TDA total unit weight will increase by a factor of 1.21 to 1.47 from the value after compaction due to the application of overlying layers (considering both compression and creep effects). Note that the overbuild calculations that will be discussed later should be performed to calculate the values of vertical stress in Equation 3.13, and the overbuild calculations may need to be revised if a smaller spacing is required. The factored tensile loads in each reinforcement layer are calculated using the vertical spacing for each layer as follows:

$$T_{max} = \sigma_h S_v \quad (3.14)$$

where the vertical spacing is defined as the tributary distance from the nearest two unreinforced heights. Throughout the height of the wall, the value of S_v will likely be uniform (i.e., the distance between the middle of each reinforced layers) but at the top and bottom the values of S_v may be different (i.e., the distance from the unreinforced bottom or top and the middle of the next

reinforced layer). The factored tensile load can then be compared with the factored tensile resistance, given by combining Equation 3.1 with the resistance factor:

$$T_{al,f} = \Phi T_{al} \quad (3.15)$$

The value of resistance factor Φ is equal to 0.9 for static loading (rupture or pullout) and 1.2 for combined static loading and earthquake loading. By comparing $T_{al,f}$ with the maximum value of T_{max} calculated in the wall, the geosynthetic product can be selected or refined, and the vertical spacing can also be refined. Although three geogrids commonly used in MSTDA walls were characterized in Chapter 2, the manufacturers of these geogrids often have similar uniaxial geogrids that have greater ultimate strengths. If the vertical spacing is reduced, the spacing should still be an integer multiple of the TDA lift height for practical purposes.

Pullout Check

After refining the spacing to account for rupture of the geosynthetic reinforcements, a check on the pullout resistance is performed to assess that the length of embedment in the resistive zone, L_e is adequate:

$$\Phi L_e > \frac{T_{max}}{F\alpha\sigma_v C} \quad (3.16)$$

where T_{max} is from Equation 3.11 and the resistance factor Φ is equal to 0.9. The values of L_e at different depths from the top of the reinforced fill in the MSTDA wall can be calculated as follows:

$$L_e = L_{TDA} - (H - Z)\tan\left(45 - \frac{\phi_b}{2}\right) \quad (3.17)$$

where Z is the depth from the top of the fill, and ϕ_b is the friction angle of the granular fill or TDA. If L_e needs to be increased so that the geosynthetic has sufficient pullout strength at a given depth Z , then Equation 3.14 indicates that the total length of the geosynthetic should be increased.

Facing Connection Strength Check

The facing connection strength should be designed to carry the value of T_{max} calculated from Equation 3.11 at each of the depths in the wall. For gabions in MSTDA walls, the connection is expected to be frictional between the gabion backfill material and the geosynthetic reinforcement. This means that the geosynthetic reinforcements should be placed so that they overlap with the full length of the gabion L_{GA} . The factored connection strength for a vertical gabion wall can be estimated as follows:

$$T_{connection,f} = \Phi 2L_{GA}\sigma_{v,GA}\tan\phi_{GA-geosynthetic} \quad (3.18)$$

where Φ is the resistance factor of 0.9, $\sigma_{v,GA}$ is the vertical stress in the gabion calculated using the depth from the top of the gabion facing, and $\phi_{GA-geosynthetic}$ is the friction angle for the interface between the gabion fill and the geosynthetic. The factor of 2 is to account for friction on the top and bottom of the geosynthetic reinforcement. For MSTDA walls having a height less than 5 m and a gabion batter less than 8 degrees, Equation 3.18 can be used to estimate the connection strength. However, for MSTDA walls with a larger gabion batter angle, the length of the overlap between any two gabions will reduce and the vertical stress on a given gabion may reduce as the

center of gravity of the gabions may shift away from the edge of the gabions. The analysis in Figure 4-17 of Berg et al. (2009) can be used to estimate the vertical stress on the gabions.

Considerations for TDA Compression: Overbuild

After selection of the vertical spacing of the reinforcements in the internal stability analysis, it is important to calculate the overbuild for each of the lifts. This is calculated by dividing the MSTDA wall into layers corresponding to each of layers with a geosynthetic reinforcement and defining an initial thickness of each of the layers (most commonly the final target thickness). As mentioned in Chapter 2, the experimental data for the compression curves of Type B TDA start from relatively high void ratios that correspond to lower dry unit weights from compaction than encountered in the construction of MSTDA walls in the field. Accordingly, an approach was developed to use the same values of C_r and C_c from the experiments, but to use a larger yield stress, as shown in Figure 3.5. For a dry unit weight of 7 kN/m^3 in the field, the recompression line can be shifted downward to have an apparent yield stress of 70 kPa with the virgin compression line. If other dry unit weights are encountered in a field project, a similar approach can be used to shift the recompression line upward or downward to define the apparent yield stress for a given project.

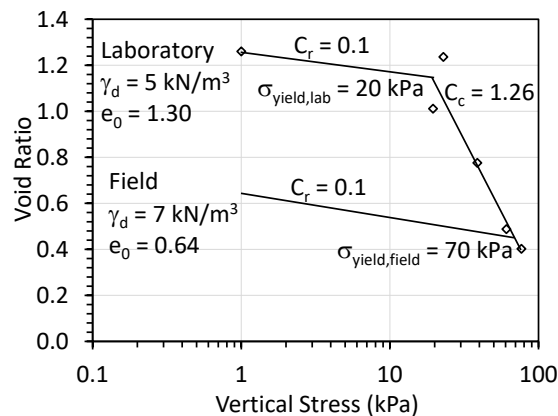


Figure 3.5: Compression Curve of Type B TDA from Laboratory Experiments

The change in thickness of each layer and underlying layers due to the application of all overlying layers is then calculated using Equations 2.6 and 2.7. As part of this calculation, it is more accurate to break the layers up into multiple sublayers. The initial vertical stress at the center of each sublayer should be calculated. Next, the vertical stress corresponding to the granular fill layer is calculated and is applied as a change in stress to all the underlying layers. Equations 2.6 and 2.7 are then used to calculate the change in thickness of each TDA layer due to external stresses, and this can be added to the change in thickness of each TDA layer due to creep using Equation 2.8. It is important to consider the effects of creep but should be noted that the change in thickness due to creep of Type B TDA is a small fraction of the change in thickness due to application of external vertical stresses, even when considering long durations of creep. A solver is then used to identify the initial thickness of the TDA layer that will have a final thickness corresponding to the target elevations of each lift after placement of the overlying TDA layers and the granular fill layer. The results of an overbuild analysis for TDA Type B for a Target lift

thickness of 3 m and a total TDA height of 3 m for different thicknesses of granular fill layers is shown in Figure 3.5, where TDA lift number 1 is at the bottom of the MSTDA wall.

The overbuild results are shown in terms of the cumulative overbuild with increasing height in the wall in Figure 3.6(a) and in terms of the individual lift overbuild in Figure 3.6(b). A permanent pavement surcharge of 8 kPa and a creep duration of 10 years were used in the calculations. The results in Figure 3.6(a) indicate that when using a 2 m-thick granular fill layer, an overbuild of 0.31 m of TDA should be added to the wall to make sure that its final thickness is 3 m. This is very close to the amount of overbuild of 0.24 m predicted in the chart of Humphrey (2008) shown in Figure 2.5 for Type A TDA and the same loading condition. The results in Figure 3.6(b) indicate that more TDA should be added to the lower layers in the MSTDA wall as they will experience greater changes in thickness after self-weight loading. Due to the overbuild, the TDA unit weight will increase from the value after compaction, as shown in Figure 3.7. It is important to consider the effects of this final unit weight when calculating the maximum tensile stresses in the TDA, so it may be necessary to revisit the internal stability analysis and lengthen the reinforcements in case pullout becomes a concern or to decrease the vertical spacing in case the maximum factored tensile stress exceeds the factored tensile resistance of the reinforcements.

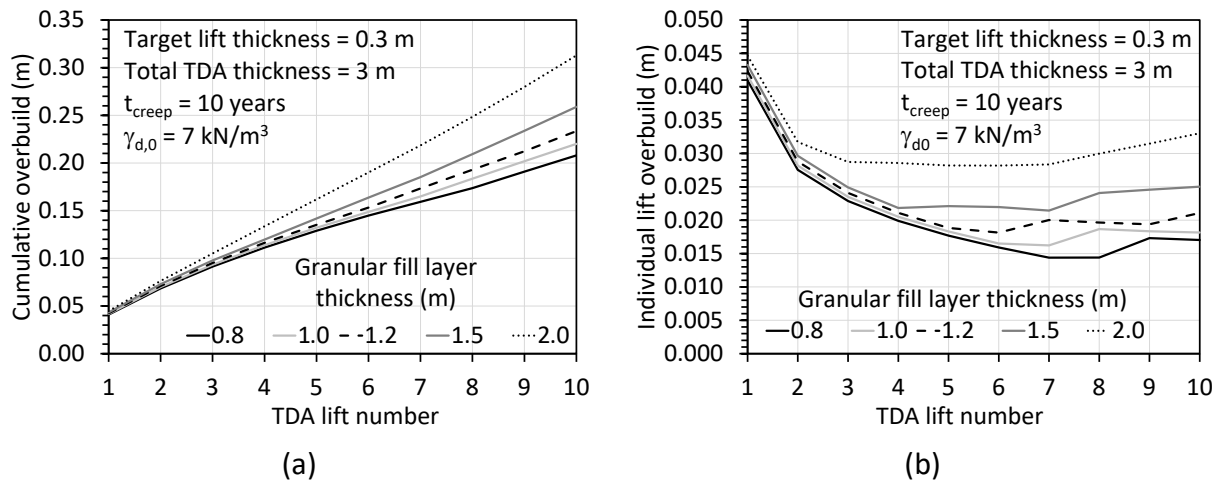


Figure 3.6: Sample Overbuild Calculations for MSTDA Walls with a Maximum TDA Thickness of 3 m and Different Granular Fill Layer Thicknesses: (a) cumulative; (b) Individual Lift Values

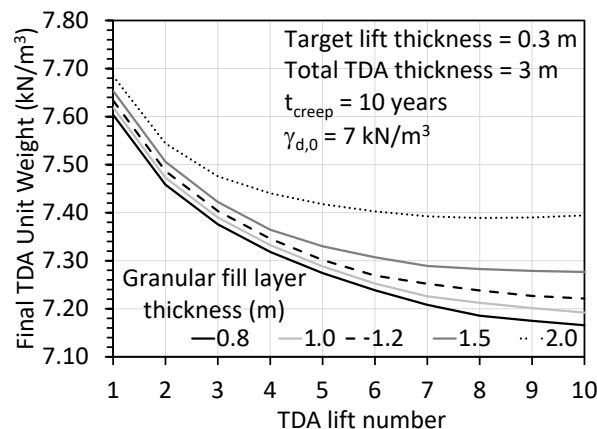


Figure 3.7: Distribution in Final Total Unit Weight of the TDA after Compression Under Overbuild.

The final total unit weights of TDA in Figure 3.7 can be used to calculate the profiles of effective stress in the TDA layer within an MSTDA wall as shown in Figure 3.8(a), accounting for the surcharge due to a pavement layer of 8 kPa and the self-weight of the overlying granular fill layer (which increases with the thickness of the granular fill layer). Although the final total unit weight of the TDA varies nonlinearly with height in the MSTDA walls, the effective stress profiles are still close to linear. The effective stresses can then be used to calculate the variation in the secant friction angle of the TDA using the parameters in Table 2.1, as shown in Figure 3.8(b). In this case, the secant friction angle clearly varies nonlinearly with height in the wall but within a relatively narrow range of approximately 3° for each of the fill layer thicknesses considered. Calculations like these can be used to estimate the average secant friction angle of the TDA to use in the internal stability calculations.

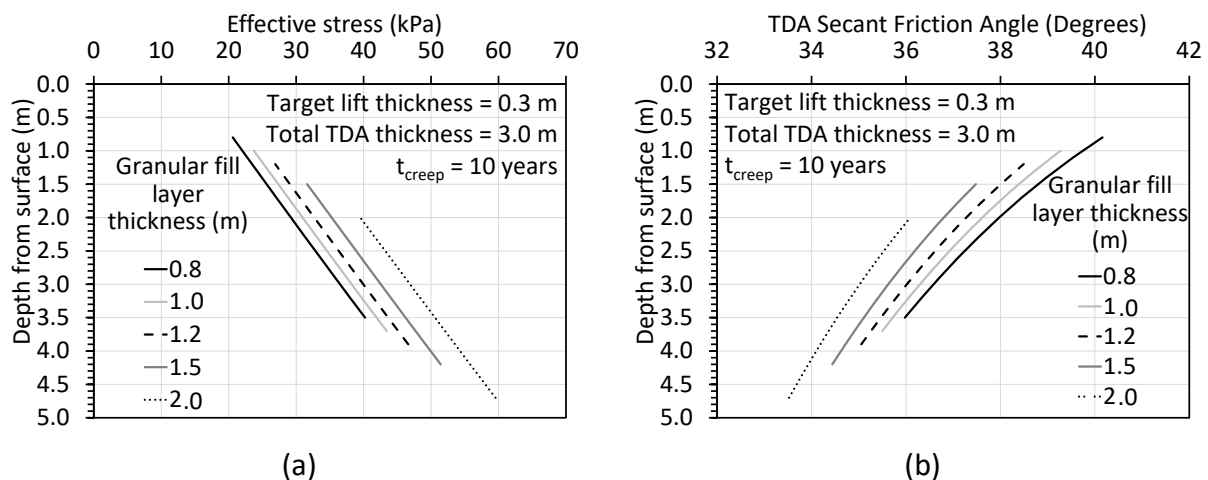


Figure 3.8: (a) Effective stress profiles in MSTDA walls with different granular fill layer thicknesses; (b) Variations in TDA secant friction angle with height in the MSTDA walls

In addition to the vertical compression and the need to overbuild the TDA layer, it may be challenging to compact TDA to high unit weights near a flexible facing as compaction may lead to lateral movements of the flexible facing. Most studies on the compaction of TDA have involved compaction into a container with rigid horizontal boundaries. The lateral movement of the facing in MSTDA walls should be carefully monitored and the target inclination may be achieved by placing the facing units with a larger batter than expected, or by controlling the position of the gabions while compacting the TDA. Berg et al. (2009) provides a chart to estimate the lateral facing displacement as a function of the L/H ratio. Lower displacements are expected when the L/H ratio is greater than 0.7. A lighter weight compactor may be suitable when within 1 m of the face of the MSTDA wall.

Drainage in MSTDA Walls

It is critical to provide adequate drainage in MSTDA walls to avoid adding weight to the retained backfill and reducing effective stresses. Although MSE and MSTDA walls can be designed to withstand the effects of water within the reinforced and retained fill, it is preferred to provide adequate drainage along the base of the wall so that groundwater or water infiltrating into the

fill can be captured and discharged. The surface layer of the MSTDA wall should be designed so that surface water runoff will be directed away from the wall so that it does not infiltrate into the backfill. Water should not be directed to the face of the wall to avoid concerns about degradation of the gabions or scour of the soil at the toe of the wall. Design details for different drainage elements are given in Section 5.3 of Berg et al. (2009).

Global Stability Analyses

Global stability analysis is typically performed using a software that can consider circular- or wedge-type failure surfaces. The reinforced TDA should be included in the analysis. Many proprietary software programs define the shear strength of geomaterials in terms of drained parameters (c' and ϕ') or undrained parameters (c_u), and a model to incorporate the nonlinear failure envelope for TDA is not available. In this case, two choices are available to represent the shear strength of the TDA, and both should represent drained conditions. The first is to use an average ϕ_{sec} value for the range of normal stresses present in an MSTDA wall using the same approach used when defining the average Rankine failure surface in the internal stability analysis. The second would be to fit a linear envelope with $c'_{apparent}$ and $\phi'_{apparent}$ that provides an approximate fit to the nonlinear failure envelope over the range of vertical stresses present in MSTDA walls. In this case, the value of $c'_{apparent}$ does not imply that the TDA has cohesion and is only a fitting parameter.

The global stability is performed at the service limit state, which means that all the load factors are equal to 1.0. As mentioned, the resistance factors for global stability are either 0.75 when the geotechnical parameters are well defined and the slope does not support or contain a structural element, or 0.65 when the geotechnical parameters are based on limited information or the slope supports or contains a structural element (Berg et al. 2009). As the global stability analysis is performed at the service limit state with load factors of 1.0, the resistance factor of 0.75 corresponds to a conventional factor of safety of 1.3 and the resistance factor of 0.65 corresponds to a conventional factor of safety of 1.5. This is useful as most slope stability programs only provide results in terms of the minimum factor of safety for a critical slip surface. Although the MSTDA wall should be designed with adequate drainage so that the TDA remains at low water contents, the global stability analysis should evaluate different worst-case scenarios for the water level and pore water pressures.

Extreme Event (Seismic) Stability Analyses

Due to their flexibility, MSE walls are resistant to dynamic forces developed during a seismic event, as confirmed by the excellent performance in several recent earthquakes and shake table experiments (e.g., E.-Emam and Bathurst 2007; Ling et al. 2012; Zheng et al. 2019). The seismic response of retaining walls constructed with TDA Type B has been evaluated in large-scale experiments recently by Xiao et al. (2013) and Ahn and Cheng (2014), who found that these systems have many positive seismic characteristics. TDA has also been used as a cushion material to damp out vibrations from compaction (Lee and Roh 2007), as a liquefaction mitigation measure (Hazarika et al. 2010), and as a seismic isolation method (Tsang 2008). Several studies have evaluated the dynamic properties of TDA with relatively small particle sizes and the effects of mixing with soils (Bosscher et al. 1997; Feng and Sutterer 2000; Kaneko et al. 2003; Ehsani et al. 2015). Fewer studies have measured the dynamic properties of Type B TDA due to the

requirement for a large testing device to accommodate the relatively large particle sizes (McCartney et al. 2017).

The seismic design of MSTDA walls starts with the initial wall design based on static loading considering both external and internal stability, including the actual total unit weight profile of the TDA shown in Figure 3.6. The next step is to establish the seismic hazard for the region of the MSTDA wall using a 1000 year return period using the seismic hazard maps in section 3.10.2 of AASHTO (2020). The expected peak ground acceleration (PGA) and spectral acceleration at a period of 1 second (S_1) should be selected from the maps. Next, the site effects should be established using Tables 3.10.3.2-1 and 3.10.3.2-3 in AASHTO (2020), respectively, including the site class (A, B, C, D, or E) and the site factors F_{PGA} and F_v . Using this information, the average maximum horizontal acceleration k_{av} and the peak ground velocity PGV can be estimated:

$$k_{av} = \alpha_H F_{PGA} PGA \quad (3.19)$$

$$PGV = 38 F_v S_1 \quad (3.20)$$

where α_H is a wall height dependent reduction factor that can be defined as follows for sites with soil subgrades (Site Class C, D, and E) as follows:

$$\alpha_H = 1 + 0.01H \left[0.5 \left(\frac{F_v S_1}{F_{PGA} PGA} \right) - 1 \right] \quad (3.21)$$

where the value of H should be entered in feet for this empirical equation. For sites with hard or soft rock foundations (Site Class A or B), the value of α should be increased by a factor of 1.2. As MSTDA walls are always less than 5 m (15 ft), the value of α be close to 1.0. Next, the total thrust due to both static and dynamic loading P_{AE} is calculated using the Mononobe-Okabe formulation as follows:

$$P_{AE} = 0.5 K_{AE} \gamma_{b,ave} H^2 \quad (3.22)$$

where $\gamma_{b,ave}$ is the average unit weight of the TDA and granular backfill layers in the MSTDA wall and K_{AE} is defined as follows:

$$K_{AE} = \frac{\cos^2(\phi_{b,ave} - \xi - \theta)}{\cos(\xi) \cos^2(\theta) \cos(\phi_{b,ave} + \xi + \theta)} \left[\frac{1 + \frac{\sin(2\phi_{b,ave}) \sin(\phi_{b,ave} - \xi)}{\cos(\phi_{b,ave} + \xi + \theta) \cos(-\theta)}}{\sqrt{\frac{\sin(2\phi_{b,ave}) \sin(\phi_{b,ave} - \xi)}{\cos(\phi_{b,ave} + \xi + \theta) \cos(-\theta)}}}} \right]^2 \quad (3.23)$$

where $\phi_{b,ave}$ is the weighted average of the friction angle in the MSTDA wall, considering the variation in secant friction angle of the TDA with depth and the friction angle of the granular fill layer, θ is the batter angle from the vertical plane, and the Mononobe-Okabe angle ξ is defined as follows:

$$\xi = \tan^{-1} \left(\frac{k_h}{1 - k_v} \right) \quad (3.24)$$

where k_h and k_v are horizontal and vertical seismic coefficients, respectively. Typically, k_h is assumed to equal k_{av} from Equation 3.19 and k_v is assumed to equal zero. The total thrust P_{AE} is assumed to act at a height of $H/2$ and is thus assumed to be uniformly distributed of the height of the reinforced fill of the MSTDA wall. The thrust P_{AE} is assumed to be inclined on the back edge of the reinforced mass for a horizontal backfill at an angle equal to $\phi_{b,ave}$, and thus has vertical and horizontal components that should be considered in stability analyses.

Next, the horizontal initial force P_{IR} of the total reinforced wall mass is calculated as follows:

$$P_{IR} = 0.5k_{av}W \quad (3.24)$$

where W is the weight of the full reinforced mass in the MSTDA wall (both TDA and overlying granular fill layer) and is equal to $V_1+V_2+V_3$ as defined in Figure 3.3. This inertial force is assumed to act horizontally on the centroid of the reinforced mass. The total horizontal force is the calculated as follows:

$$T_{H,EQ} = P_{AE}\cos(\phi_{b,ave}) + P_{IR} + \Gamma_{EQ}qK_{AE}H \quad (3.25)$$

where the load factor in this equation is Γ_{EQ} is equal to 1.0. The sliding resistance is then checked by comparing the total horizontal force in Equation 3.25 with the sliding resistance as follows:

$$R_{f,EQ} = \Phi \left[\frac{(V_1 + V_2 + V_3) + P_{AE}\sin(\phi_{b,ave})}{L \times 1} \right] (L \times 1)\tan\phi_{TDA-Soil} \quad (3.26)$$

using a resistance factor Φ equal to 1.0. If $R_{f,EQ}$ is greater than $T_{H,EQ}$, then the design is satisfactory for sliding resistance. Berg et al. (2009) provides a simple technique for estimating the wall sliding displacement that involves identification of the yield seismic coefficient obtained by plotting the resisting and driving horizontal forces in Equations 3.25 and 3.26 as a function of k_{av} and finding the intersection point. The value of k_y and PGV are then used in an empirical equation to estimate the seismic sliding displacement, which should be less than 50 mm (2 inches).

The same approach to modifying the applied loads in the limiting eccentricity and bearing capacity analyses should be followed, where the horizontal and vertical components of P_{AE} are added to the other applied loads considered in the static analysis. A resistance factor of 1.0 should be used in these calculations. The eccentricity value due to combined static and seismic loading should be within the middle eight-tenths of the wall when using a load factor Γ_{EQ} of 1.0.

Finally, internal stability should be checked by including an additional inertial load associated with the weight of the active wedge and facing. The additional inertial load associated with seismic loading can be calculated as follows:

$$P_i = k_{av}(W_a + V_3) \quad (3.27)$$

where V_3 is the weight of the facing blocks per unit meter and W_a is the weight of TDA and granular fill in the active wedge, which can be calculated as follows:

$$\begin{aligned}
W_a = & \gamma_{TDA} H_{TDA}^2 \tan\left(45 - \frac{\phi_{TDA}}{2}\right) \\
& + \frac{\gamma_G H_G}{2} \left(H_{TDA} \tan\left(45 - \frac{\phi_{TDA}}{2}\right) \right. \\
& \left. + (H_{TDA} + H_G) \tan\left(45 - \frac{\phi_G}{2}\right) \right)
\end{aligned} \tag{3.28}$$

It is assumed that the magnitude of P_i will be the same at all the heights of the reinforcements in the wall, and that the inertial force is distributed across all the reinforcements equally as follows:

$$T_{d,f} = \frac{P_i}{n} \tag{3.29}$$

where n is the number of reinforcements and $T_{d,f}$ is referred to as the factored tensile load due to dynamic (seismic) loading. The total tensile load in the reinforcements T_{total} for both static and dynamic loading is as follows:

$$T_{total} = T_{max} + T_{d,f} \tag{3.30}$$

where T_{max} was defined in equation 3.14. The ultimate strength of the geosynthetic should be greater than the factored sum of the total loading considering:

$$T_{ult} > \frac{T_{max} \times RF_{ID} \times RF_{CR} \times RF_D}{\Phi} + \frac{T_{d,f} \times RF_{ID} \times RF_D}{\Phi} \tag{3.31}$$

where the resistance factor Φ is equal to 1.2 for dynamic loading. The first term on the right-hand side in Equation 3.27 is the required resistance to static loading and the second term on the right-hand side is the required resistance to dynamic loading (and thus does not have a creep reduction factor). A check on the length of embedment against pullout for combined static and dynamic loading is given as follows:

$$L_e \geq \frac{T_{total}}{0.8\Phi F\alpha\sigma_v C} \tag{3.32}$$

where the resistance factor Φ is equal to 1.2 for dynamic loading and the factor of 0.8 is used to account for the uncertainty associated with dynamic pullout of geosynthetics from TDA. If dynamic pullout tests are performed, then this factor does not need to be included in Equation 3.32. Finally, the connection strength due to combined static and dynamic loading $T_{ult,connection}$ should be considered as follows:

$$T_{ult,connection} > \frac{T_{max} \times RF_D}{0.8\Phi} + \frac{T_{d,f} \times RF_D}{0.8\Phi} \tag{3.33}$$

where the resistance factor Φ is equal to 1.2 for dynamic loading and the factor of 0.8 is used to account for the uncertainty associated with dynamic shearing at the gabion fill-geogrid interface.

Chapter 4: Example Calculations for Design of an MSTDA Retaining Wall

This chapter summarizes the design steps for an example MSTDA wall in California.

Step 1: Establish project requirements:

The example MSTDA wall considered in this chapter is a 3 m-thick TDA layer overlain by a 1.2 m-thick granular fill layer, overlain by a roadway layer (0.1 m of hot mix asphalt overlying 0.3 m of class 2 aggregate base) applying a permanent surcharge stress of 8 kPa (167 psf). A traffic surcharge of 17 kPa (350 psf) was selected to represent traffic from heavy trucks. The wall configuration under consideration is shown in Figure 4. 1. The MSTDA wall was assumed to be installed on a slope with an inclination of 3H:1V. The reinforcements are assumed to be geogrids (GGB was selected as this type was also used in one of the case histories in the next chapter), except for a woven geotextile separating the TDA from the granular fill layer. The woven geotextile was assumed to have similar properties to the geogrid for simplicity in the design.

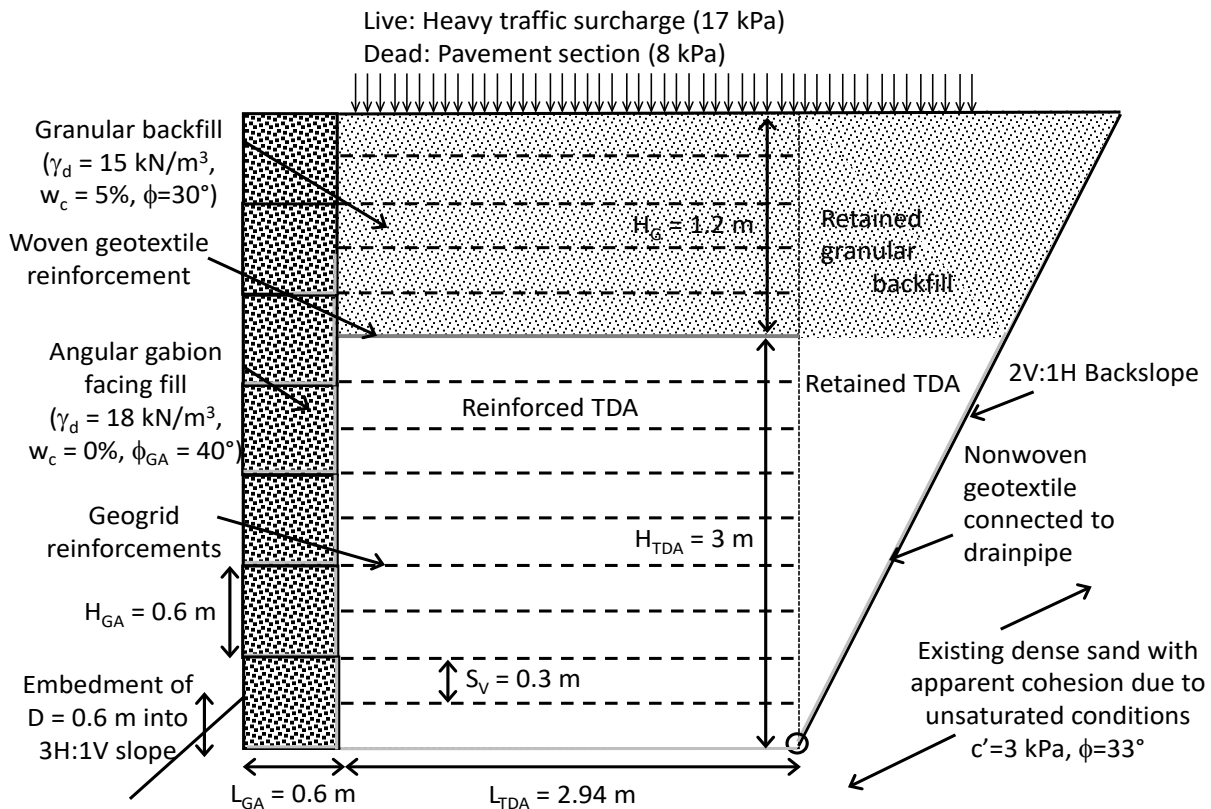


Figure 4.1: Initial Configuration of an MSTDA Wall Considered in the Design Example

Step 2: Establish project material parameters:

The properties of Type B TDA summarized in Chapter 2 are used to represent the behavior of the TDA in the wall. The granular fill layer is set to have a dry unit weight of 15 kN/m^3 , a compaction water content of 5%, and a friction angle of 33° with no cohesion. The gabion fill was assumed to be dry angular fill with a friction angle of 40° with no cohesion and a total unit weight of 18 kN/m^3 .

Step 3: Establish the initial design configuration:

The cross-section shown in Figure 4.1 is assumed to be the critical section for design, with the highest wall height. The wall was assumed to have a vertical inclination. An embedment depth of 0.6 m was selected for the 3:1 slope. The initial reinforcement length in the TDA was set to be 0.7H to start the analysis, and the vertical spacing was set to be one-half the height of the gabion height of 0.6 m. The gabions were assumed to have a square aspect ratio to start the analysis. A summary of the initial design configuration data is shown in Table 4.1. At this stage, an overbuild calculation was also performed for the initial vertical spacing, with results summarized in Tables 4.2.

Table 4.1: Initial Design Configuration Data for the Wall (Note that the reinforcement length and the gabion length are different than in Figure 4.1 as they were modified during design)

<u>General Data:</u>				
	TDA Height	H_{TDA}	3.0	m
	Granular Fill Height	H_G	1.2	m
	Total Fill Height	H	4.2	m
	Gabion Height	H_{GA}	0.6	m
	Embedment Depth	D	0.6	m
	Batter Angle	θ	0	degrees
	Vertical Spacing of Reinforcements	S_v	0.3	m
	Number of TDA Lifts	n_{TDA}	10	
	Number of Granular Lifts	n_G	4	
	Length of Gabion (equal to S_v to start)	L_{GA}	0.8	m
	Length of Reinforcements in TDA (0.7H to start)	L_{TDA}	5.5	m
	Total length of MSTDA wall	L	6.3	m
<u>Pavement Layer Properties:</u>				
	Hot mix asphalt layer thickness	H_{HMA}	0.10	m
	Hot mix asphalt unit weight	γ_{HMA}	22.0	kN/m ³
	Class 2 aggregate base thickness	H_{ab}	0.30	m
	Class 2 aggregate base unit weight	γ_{ab}	19.0	kN/m ³
	Permanent road section surcharge (dead load)	$q_{pavement}$	8.0	kPa/m
<u>Traffic Surcharge (Heavy trucks):</u>				
	Transient traffic surcharge (live load)	$q_{traffic}$	17	kPa/m
<u>TDA Fill Layer Properties:</u>				
	Reference friction angle	ϕ_0	30.2	degrees
	Change in friction angle	$\Delta\phi$	-14.4	degrees
	Reference pressure	P_{atm}	101.3	kPa
	Average secant friction angle	ϕ_{TDA}	36.8	degrees
	Apparent cohesion	c_{TDA}	0	kPa
	Initial dry unit weight	$\gamma_{d,TDA}$	5.0	kN/m ³
	Compaction water content	$w_{compaction}$	4.0	%
	Initial total unit weight	γ_{TDAi}	5.2	kN/m ³
	Final total unit weight after overbuild	γ_{TDA}	6.8	kN/m ³
<u>Granular Fill Layer Properties:</u>				
	Friction angle	ϕ_G	30.0	degrees
	Apparent cohesion	c_G	0	kPa
	Dry unit weight	$\gamma_{d,G}$	15.0	kN/m ³
	Compaction water content	$w_{compaction}$	5.0	%
	Total unit weight	γ_G	15.75	kN/m ³
<u>Gabion Fill Properties:</u>				
	Gabion fill friction angle	ϕ_{GA}	40.0	degrees
	Gabion fill unit weight	γ_{GA}	18.0	kN/m ³
<u>Foundation Soil (Unsaturated Dense Sand):</u>				
	Foundation soil friction angle	ϕ'_F	33	degrees
	Foundation soil apparent cohesion	c'_F	3	kPa
	Foundation soil unit weight	γ_F	17	kN/m ³
	Friction angle between TDA/nonwoven GT/Sand	$\phi_{TDA-Soil}$	31.3	

Table 4.2: Overbuild Calculations for the TDA Lifts

Material Properties				
TDA dry unit weight	5	kN/m ³	32	pcf
TDA gravimetric water content	4	%	4	%
TDA total unit weight	5.2	kN/m ³	33	pcf
G _s for TDA	1.15		1.15	
C _c for TDA	1.13		1.13	
C _r for TDA	0.1		0.1	
C _{ae} for TDA	0.0065			
Yield Stress for TDA	15		15	
t _{design}	3650	days		
φ ₀	30.2	degrees		
Δφ	-14.4	degrees		
P _{atm}	101.3	kPa		
Backfill dry unit weight	15.0	kN/m ³	110	pcf
Backfill gravimetric water content	5	%	10	%
Backfill total unit weight	15.75	kN/m ³	121	pcf
Target Geometry				
TDA Lift Thickness	0.3	m	1	ft
Reinforcement/Gabion Spacing	0.3	m	2	ft

TDA Overbuild Calculations without Surcharge (4 Sublayers)															
Layer	Granular Fill Thickness (m)	Depth from Surface (m)	Initial Elevation Top of Lift (m)	Initial Stress at Middle 1 (kPa)	Change in Stress at Middle 1 (kPa)	Final Stress at Middle 1 (kPa)	Initial Stress at Middle 2 (kPa)	Change in Stress at Middle 2 (kPa)	Final Stress at Middle 2 (kPa)	Initial Stress at Middle 3 (kPa)	Change in Stress at Middle 3 (kPa)	Final Stress at Middle 3 (kPa)	Initial Stress at Middle 4 (kPa)	Change in Stress at Middle 4 (kPa)	Final Stress at Middle 4 (kPa)
1	1.2	4.92	0.45	0.29	47.1	47.4	0.87	47.7	48.6	1.45	48.3	49.8	2.03	48.9	50.9
2		4.49	0.88	0.57	45.2	45.8	1.71	46.3	48.0	2.85	47.5	50.3	3.99	48.6	52.6
3		4.07	1.30	0.85	43.3	44.1	2.54	45.0	47.5	4.23	46.6	50.9	5.92	48.3	54.3
4		3.65	1.72	1.12	41.4	42.5	3.35	43.6	46.9	5.59	45.8	51.4	7.83	48.1	55.9
5		3.23	2.14	1.39	39.5	40.8	4.17	42.2	46.4	6.94	45.0	52.0	9.72	47.8	57.5
6		2.82	2.55	1.66	37.6	39.2	4.97	40.9	45.9	8.28	44.2	52.5	11.60	47.5	59.1
7		2.41	2.96	1.92	35.7	37.6	5.77	39.6	45.3	9.61	43.4	53.0	13.46	47.3	60.7
8		2.00	3.36	2.19	33.9	36.1	6.56	38.2	44.8	10.93	42.6	53.6	15.31	47.0	62.3
9		1.60	3.77	2.45	32.0	34.5	7.35	36.9	44.3	12.24	41.8	54.1	17.14	46.7	63.9
10		1.20	4.17	2.71	30.2	32.9	8.13	35.6	43.8	13.54	41.1	54.6	18.96	46.5	65.4

Layer	Initial Void Ratio	Settlement (m)	Change in Void ratio	Final Void Ratio	Final TDA Unit Weight (kN/m ³)	Percent Increase in Unit Weight	Final Lift Top Elevation (mm)	Target Elevation (m)	Cumulative Overbuild (m)	Individual Overbuild (m)	Depth from Top of TDA (m)	Depth from Surface (m)	Effective stress (kPa)	TDA Friction Angle (degrees)	K _{a,TDA}
1	1.3	0.147	-0.703	0.597	7.066	136	0.3	0.3	0.147	0.147	2.7	3.9	45.1	35.3	0.27
2	1.3	0.277	-0.674	0.626	6.936	133	0.6	0.6	0.277	0.130	2.4	3.6	43.0	35.6	0.26
3	1.3	0.401	-0.656	0.644	6.861	132	0.9	0.9	0.401	0.124	2.1	3.3	41.0	35.9	0.26
4	1.3	0.520	-0.642	0.658	6.806	131	1.2	1.2	0.520	0.119	1.8	3.0	38.9	36.2	0.26
5	1.3	0.636	-0.632	0.668	6.762	130	1.5	1.5	0.636	0.116	1.5	2.7	36.9	36.5	0.25
6	1.3	0.748	-0.622	0.678	6.724	129	1.8	1.8	0.748	0.112	1.2	2.4	34.9	36.9	0.25
7	1.3	0.858	-0.614	0.686	6.690	129	2.1	2.1	0.858	0.109	0.9	2.1	32.9	37.2	0.25
8	1.3	0.964	-0.606	0.694	6.659	128	2.4	2.4	0.964	0.106	0.6	1.8	30.9	37.6	0.24
9	1.3	1.067	-0.598	0.702	6.629	127	2.7	2.7	1.067	0.103	0.3	1.5	28.9	38.0	0.24
10	1.3	1.167	-0.591	0.709	6.601	127	3.0	3.0	1.167	0.100	0.0	1.2	26.9	38.5	0.23

Step 4: Characterize allowable tensile strength of reinforcements and resistance factors

The characteristics of the geogrid used in the MSTDA wall along with relevant reduction factors and pullout factors are summarized in Table 4.3. This table also includes the calculated allowable tensile strength.

Table 4.3: Geosynthetic Characteristics

Geosynthetic Properties				
Geosynthetic reinforcement type	GGB (PET Uniaxial Geogrid)			
Measured ultimate tensile strength	T_{ult}	71.6		kN/m
Reduction factor for installation damage	RF_D	1.1		
Reduction factor for creep	RF_{CR}	2.05		
Reduction factor for durability issues	RF_D	1.3		
Allowable tensile strength	T_{al}	24.4		kN/m
Pullout factor	F	0.55		
Geogrid effective unit perimeter	C	2		
Pullout scale correction factor	α	0.8		

Step 5: Define nominal loads, load combinations, and load factors

The load factors and the calculation of horizontal and vertical forces for static loading are summarized in Table 4.4. The geometry of the schematic in this table is not representative of the geometry of the wall in Figure 4.1, but shows the general definition of the forces.

Table 4.4: Load Factors and Definition of Key Forces

Load Factor Summary:						
Limit State	EH	ES	EV	LL	EQ	
Strength Limit State	0.9 to 1.5	0.75 to 1.5	1.0 to 1.35	1.75	-	
Extreme Event (Seismic) Limit State	0.9 to 1.5	0.75 to 1.5	1.0 to 1.35	G_{EQ}	1	
Global Stability	-	1	1	-	-	
Service Limit State	1	1	1	-	-	

Calculation of Forces	<p>Surcharge for bearing resistance and global stability analysis</p> <p>Surcharge for limiting eccentricity and sliding resistance analyses</p> <p>Granular fill layer (ϕ_{Gf}, γ_{Gf}, K_{aG})</p> <p>Gabion fill (ϕ_{Gf}, γ_{Gf})</p> <p>Dimensions: H, H_G, H_{TDA}, L_G, L, B, C_L</p> <p>Formulas for forces:</p> <ul style="list-style-type: none"> $V_1 = \gamma_{Gf} H_{TDA} L$ $V_2 = \gamma_{Gf} H_G L$ $V_3 = \gamma_{Gf} H_G L$ $F_1 = \frac{1}{2} \gamma_{TDA} H_{TDA}^2 K_{aTDA}$ $F_2 = \frac{1}{2} \gamma_{Gf} H_G^2 K_{aG}$ $F_3 = q H_{TDA} K_{aTDA}$ $F_4 = q H_G K_{aG}$ <p>Vertical force levels: $H_{TDA}/3$, $H_{TDA}/2$, $H_{TDA} + H_G/2$, $H_{TDA} + H_G/3$</p>					
Average active earth pressure coefficient for TDA	$K_{a,TDA}$	0.25	(NOTE: Equation for Vertical Wall)			
Active earth pressure coefficient for granular fill	$K_{a,G}$	0.33				
Vertical force 1	V_1	128.0		kN/m		
Vertical force 2	V_2	119.1		kN/m		
Vertical force 3	V_3	60.5		kN/m		
Horizontal force 1	F_1	7.7		kN/m		
Horizontal force 2	F_2	3.8		kN/m		
Horizontal force 3	F_3	18.9		kN/m		
Horizontal force 4	F_4	10.0		kN/m		

Step 6: Evaluation of external stability

Next, the external stability of the wall is analyzed. The results of the analyses and the relevant checks are summarized below. The wall had sufficient external stability for the initial geometric configuration of the wall. However, the results below are for the length of the reinforcements and the length of the gabions shown in Table 4.1. These values were increased from the initial values later in the analysis to have sufficient seismic stability. However, the summary of the calculations below show how the different external stability checks are performed.

<i>Sliding:</i>				
	Resistance factor for sliding	Φ	1.0	
	Load factor for vertical loads in resistance	Γ_{EV}	1.0	
	Factored resistance against sliding failure	R_f	187	kN/m
	Load factor for horizontal dead loads	Γ_{EH}	1.5	
	Load factor for horizontal live loads	Γ_{LS}	1.75	
	Factored load contributing to sliding failure	F_f	68	kN/m
	Check on sliding	$R_f > F_f ?$	OK	
<i>Limiting Eccentricity:</i>				
	Maximum eccentricity for soil subgrade	$e_{c,max}$	1.6	m
	Maximum eccentricity for rock subgrade	$e_{c,max}$	2.4	m
	Load factors for horizontal dead loads	Γ_{EH}	1.5	
	Load factors for horizontal live loads	Γ_{LS}	1.75	
	Load factors for vertical loads	Γ_{EV}	1.0	
	Sum of factored driving moments	ΣM_D	143	kN/m-m
	Sum of factored resisting moments	ΣM_R	901	kN/m-m
	Sum of factored vertical forces	ΣV	308	kN/m
	Factored eccentricity (neglect resisting moments)	e_c	0.47	m
	Check on eccentricity	$e_c < e_{c,max} ?$	OK	

<i>Bearing Capacity:</i>				
	Load factors for horizontal dead loads	Γ_{EH}	1.5	
	Load factors for horizontal live loads	Γ_{LS}	1.75	
	Load factors for vertical loads	Γ_{EV}	1.35	
	Sum of factored driving moments for bearing	ΣM_D	143	kN/m-m
	Sum of factored resisting moments	ΣM_R	1217	
	Sum of factored vertical forces for bearing	ΣV	656	
	Eccentricity for bearing capacity (neglect resisting)	e_B	0.22	m
	Uniform bearing stress per unit width	$\sigma_{v,bearing}$	112	kPa/m
	Bearing capacity factor	N_c	38.64	
	Bearing capacity factor	N_q	26.09	
	Bearing capacity factor	N_γ	24.44	
	Surcharge due to embedment (neglected)	q_D	9.00	kPa/m
	Ultimate bearing capacity	$q_{ult,drained}$	324	kPa/m
	Resistance factor for bearing capacity	Φ	0.65	
	Factored ultimate bearing capacity	$q_{ult,drained} \cdot f$	210	
	Check on bearing capacity	$q_{ult,drained} \cdot f > \sigma_{v,bearing} ?$	OK	

Step 7: Evaluate internal stability for MSTDA wall with geosynthetic reinforcements

The details of the internal stability checks for the MSTDA wall are summarized below. Similar to the external stability checks for static loading, the wall had sufficient internal stability for the initial configuration. The most critical issue in the internal stability analysis was the frictional connection strength in the gabions. Only every other geosynthetic is connected to the gabion facing. Nonetheless, the intermediate reinforcements are still stable. The results below account for the longer reinforcement length and gabion length selected to have sufficient seismic stability but they exemplify the steps necessary to assess the internal stability.

<i>Rupture:</i>									
	Load factor for horizontal stresses	Γ_{EV}	1.350						
	Reinforcement layer number	Depth of reinforcement (m)	Vertical Stress (kPa)	Factored Horizontal Stress (kPa/m)	Tensile stress (kN/m)	L_e (m)	Vertical Stress in Gabions (kPa)	$T_{connection,f}$ (kN/m)	$T_{ult,connection}$ (kN/m)
	Granular Fill 1	0.3	29.8	13.4	4.0	3.25	5.4		
	Granular Fill 2	0.6	34.5	15.5	4.7	3.42	10.8	11.3	13.1
	Granular Fill 3	0.9	39.2	17.6	5.3	3.59	16.2		
	Granular Fill 4	1.2	43.9	19.8	5.9	3.77	21.6	22.6	26.3
	TDA 1	1.5	45.9	15.6	4.7	4.15	27		
	TDA 2	1.8	47.9	16.2	4.9	4.30	32.4	33.9	39.4
	TDA 3	2.1	49.9	16.9	5.1	4.45	37.8		
	TDA 4	2.4	51.9	17.6	5.3	4.60	43.2	45.2	52.5
	TDA 5	2.7	53.9	18.3	5.5	4.75	48.6		
	TDA 6	3	55.9	19.0	5.7	4.90	54	56.5	65.7
	TDA 7	3.3	58.0	19.7	5.9	5.05	59.4		
	TDA 8	3.6	60.0	20.3	6.1	5.20	64.8	67.8	78.8
	TDA 9	3.9	62.1	21.1	6.3	5.35	70.2		
	Base of Wall - no Reinforcement	4.2	64.2	21.8					
	Maximum tensile stress in geosynthetic	T_{max}	6.3	kN/m					
	Resistance factor	Φ	0.9						
	Factored allowable tensile resistance	$T_{all,f}$	22.0	kN/m					
	Check on rupture	$T_{all,f} > T_{max}$?	OK						
<i>Pullout:</i>									
	Resistance factor for pullout	Φ	0.9						
	Minimum embedment in TDA layer	L_e	4.15	m					
	Factored embedment	ΦL_e	3.73	m					
	Vertical stress at the depth of minimum embedment	σ_v	46	kPa					
	Required embedment	$T_{max}/F\alpha\sigma_v C$	0.16	m					
	Check on pullout	$\Phi L_e > T_{max}/F\alpha\sigma_v C$?	OK						
<i>Connection strength:</i>									
	Resistance factor for connection strength	Φ	0.9						
	Interface friction angle between gabion and geogrid	$\phi_{GA-geosynthetic}$	36	degrees					
	Check on connection strength at wall crest	$T_{connection,f} > T_{max}$?	OK						

Step 8: Service limit state checks on TDA deformations

This step is required in the case that the geosynthetic spacing needs to be refined. However, the initial spacing was satisfactory, so the results in Table 4.2 were the final set of overbuild calculations.

Step 9: Global and compound stability (at service limit state)

As the wall considered in this report is hypothetical, a global stability analysis was not performed. However, the goals of a global stability analysis performed with a commercial slope stability software are summarized below.

C. Global Stability			
Resistance factor for shear strength on failure plane:	Φ	0.75	
All load factors	Γ	1	
Corresponding required factor of safety	$FS_{required}$	1.3	
<i>Use a slope stability analysis to perform stability analysis with final unit weights and geometry, ensure $FS > FS_{required}$</i>			

Step 10: Check effects of seismic events (and other extreme events)

The critical design process for the MSTDA wall was the seismic stability analysis. A location near Santa Barbara, CA was selected for this example, and the results of the seismic characteristics are summarized in Table 4.5. These parameters were primarily obtained from the Figures and Tables in Chapter 3.10 of AASHTO (2020).

Table 4.5: Seismic Characteristics of the Hypothetical MSTDA Wall Location

<i>Assume a site location near Santa Barbara, CA</i>			
Peak Ground Acceleration with 1000 year return	PGA	0.40	g
Spectral acceleration at 1 second with 1000 year return	S_1	0.34	g
Assume a site class with stiff soil	Site Class	D	
Site factor	F_{PGA}	1.1	
Site factor	F_v	1.6	
Wall height reduction factor	α_H	0.98	
Maximum horizontal acceleration	k_{av}	0.43	
Peak ground velocity	PGV	21	m/s
Average unit weight of backfill	$\gamma_{b,ave}$	9.34	kN/m ³
Average friction angle of the backfill	$\phi_{b,ave}$	34.8	
Horizontal seismic coefficient	k_h	0.43	
Vertical seismic coefficient	k_v	0.0	
Horizontal-Vertical Acceleration Angle	ξ	23.4	degrees
Average M-O earthquake horizontal coefficient	K_{AE}	0.78	
Total thrust due to static and dynamic loading	P_{AE}	64	kN/m
Weight of Backfill and Gabion	W	308	
Horizontal inertial force	P_{IR}	67	kN/m
Earthquake Loading Factor	Γ_{EQ}	1	
Total horizontal force	$T_{H,EQ}$	202	kN/m

Next, checks were performed on the seismic external stability and the seismic internal stability. The seismic sliding resistance required that the length of the reinforcements be increased from 0.7H (equal to 2.94 m) to 5.5 m. As a spreadsheet approach was used for the design, the previous analyses were updated with the new length and the checks were all performed again.

<i>Seismic Sliding:</i>				
	Resistance factor for earthquake sliding	Φ	1	
	Resistance to earthquake sliding	$R_{f,EQ}$	209	kN/m
	Check on earthquake sliding	$R_f > F_f ?$	OK	

<i>Seismic Limiting Eccentricity:</i>				
	Maximum eccentricity for soil subgrade	$e_{c,max}$	1.6	
	Maximum eccentricity for rock subgrade	$e_{c,max}$	2.4	
	Load factors for horizontal dead loads	Γ_{EQ}	1.0	
	Load factors for horizontal live loads	Γ_{EQ}	1.0	
	Load factors for vertical loads	Γ_{EQ}	1.0	
	Sum of factored driving moments	ΣM_D	424	
	Sum of factored vertical forces	ΣV	344	
	Factored eccentricity (neglect resisting moments)	e_c	1.23	
	Check on eccentricity	$e_c < e_{c,max} ?$	OK	
<i>Seismic Bearing Capacity:</i>				
	Load factors for horizontal dead loads	Γ_{EQ}	1.0	
	Load factors for horizontal live loads	Γ_{EQ}	1.00	
	Load factors for vertical loads	Γ_{EQ}	1.00	
	Sum of factored driving moments for bearing	ΣM_D	424	kN/m-m
	Sum of factored vertical forces for bearing	ΣV	482	kN/m
	Eccentricity for bearing capacity (neglect resisting)	e_B	0.88	m
	Uniform bearing stress per unit width	$\sigma_{v,bearing}$	106	kPa/m
	Bearing capacity factor	N_c	38.64	
	Bearing capacity factor	N_q	26.09	
	Bearing capacity factor	N_γ	24.44	
	Surcharge due to embedment (neglected)	q_D	14.18	kPa/m
	Ultimate bearing capacity	$q_{ult,drained}$	324	kPa/m
	Resistance factor for bearing capacity	Φ	1.00	
	Factored ultimate bearing capacity	$q_{ult,drained} \cdot f$	324	kPa/m
	Check on bearing capacity	$q_{ult,drained} \cdot f > \sigma_{v,bearing} ?$	OK	

Finally, the seismic internal stability was assessed. While the geosynthetic had sufficient ultimate tensile strength and pullout strength to resist the increased seismic loading, the connection strength was an issue. Accordingly, the length of the gabion was increased from 0.6 to 0.8 m. Again, all the previous design checks were evaluated with this new variable.

<i>Seismic Rupture:</i>				
	Weight of fill in active wedge	W_a	66	kN/m
	Inertial load	P_i	55	kN/m
	Number of reinforcements	n	13	
	Inertial force in reinforcements	$T_{d,f}$	4.2	kN/m
	Total tensile load in reinforcements	T_{total}	10.5	kN/m
	Resistance factor for dynamic loading	Φ	1.2	
	Factored total load in reinforcements	$T_{total,f}$	20	
	Check on rupture	$T_{ult} > T_{total,f} ?$	OK	
<i>Seismic Pullout:</i>				
	Minimum embedment length in TDA	$L_{e,min}$	4.15	m
	Vertical stress in TDA at depth of minimum embedment	σ_v	26	kPa
	Dynamic resistance factor	Φ	1.20	
	Required seismic embedment	$T_{total}/0.8\Phi F\alpha\sigma_v C$	0.48	m
	Check on pullout	$L_e > T_{total}/0.8\Phi F\alpha\sigma_v C ?$	OK	
<i>Seismic Connection:</i>				
	Resistance factor for connection strength	Φ	1.2	
	Interface friction angle between gabion and geogrid	$\phi_{GA-geosynthetic}$	36	degrees
	Required seismic connection strength	$T_{connection,dyn}$	8.7	kN/m
	Check on connection strength at wall crest	$T_{ult,connection} > T_{connection,dyn} ?$	OK	

Step 11: Design wall drainage system

A detailed drainage analysis was not performed, but the typical details for the drainage system are shown in the final layout of the wall in Figure 4.2. This modified design shows the longer reinforcement length and gabion length compared to the initial design configuration.

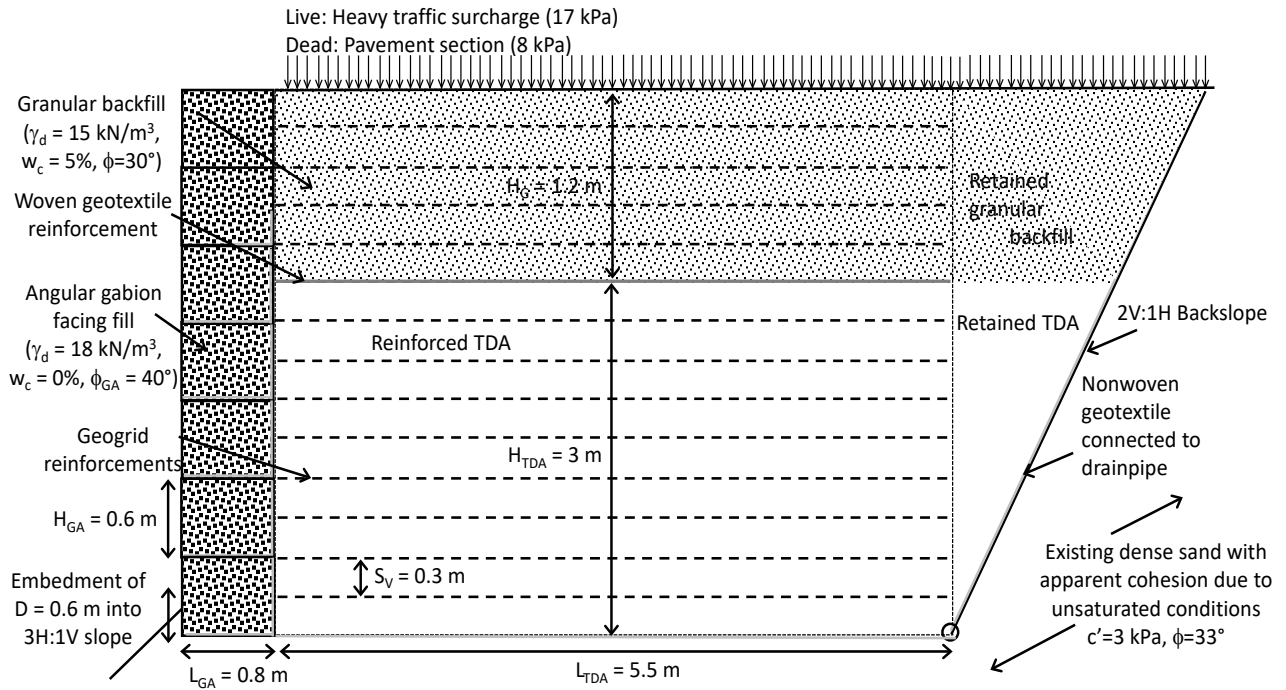


Figure 4.2: Final MSTDA Wall Configuration Accounting for all Design Checks

This page is intentionally left blank

Chapter 5: Case Histories of MSTDA Retaining Walls in California

Three case histories are presented in this chapter. The MSTDA walls were constructed prior to the development of this report, so they do not necessarily follow the design process or recommendations listed above. However, they provide useful insight into the motivation to use MSTDA walls, design decisions, and construction details.

Case 1: Ortega Ridge Road (Santa Barbara County, CA)

The project site is located south of Highway 192 and north of State Route 1 on Ortega Ridge Road in Santa Barbara County as shown on Figure 5.1. Approximately 60 m (200 ft) of an embankment constructed in the 1950's on Ortega Ridge Road had been undergoing creep settlement over many years, as evidenced by chronic settlement of the road surface. The road had been overlaid several times to keep the road surface relatively flat and safe, which added to the weight on the embankment and exacerbated the creep. The geotechnical site investigation was performed in February 2016, and project construction occurred in June 2019. The remediation project involved removing some roadway fill and replacing it with an MSTDA wall.

Plan-view drawings showing the area of soil removed during construction and replaced with a MSTDA wall are shown in Figures 5.2 and 5.3, respectively. A general cross-sectional schematic of the MSTDA wall is shown in Figure 5.4, highlighting the crushed rock-filled gabion facing, the TDA layer with different heights up to 3 m (10 ft), the use of geosynthetic reinforcement in both the TDA and the overlying 1 m-thick granular backfill layer, and the paved road on the surface. The gabions used in the project have a height of 0.457 m (18 inches), which corresponded to the reinforcement spacing. A detailed view highlighting the reinforcement locations is shown in Figure 5.5. The detailed schematic in Figure 5.5 indicates that the bottom two TDA lifts were embedded below the ground surface by a depth of 1 m (3ft) and that no bearing pad was included below the facing. A drainage pipe was included in a granular layer below the TDA. The gabion construction detail in Figure 5.6 shows that each gabion was shifted inward by 0.15 m (6 inches) from the lower gabion (batter angle of 72 degrees), and also shows how the separation geotextile is placed between the TDA and crushed rock within the gabions. The height of the wall varied along the length of the road, as shown in Figure 5.7. The maximum exposed height of the wall is approximately 12 feet with a 3 m-thick (10 ft-thick) layer of TDA behind the wall facing.

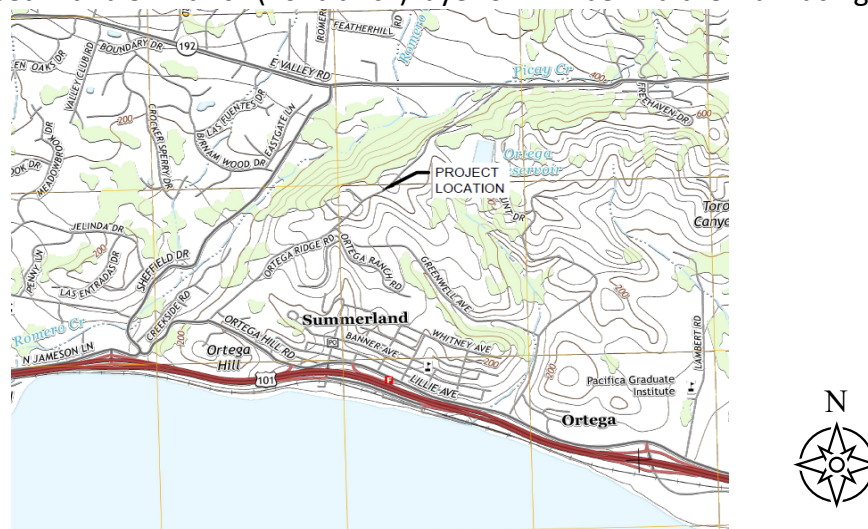


Figure 5.1: Map of the Project Location

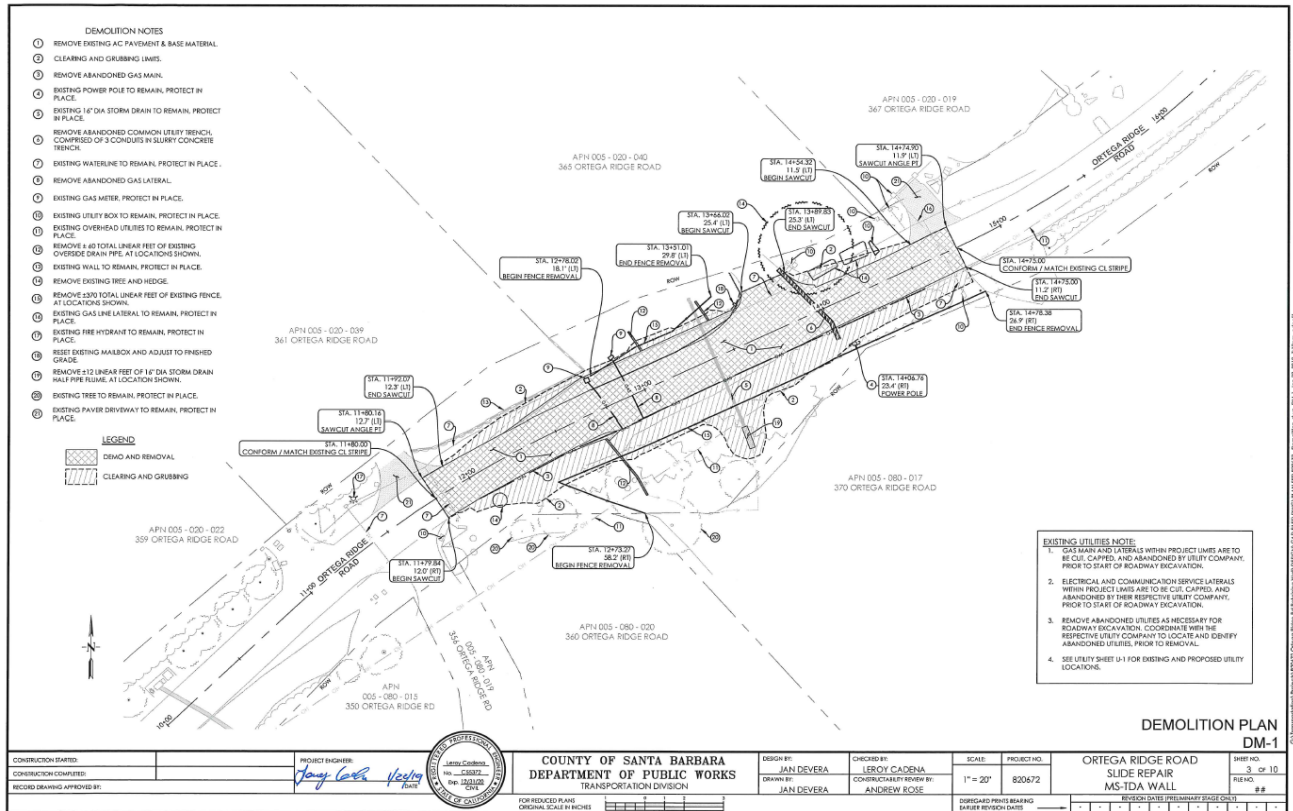


Figure 5.2: Drawing Shown in the Area of Existing Soil Removed

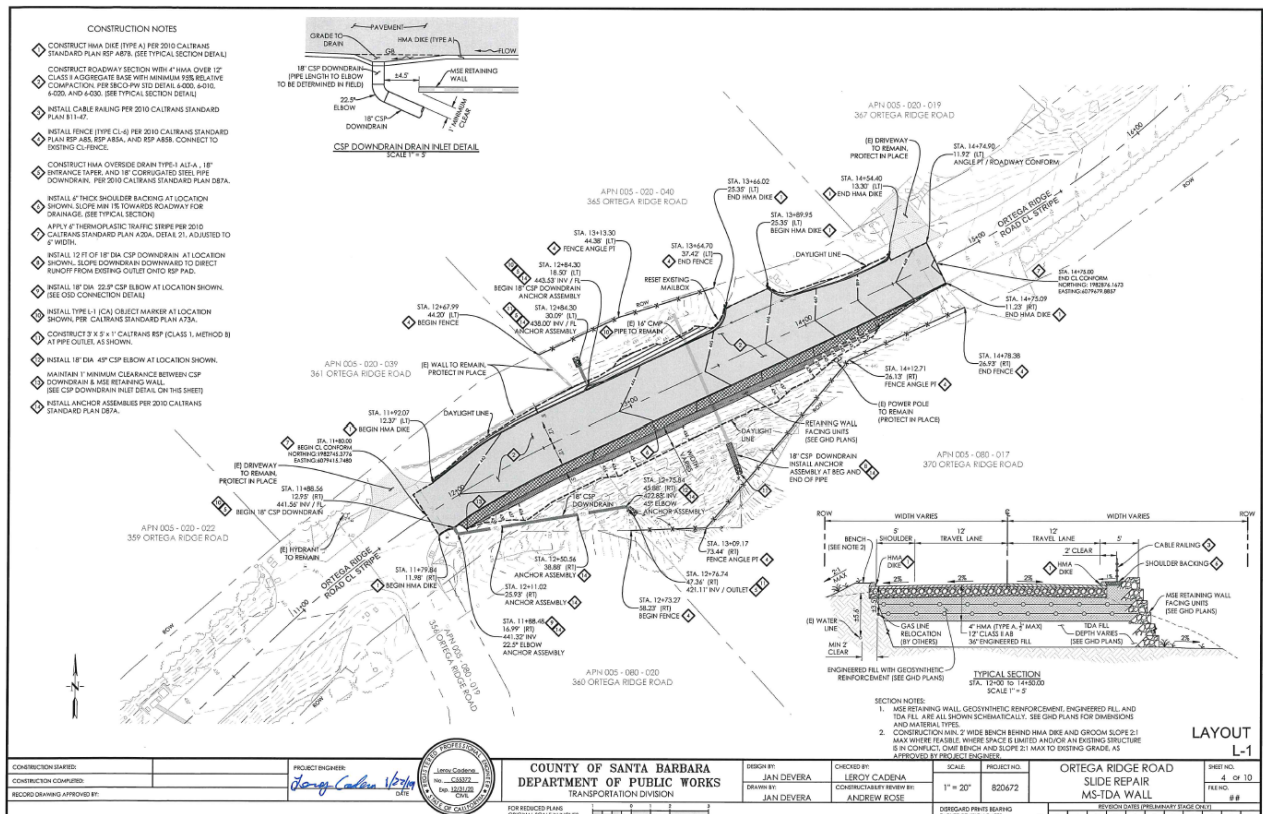


Figure 5.3: Drawing Showing the Area Replaced with an MSTDA Wall

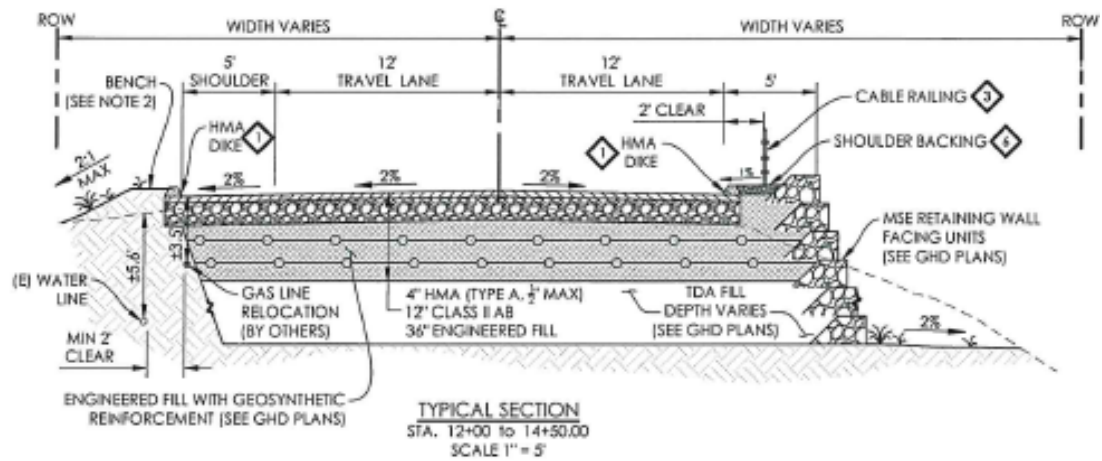


Figure 5.4: General Drawing of the MSTDA Wall

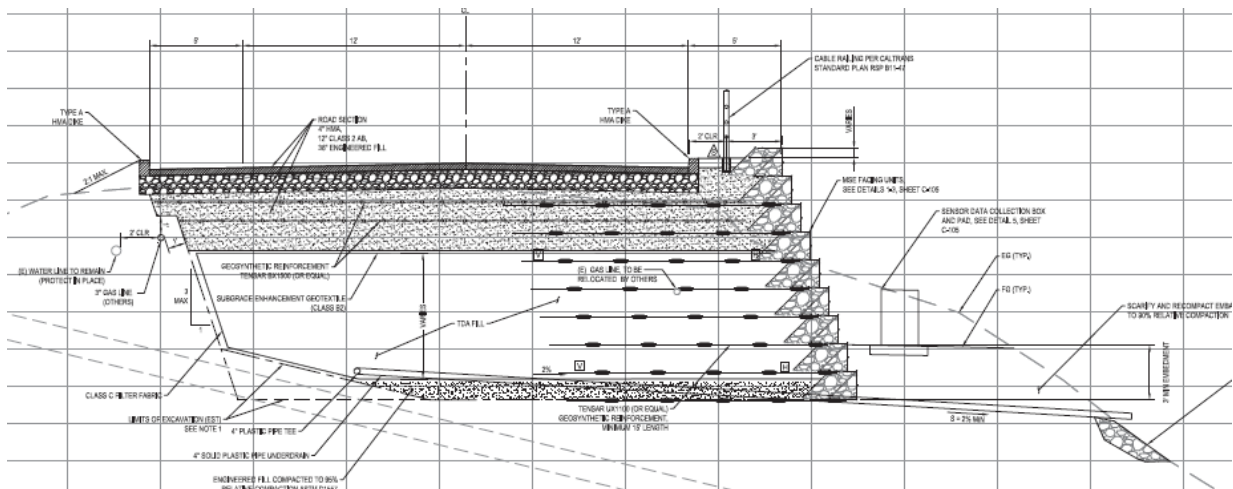


Figure 5.5: Detailed Drawing of the MSTDA Wall

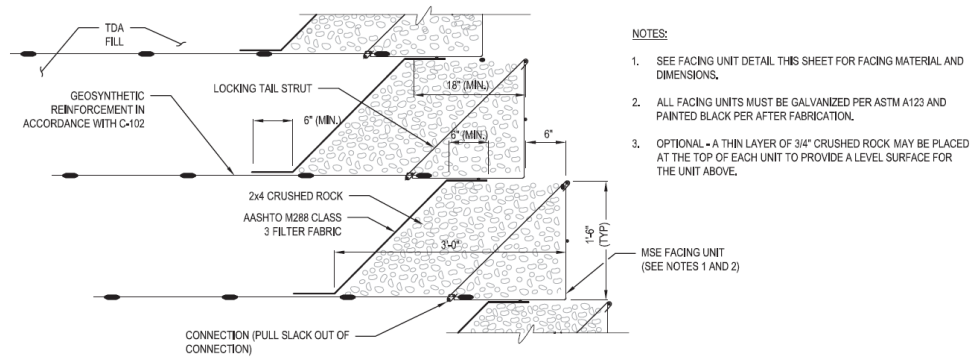


Figure 5.6: Gabion Facing Connection Detail

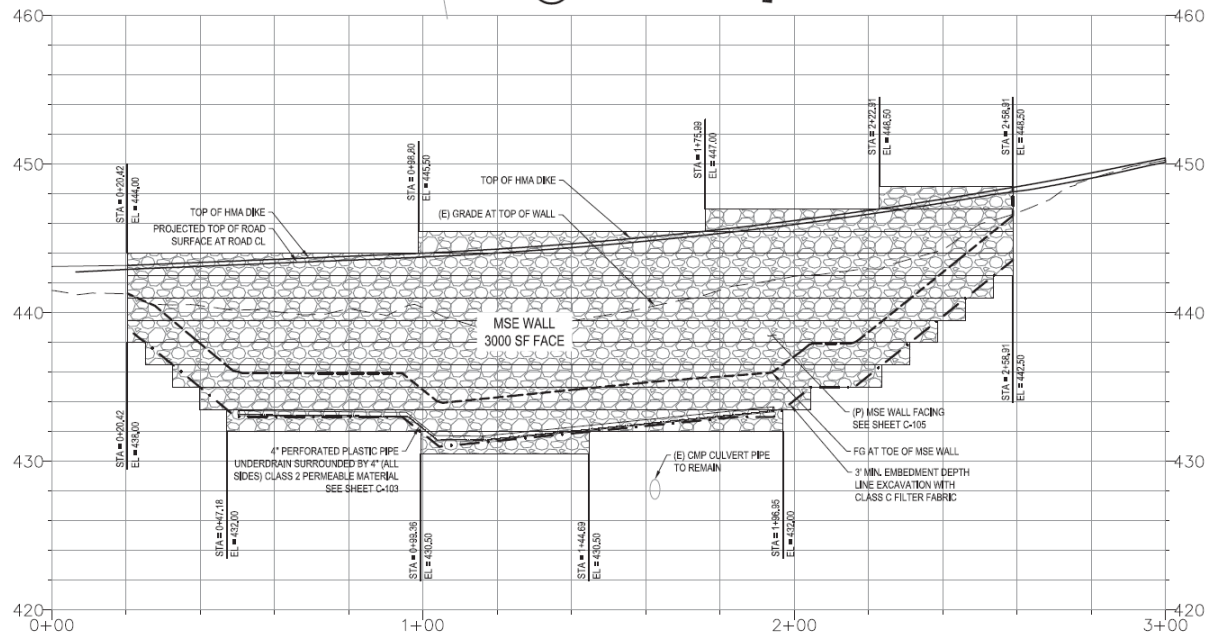


Figure 5.7: Elevation View of the Wall Height Along the Length of the Road

As part of the design, static and pseudo-static global stability analyses were performed to consider the overall stability of the embankment considering the MSTDA wall as well as an internal stability analysis to check the reinforcement length and spacing. The material parameters used in both analyses are summarized in Table 5.1. A linear failure envelope with a friction angle was used for TDA with an average friction angle of 35°, which is consistent with the range of secant friction angles mentioned in Chapter 2 for Type B TDA. The results from the global stability analyses are shown in Figures 5.8 and 5.9.

Table 5.1: Material Parameters Used in the Stability Analysis

Material	ϕ' (deg)	c' (psf)	γ_t (pcf)
Sandy Clay (historical fill)	5	1,000	110
Native Clay (historical fill)	5	550	110
Sandy Silt (native)	36	500	125
TDA	35	0	45
Engineered Fill (above TDA)	34	0	125
Pavement Section	36	0	140
Uniaxial Geogrid (Tensar UX1100): Pullout = 1,000 psf; Tensile = 742 lbs			

Table 5.2: Global Stability Results for the MSTDA Wall and Surrounding Embankment

Analysis Condition	Factors of Safety		Acceptable
	Result	Criteria	
Long-term Static	1.6	1.4	yes
Pseudo-Static	1.1	1.1	yes

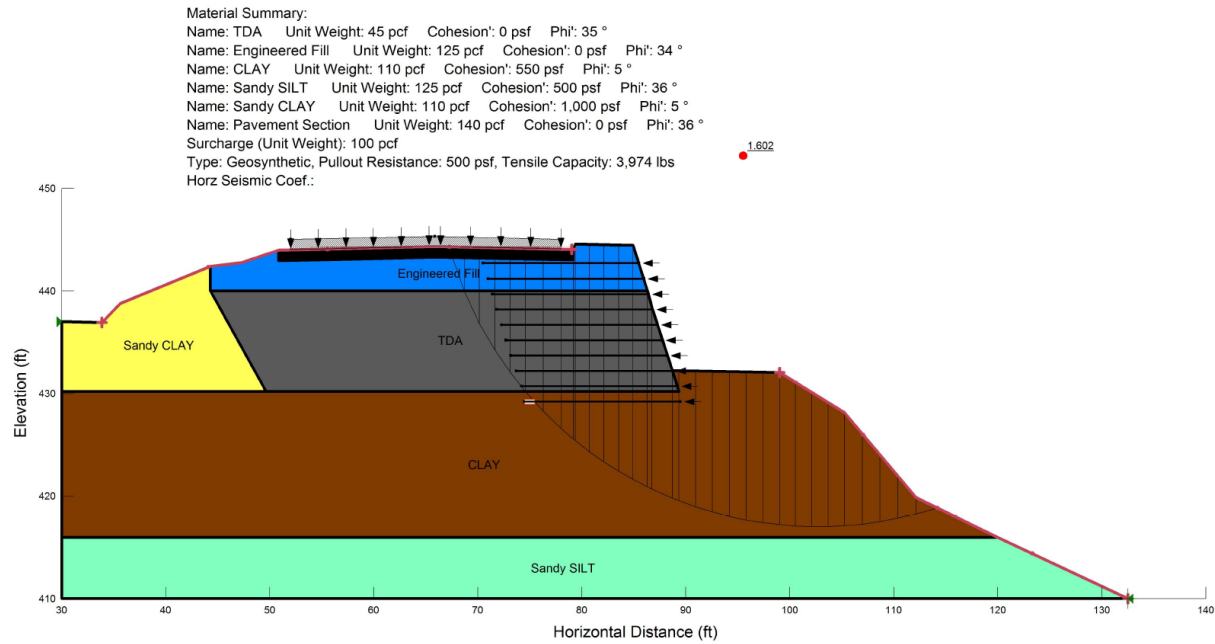


Figure 5.8: Global Stability Analysis Results for Static Conditions Showing the Most Critical Global Failure Surface

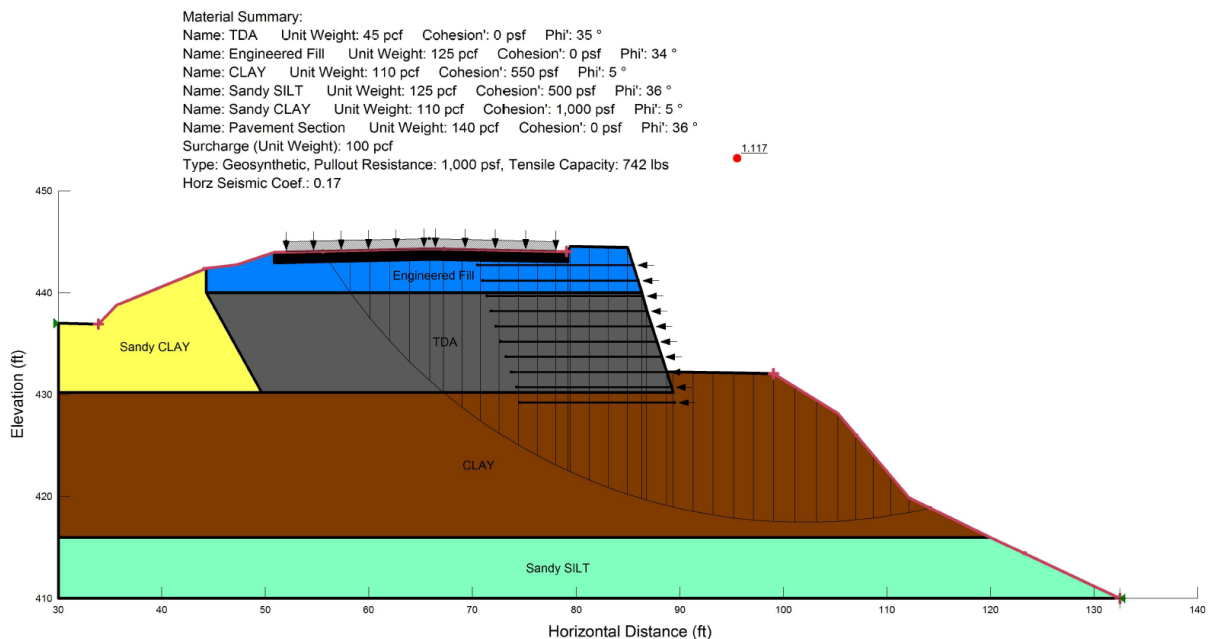


Figure 5.9: Global Stability Analysis Results for Pseudo-Static Conditions Showing the Most Critical Global Failure Surface

An MSE wall design software developed by Tensar was used to perform the internal stability analysis, shown in Figures 5.10 and 5.11. This analysis found that a reinforcement length of 15 ft was used for the wall height of 15 ft. The results of the external stability analysis in Figure 5.11 are not as accurate as the analyses in Figures 5.8 and 5.9, but this figure summarizes the checks that were performed and the minimum factors of safety for each check.

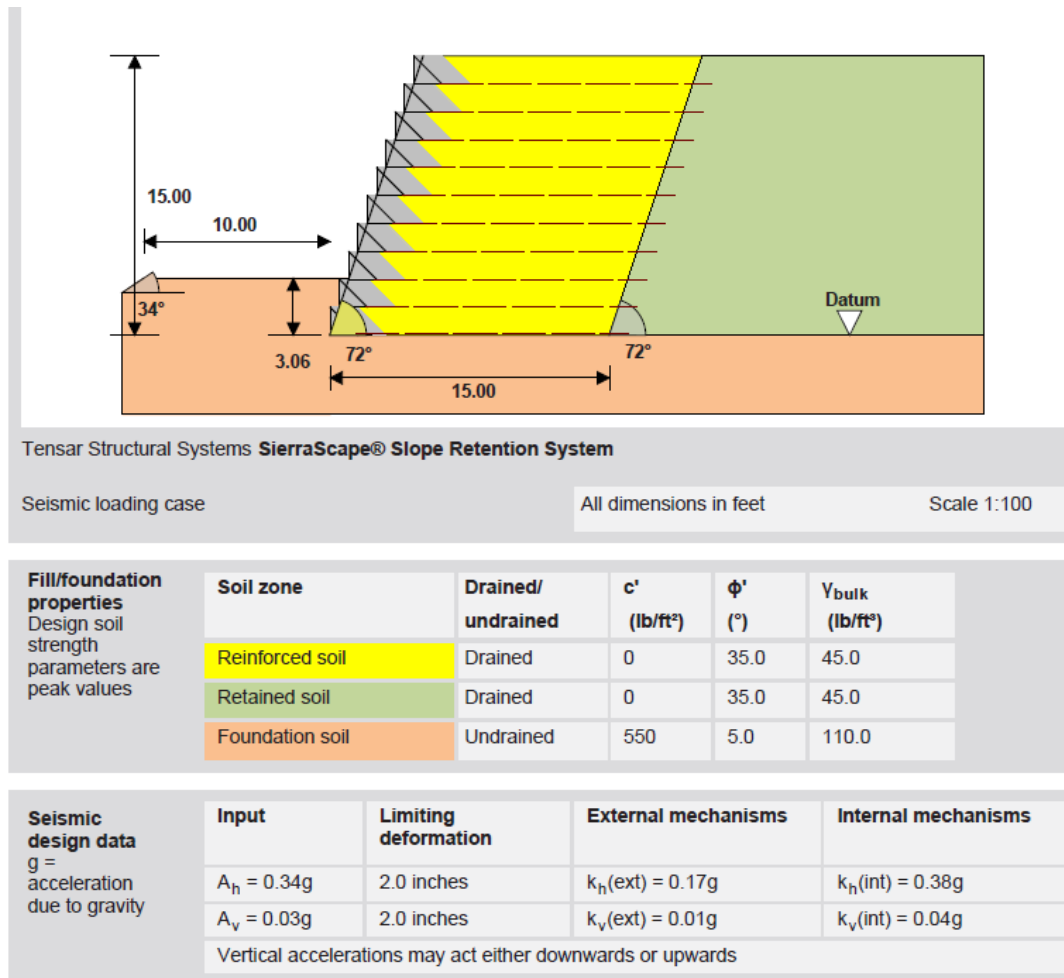


Figure 5.10: Overview of Internal Stability Analysis for the Ortega Ridge MSTDA Wall

Water pressure data	Location	Height of water level above datum (m)		r_u	
	In front of structure	No water pressures			
	Within fill	No water pressures		NA	

Verification of external stability	Mechanism	Result	Max/Min	Critical case	OK?
	Overturning	FS = 8.57	1.5 min	Seismic	OK
	Sliding on base	FS = 3.16	1.13 min	Seismic	OK
	Bearing capacity	FS = 5.794	2.5 min	Static	OK

Verification of internal stability	Mechanism	OK?	Mechanism	OK?
	Rupture check	OK	Pullout check	OK
	Internal sliding	OK	Connection check	OK

Reinforcement layout Starting and finishing levels are related to datum	Tensar Geogrid	No of layers	Starting level (ft)	Vertical spacing (ft)	Finishing level (ft)	Coverage C_i (%)	
	UX1100MSE	9	1.50	1.50	13.50	94	0.8
	UX1100MSE	1	0.00	-	-	94	0.8

Required minimum factors of safety As given in Table 5.1 for static and Table 6.1 for seismic.	Mechanism	Static loading	Seismic loading
	Overturning	FS = 2.0	FS = 1.5
	Sliding on base	FS = 1.5	FS = 1.1
	Bearing capacity	FS = 2.0	FS = 1.5
	Geogrid rupture	FS = 1.5	FS = 1.1
	Geogrid pullout	FS = 1.5	FS = 1.1
	Connection with facing (ultimate)	FS = 1.5	FS = 1.1
	Connection with facing (serviceability)	FS = 1.0	NA
	Internal sliding on geogrid	FS = 1.5	FS = 1.1

Figure 5.11: Results of Internal Stability Analysis for the Ortega Ridge MSTDA Wall

Pictures of the construction process of the MSTDA wall at Ortega Ridge road are shown in Figures 5.12 through 5.27. These photos show the sequence of construction from the initial excavation (Figures 5.12 and 5.13), TDA placement, compaction, and interfaces with the reinforcing geogrids and gabions (Figures 5.14 through 5.25) and the final MSTDA wall (Figures 5.26 and 5.27). The captions in each photo describe the construction process.



Figure 5.12: Failed Roadway Embankment on Ortega Ridge Road Prior to Remediation



Figure 5.13: Initial Excavation of the Failed Embankment



Figure 5.14: Excavation of the Failed Embankment Material



Figure 5.15: Placement of TDA Within the Excavation



Figure 5.16: Placement of the First Above-Ground Gabion And Preparation of the Reinforcement layer to be stretched across the TDA



Figure 5.17: Placement of the Second Above-Ground TDA Lift



Figure 5.18: Picture Showing the Geosynthetic Wrapped Around the Facing while a TDA Lift Is Being Placed By an excavator



Figure 5.19: Photo Showing the Compaction of the TDA Using a Vibratory Sheepfoot Roller



Figure 5.20: Picture of the Third Above-Ground TDA Lift Being Placed



Figure 5.21: Placement of Crushed Rock into the Next Gabion Layer



Figure 5.22: Picture of the Separator Geotextile Being Placed Between the Crushed Rock and TDA



Figure 5.23: Preparation for Geogrid Placement at the Top of a TDA Lift



Figure 5.24: Picture of a Utility Line Running through the TDA Along with a Highlight of the Separator Geotextile Between the Crushed Rock and TDA, and the Biaxial Geogrid Placed Within the Gabions for Improved Retention of Rock Within the Gabions



Figure 5.25: Placement of the Fourth Above-Ground TDA Lift and Checks on the Batter of the Gabion Wall Facing



Figure 5.26: Final MSTDA Wall at Ortega Ridge Road from the North



Figure 5.27: Final MSTDA Wall at Ortega Ridge Road from the South

Case 2: Italian Bar Road, Site 3 (Tuolumne County, CA)

Five sites along Italian Bar road in Tuolumne County, north of Sonora, CA were damaged due to heavy rainfall and erosion during 2018, as shown in Figure 5.28. The sites were all unpaved roads that ran along a steep hill and involved replacement of the roadway embankment with an MSTDA wall which helped to widen the downslope lane of the road. The design and construction of the walls occurred in 2019. The five sites had relatively similar details, so this section focuses on Site 3, which had the tallest MSTDA wall. Different from the MSTDA wall at Ortega Ridge, this site was constructed using facing elements with combined metallic reinforcements following a proprietary design by Hilfiker, with a general schematic shown in Figure 5.29. Although Figure 5.29 shows a battered wall, the actual facing elements selected had an inclined face, which led to a wall with a smooth-battered facing rather than a stepped-battered facing. The toe of the MSTDA wall was embedded similar to the MSTDA wall at Ortega Ridge. During excavation of the slope, many boulders were encountered, which were then placed on the downslope side of the wall. A plan view showing the extent of the MSTDA wall construction is shown in Figure 5.30.

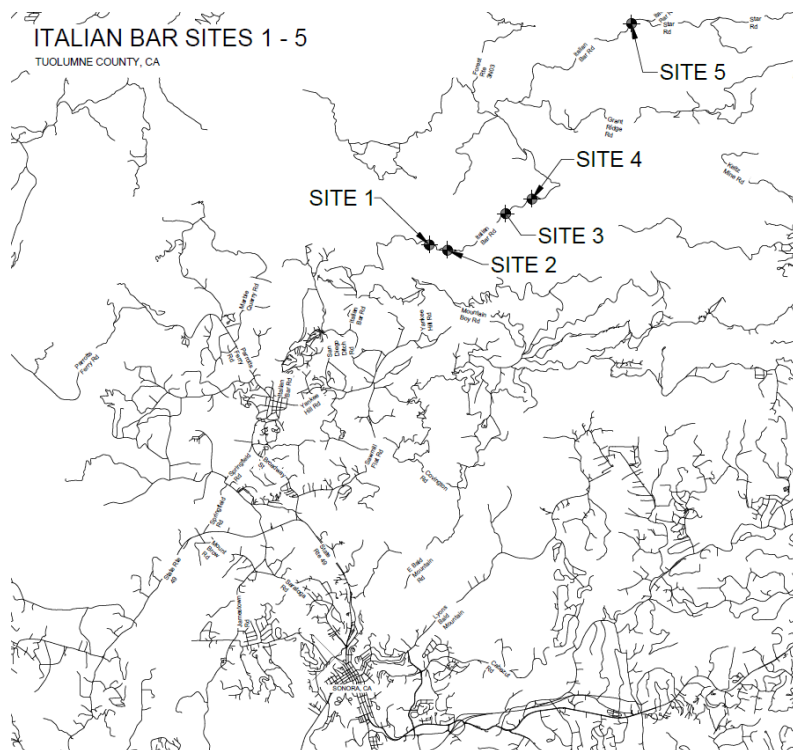
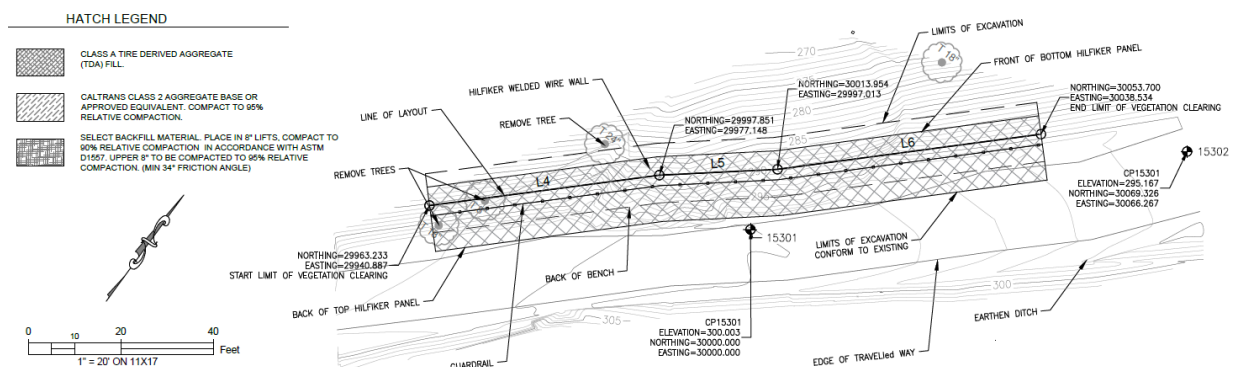
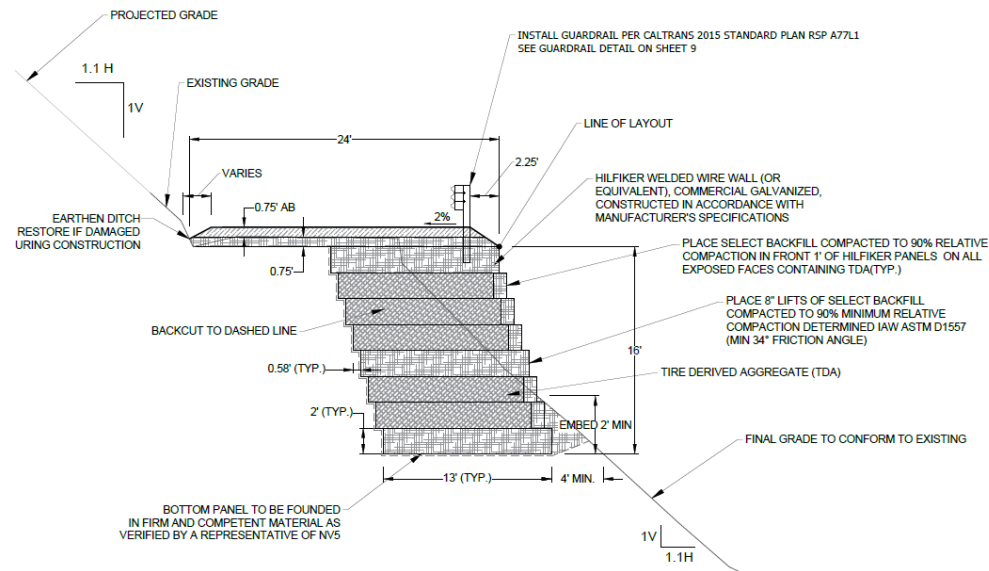


Figure 5.28: Location of Italian Bar Road Site 3 in Tuolumne County, CA



A picture of the stability analysis performed on the MSTDA wall in GEO5 is shown in Figure 5.31. The designers assumed that the TDA was similar to typical reinforced soil with a friction angle of 34 degrees, and a high unit weight of 105 pcf was used in the calculation. Both of these numbers were selected based on the designers' experience with Hilfiker welded wire walls. On the surface, the designers assumed a 350 psf traffic surcharge load and a 0.2g horizontal seismic load. They started the surcharge 1.5 ft from the wall face in all cases due to the presence of a guardrail. The wall had a maximum height of 16 ft, even though at least the bottom 2 ft were embedded, and the designers selected welded wire fabric (WWF) mats having a length of 13 ft. A picture of the global slope stability analysis for the wall is shown in Figure 5.32. The slip surfaces considered all had factors of safety greater than 3.0. Results of additional internal and external stability calculations for the MSTDA wall are shown in Figure 5.33. As a standard Hilfiker welded wire wall design was used at the site, the detailed construction specifications for the wall are shown in Figure 5.34 and 5.35. No special considerations were used for the TDA beyond encasing each TDA layer in geotextile, placing crushed rock within the gabions, and placing the granular bearing soil layer for the roadway atop the MSTDA wall.

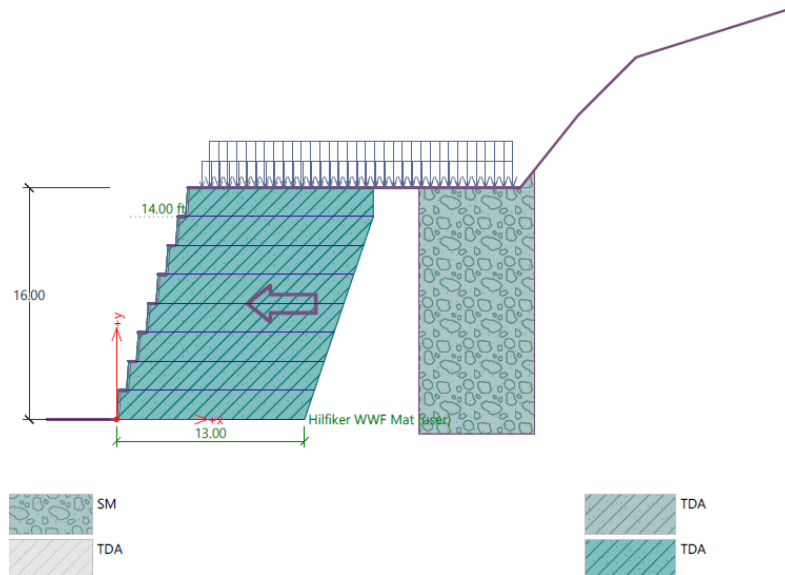
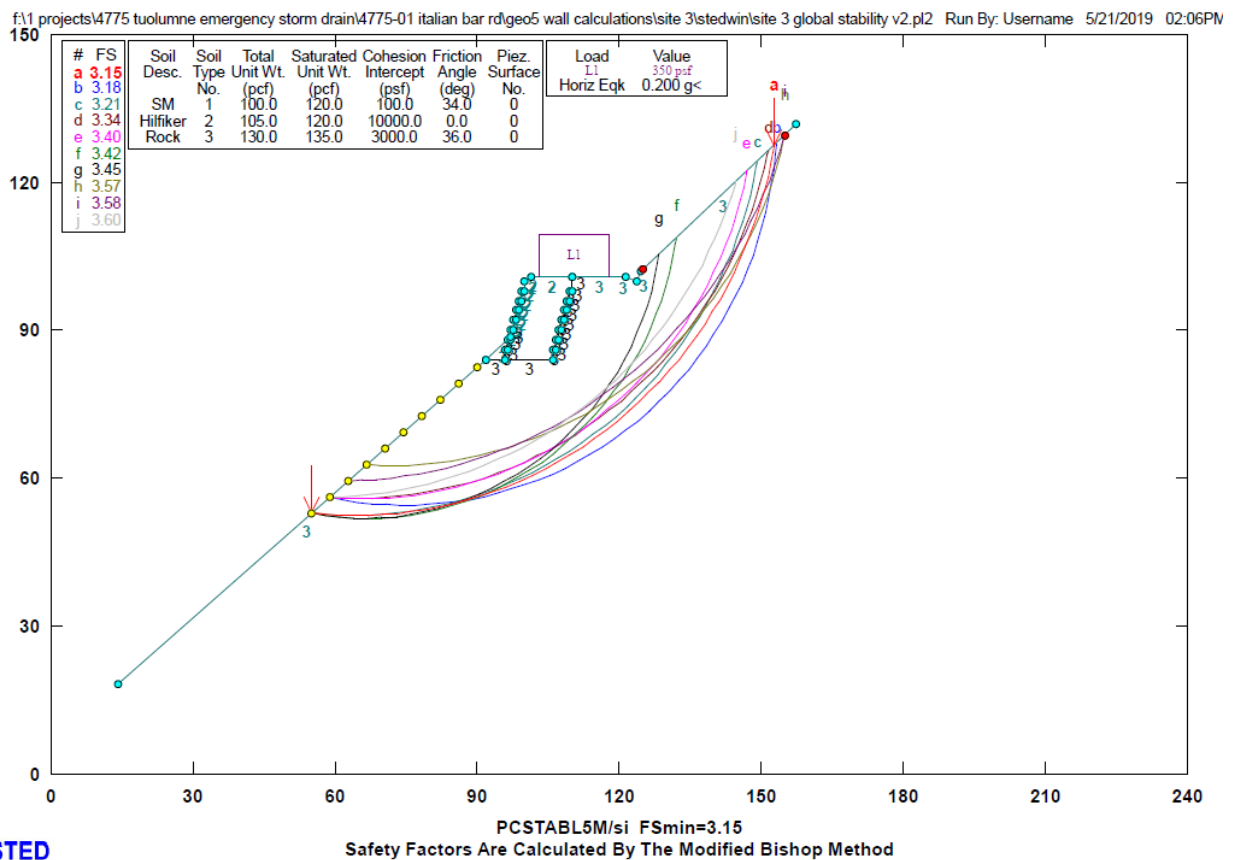


Figure 5.31: Design Calculation of the MSTDA Wall Internal and Global Stability



STED

Figure 5.32: Global Stability Analysis for the MSTDA Wall

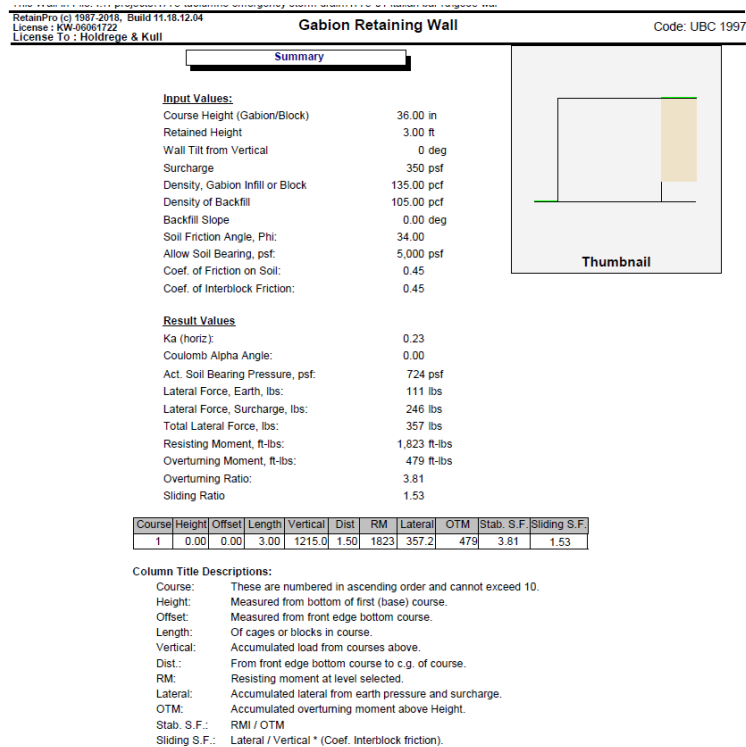


Figure 5.33: Results from the MSTDA Internal and External Stability Checks

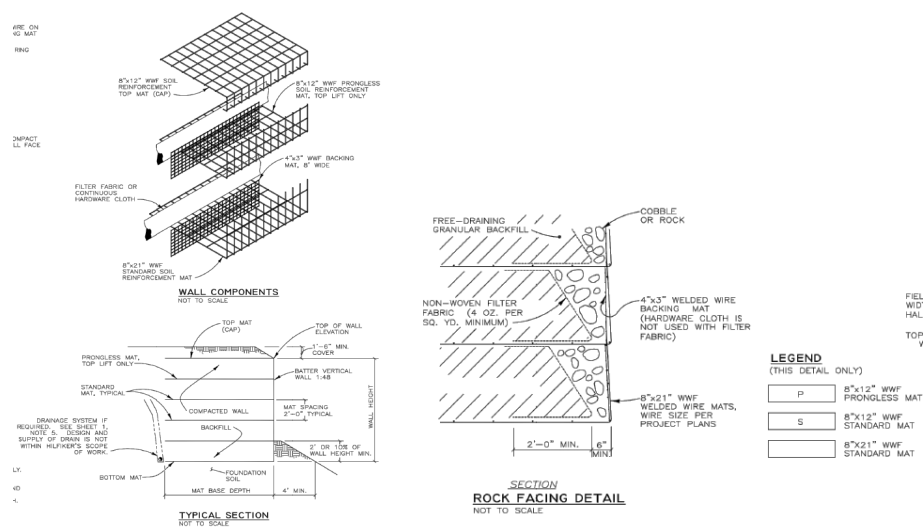


Figure 5.34: Standard Gabion/Reinforcement Details from Hilfiker

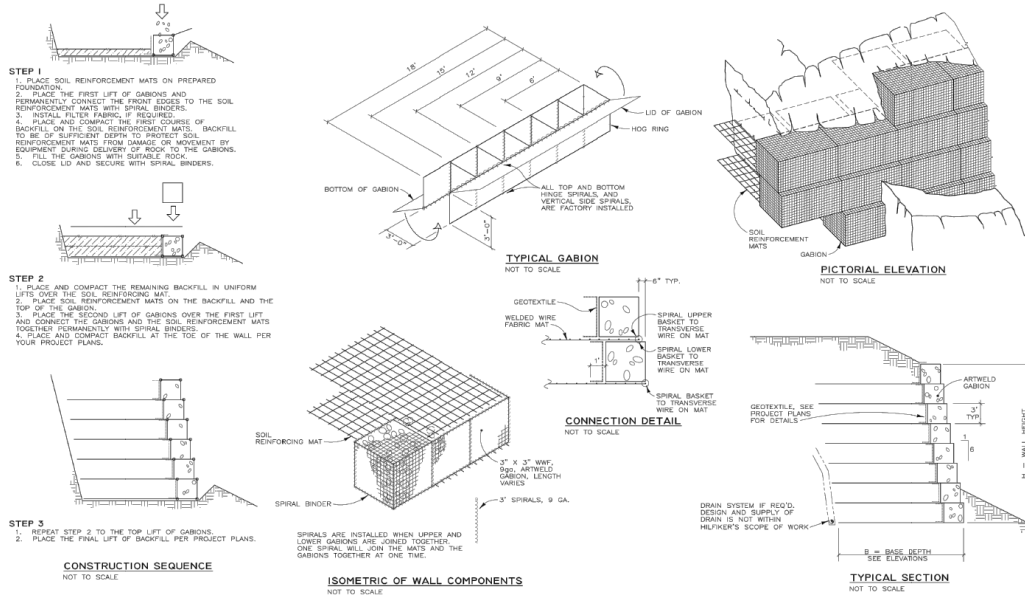


Figure 5.35: Standard Gabion/Reinforcement Details from Hilfiker

Photos of the project are shown in Figure 5.36 to 5.43. The initial site with storm damage on the downslope lane of the road is shown Figure 5.36, the excavation of the existing slope and placement of the first gabion layers is shown in Figure 5.37, and placement of TDA is shown in Figure 5.38. A picture of a nonwoven geotextile separator on the metallic reinforcement layer is shown in Figure 5.39, which implies that TDA interaction with the metallic reinforcements is primarily through friction without interlocking. The rock from the excavation placed at the downhill side of the MSTDA wall is also shown in this picture, which added to the weight on the slope but also increased the embedment of the wall. Placement of the upper layers of TDA and the granular bearing layer are shown in Figures 5.40 and 5.41, respectively, and two views of the final roadway atop the MSTDA wall are shown in Figures 5.42 and 5.43. Due to the embedment of the wall with the excavated rock, the full height of the MSTDA wall is not exposed.



Figure 5.36: Italian Bar Road Site 3 Prior to Construction with Severe Shoulder Erosion



Figure 5.37: Excavation of the Existing Slope



Figure 5.38: Placement of First Lift of TDA



Figure 5.39: Facing Detail of the Metallic Hilfiker Mesh Layers, with Nonwoven Geotextile Atop Metallic Reinforcement



Figure 5.40: Placement of Third Lift of TDA



Figure 5.41: Placement of Granular Bearing Layer



Figure 5.42: Photo of the Completed Wall and Roadway from the West



Figure 5.43: Photo of the Completed Wall and Roadway from the East

Case 3: Italian Bar Road, Site 6 (Tuolumne County, CA)

Another MSTDA wall was constructed at a sixth site on Italian Bar road further from the other five sites in Tuolumne County, CA, also due to erosion of the downslope lane of the road. The location of the site is shown in Figure 5.44. The elevation view schematic of the wall in Figure 5.45 indicates that the MSTDA wall is shorter than that at Site 3. However, as the wall at Site 6 ended up having a greater amount of exposed facing as the downhill side was not fully embedded like at Site 3. A plan view of the improved section is shown in Figure 5.46. The design approach was similar to that at Site 3, including similar material properties assumed for TDA and the use of a Hilfiker welded wire wall design. Typical internal stability and global stability calculations for this MSTDA wall are shown in Figures 5.47 and 5.48, respectively.

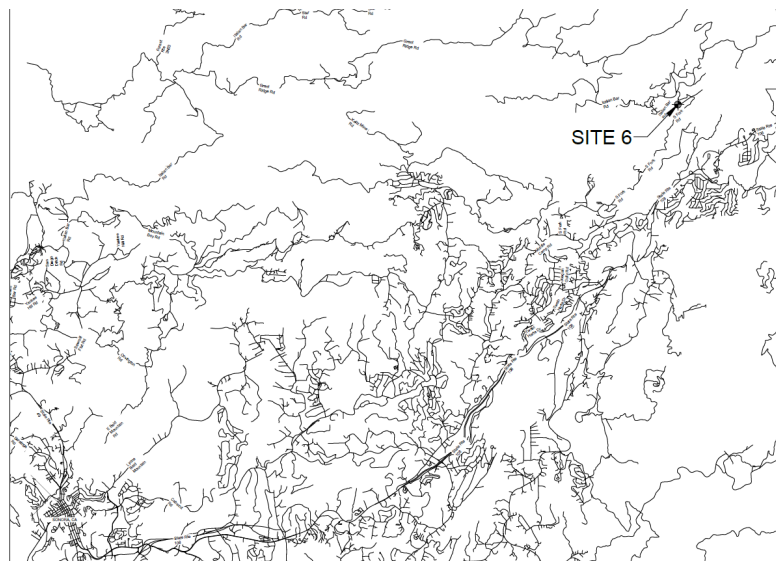


Figure 5.44: Location of Italian Bar Road Site 6 in Tuolumne County, CA

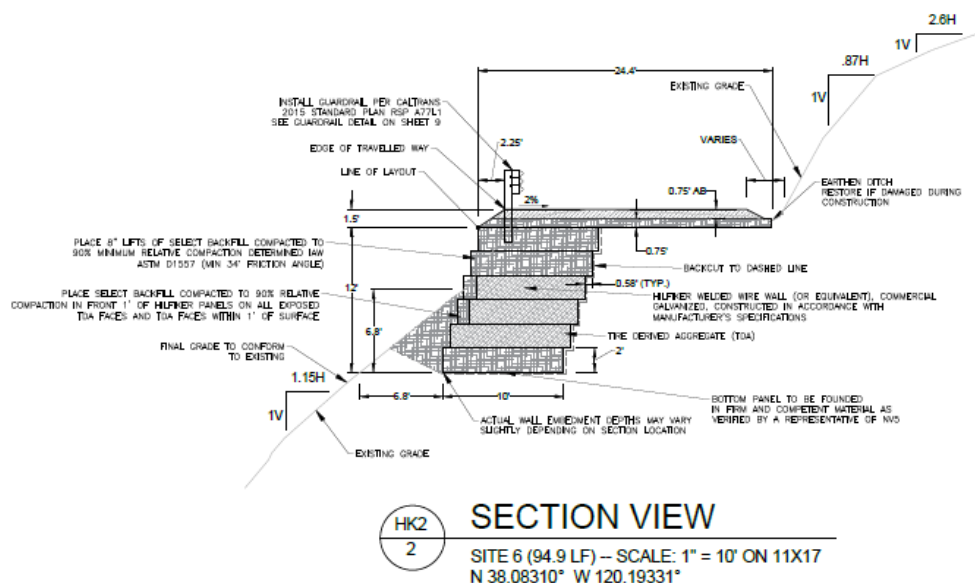


Figure 5.45: Elevation View of the MSTDA Wall at Italian Bar Road Site 6

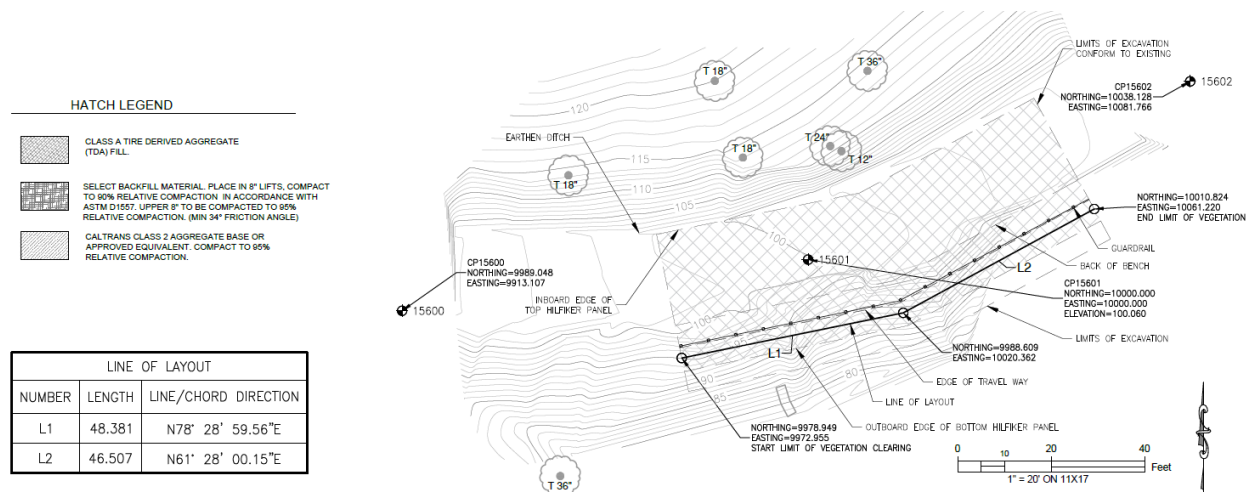


Figure 5.46: Plan View Schematic of the MSTDA Wall

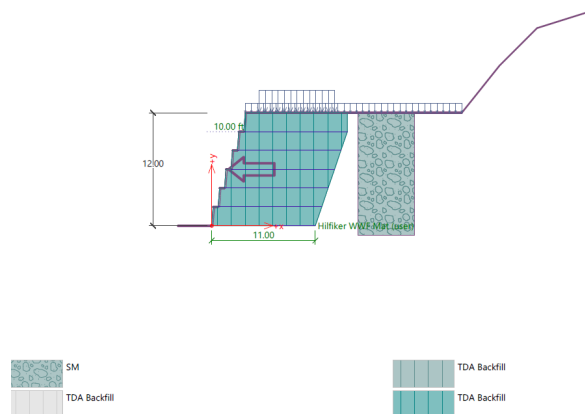


Figure 5.47: Internal Stability Calculations of the MSTDA Wall at Italian Bar Road Site 6

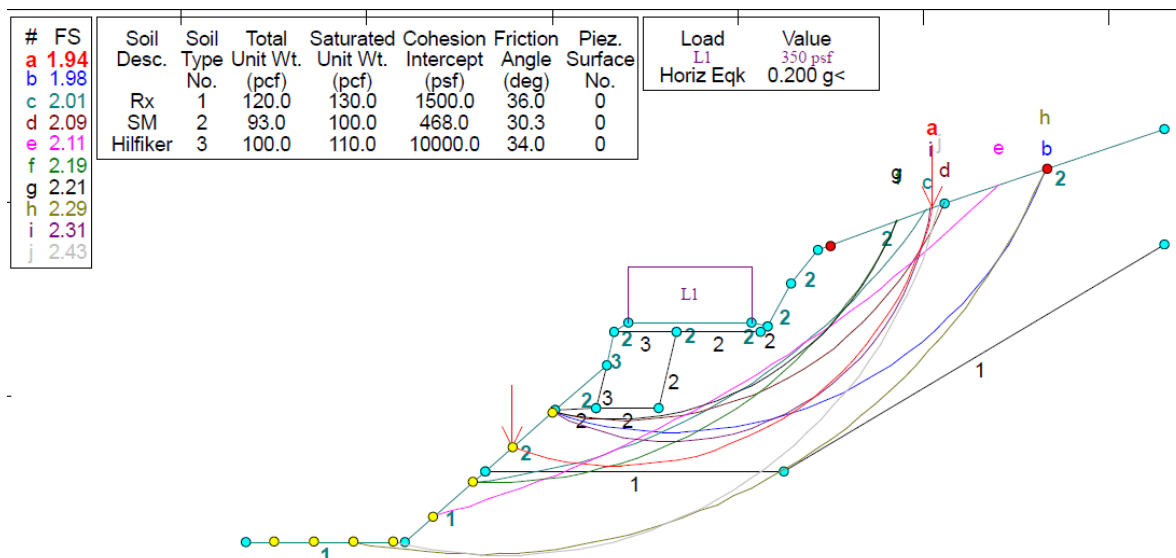


Figure 5.48: Global Stability Calculations for the Wall at Italian Bar Road Site 6

Pictures of the construction process at Italian Bar road Site 6 are shown in Figures 5.49 to 5.58. The initial damage to the road is shown in Figure 5.49, and the excavation of the damaged section is shown in Figure 5.50. Placement of TDA at the site was similar to that in Italian Bar road Site 3, with construction photos shown in Figures 5.50 to 5.55. These figures show how each TDA layer was fully encapsulated with nonwoven geotextile, limiting interaction with the metallic reinforcements. The final MSTDA wall is shown in Figures 5.56 and 5.57, which show how the inclined welded wire mesh layers lead to a smooth wall facing. The final roadway is shown in Figure 5.58, with the guard rail placed within the granular backfill layer of the road.



Figure 5.49: Italian Bar Road Site 6 Before Construction



Figure 5.50: Initial Excavation and Placement of the First Welded Wire Mesh Reinforcement/Facing Unit



Figure 5.50: Placement of the First Lift of TDA



Figure 5.51: Encapsulation of TDA in Nonwoven Geotextile



Figure 5.52: Placement of Gravel Near The Facing



Figure 5.53: Italian Bar Road Site 6 Before Construction



Figure 5.54: Placement of a TDA lift



Figure 5.55: Placement of a TDA lift



Figure 5.56: Final MSTDA Wall at Italian Bar Road Site 6 from North



Figure 5.57: Final MSTDA Wall at Italian Bar Road Site 6 from South



Figure 5.58: Final Unpaved Road atop the MSTDA Wall at Italian Bar Road Site 6 From South Showing Position of the Guard Rail in the Gravel Within the Top Gabion

Chapter 6: Proposed Construction Procedures for MSTDA Walls

This chapter presents the proposed construction process for MSTDA walls based on insights gained from the MSTDA walls constructed in California. These recommended construction procedures are based on a limited amount of information, so it is expected that they will be refined over time as engineers gain more experience with the design and construction of MSTDA walls. Based on the experience from the three MSTDA walls in Chapter 4 and the requirements of the design process in Chapter 3, a summary of the construction stages for MSTDA walls is below:

1. **Prepare subgrade** – remove any organic material, vegetation, and any debris from previous landslides. Perform any ground improvement techniques necessary to address global stability or bearing capacity issues. Level the ground surface and provide embedment if desired - no leveling pad is needed for the wall facing due to the flexibility of gabion facing construction.
2. **Erection of first level of gabions** – place gabions and fill with coarse gravel or cobblestones according to the opening size of the gabions
3. **Placement of subgrade separator** – Placement of nonwoven geotextile along the subgrade to provide separation, and provide overlap with the back of the gabion fill material. An important insight from the MSTDA walls in California is the deployment of separation geotextiles. It is important that the separation geotextile not interfere with the TDA-geogrid interaction. A nonwoven geotextile should be used as the separation layer at the bottom of the wall, at the front and back of the wall, as this will provide both filtration and separation. A short overlap section with the nonwoven geotextile and the geosynthetic reinforcement is permissible near the face of the wall, but this overlap should be less than 0.3 m.
4. **Place and compact TDA** – Place the TDA with target overbuild, and compact
5. **Place reinforcement** – Place the geosynthetic reinforcement atop the TDA and first gabion, the geosynthetic may curve upward due to the overbuild. The reinforcement should be placed so that their principal strength direction is perpendicular to the facing of the wall. The gabion should have sufficient overlap with the gabion fill material to ensure adequate connection strength. It is critical that geosynthetic reinforcements have TDA on both sides without other materials interfering (i.e., geotextile separators). In locations at corners of a wall where two sheets of geosynthetic reinforcement may overlap, TDA should be placed between the reinforcements to avoid direct contact between reinforcements.
6. **Place next level of gabions** – Place the next layer of gabion with desired set-back distance and place the gabion fill material.
7. **Place gabion fill separator** – Place a nonwoven geotextile behind the gabion fill to provide separation with the TDA, but do not overlap with the geogrid.
8. **Place next layer of TDA, compact, and place reinforcement** – Place the TDA with target overbuild, and compact, taking care to ensure no lateral displacement of the gabion, then place the next reinforcement layer.
9. **Continue construction** – Repeat steps 6-7 until reaching the top of the TDA layer
10. **Place top separation/reinforcement layer** – At the top of the TDA layer, place a high-strength woven geotextile atop the TDA and gabion – this woven geotextile will provide separation between the TDA and the overlying granular fill material but will also provide reinforcement at this level.

11. **Place the next gabion layers and granular fill layer in lifts** – Gabion facings will still need to be placed in front of the granular fill material. Place the granular fill layer in lifts, with reinforcements, and add additional gabion layers depending on the granular fill layer thickness.
12. **Driving surface** – Construct the driving surface of the road as necessary
13. **Final details** – Construction of traffic barriers and copings as necessary. The posts for the traffic barriers should ideally be embedded in the granular fill material if it is sufficiently thick. Care should be taken not to damage the reinforcement layers. It may be possible to install the guard rail posts in the gabion fill material.

References

- AASHTO. (2020). LRFD Bridge Design Specifications. 9th Edition. American Association of State Highway and Transportation Officials. Washington, DC.
- Ahmed, I. (1993). Laboratory Study on Properties of Rubber Soils. Report No. FHWA/IN/JHRP-93/4, Purdue University, West Lafayette, Indiana.
- Ahmed, I. and Lovell, C.W. (1993). "Rubber soils as lightweight geomaterials." *Transportation Research Record*. 1422, 61-70.
- Ahn, I., Cheng, L., Fox, P.J., Wright, J., Patenaude, S., and Fujii, B. (2014). "Material properties of large-size tire derived aggregate for civil engineering applications." *Journal of Materials in Civil Engineering*, DOI: 10.1061/(ASCE)MT.1943-5533.0001225, 04014258.
- American Society for Testing and Materials. (2011). ASTM D3080: Standard Test Method for Direct Shear Test of Soils under Consolidated Drained Conditions. ASTM International, West Conshohocken, PA.
- American Society for Testing and Materials. (2019). ASTM C136 / C136M-19: Standard Test Method for Sieve Analysis of Fine and Coarse Aggregates. ASTM International, West Conshohocken, PA.
- Arroyo, M., San Martin, I., Olivella, S. and Saaltink, M.W. (2011). "Evaluation of self-combustion risk in tire-derived aggregate fills." *Waste Management*. 31(9-10), 2133-2141.
- Bernal, A., Salgado, R., Swan Jr., R.H. and Lovell, C.W. (1997). "Interaction between tire shreds, rubber-sand and geosynthetics." *Geosynthetics International*. 4(6), 623-643.
- Bosscher, P.J., Edil, T.B., and Eldin, N. (1993). "Construction and performance of shredded waste tire test embankment." *Transportation Research Record*. 1345, 44-52.
- Bosscher, P.J., Edil, T.B., and Kuraoka, S. (1997). "Design of highway embankments using tire chips." *Journal of Geotechnical and Geoenvironmental Engineering*. 123(4), 295-304.
- Bressette, T. (1984). Used Tire Material as an Alternate Permeable Aggregate. State of California, Department of Transportation, Division of Engineering Services, Office of Transportation Laboratory, Sacramento, CA.
- CalRecycle. (2016). Usage Guide: Tire-Derived Aggregate (TDA). Publication # DRRR 2016-01545. California Department of Resources Recycling and Recovery (CalRecycle). Sacramento, CA.
- CalRecycle. (2017). Report to the Legislature, Five-Year Plan for the Waste Tire Recycling Management Program (Ninth Edition covering Fiscal Years 2017-2018 to 2021-2022). Publication # DRRR-2017-01610. California Department of Resources Recycling and Recovery (CalRecycle). Sacramento, CA.
- CalRecycle. (2019). California Waste Tire Market Report: 2018. Publication # DRRR-2019-1654. California Department of Resources Recycling and Recovery (CalRecycle). Sacramento, CA.
- CalRecycle. (2020). California Waste Tire Market Report: 2019. Publication # DRRR-2020-1691. California Department of Resources Recycling and Recovery (CalRecycle). Sacramento, CA.
- Cerato, A.B. and Lutenecker, A.J. (2006). "Specimen size and scale effects of direct shear box tests of sands." *Geotechnical Testing Journal*, 31(1), 507-516.

- Cheng, D.X., Zhang, K., Cavender, Z., Giles, M., Thor, J., and Joslin, K. (2021). Tire Derived Aggregate Handbook. 3rd Edition. Report to California Department of Resources Recycling and Recovery.
- Christopher, B.R., Gill, S.A., Giroud, J.P., Juran, I., Mitchell, J.K., Schlosser, F., and Dunnicliff, J. (1990). Design and Construction Guidelines for Reinforced Soil Structures: Vol. I. Summary of Research: Vol. II. U.S. Department of Transportation, Federal Highway Administration, Report FHWA-RD-89-043.
- Berg, R.R., Christopher, B.R. and Samtani, N.C., (2009). Design of Mechanically Stabilized Earth Walls and Reinforced Soil Slopes – Volume I. FHWA-NHI-10-024. Federal Highway Administration, Washington, DC.
- Dickson, T.H., Dwyer, D.F., Humphrey, D.N. (2001). "Prototype tire-shred embankment construction." Transportation Research Record, 1755, National Research Council, Transportation Research Board, Washington, D.C. pp. 160-167.
- Duncan, J.M., Byrne, P., Wong, K.S. and Mabry, P. (1980). Strength, Stress-strain and Bulk Modulus Parameters for Finite Element Analysis of Stresses and Movements in Soil Masses. Report No. UCB/GT/80-01, Dept. Civil Engineering, U.C. Berkeley.
- Edil, T.B. and Bosscher, P.J. (1994). "Engineering properties of tire chips and soil mixtures." Geotechnical Testing Journal, 17(4), 453-464.
- El-Emam, M., and Bathurst, R.J. (2007). "Influence of reinforcement parameters on the seismic response of reduced-scale reinforced soil retaining walls." Geotextiles and Geomembranes, 25(1), 33-49.
- Elias, V., Christopher, B.R., and Berg, R.R. (2001). Mechanically Stabilized Earth Walls and Reinforced Soil Slopes Design and Construction Guidelines. U.S. Department of Transportation, Federal Highway Administration, Publication FHWA-NHI-00-043.
- Federal Highway Administration, U.S. Department of Transportation. (1998). User Guidelines for Waste and Byproduct Materials in Pavement Construction. Publication Number: FHWA-RD-97-148.
- Feng, Z.Y. and Sutterer, K.G. (2000). "Dynamic properties of granulated rubber/sand mixtures." ASTM Geotechnical Testing Journal. 23(3), 338–344.
- Finney, B.A. (2018). Exothermic Behavior of Tire Derived Aggregate Fills Subject to Periodic Wetting with Fresh and Saline Water. California Department of Resources Recycling and Recovery (CalRecycle), Sacramento, CA. In Press.
- Finney, B.A. and Maeda, R.K. (2016). Evaluation of Tire Derived Aggregate as a media for Stormwater Treatment. Publication # DRRR-01625. California Department of Resources Recycling and Recovery (CalRecycle), Sacramento, CA.
- Foose, G.J., Benson, C.H., and Bosscher, P.J. (1996). "Sand reinforced with shredded waste tires." Journal of Geotechnical Engineering. 122(9), 760-767.
- Fox, P.J., Thielmann, S.S., Sanders, M.J., Latham, C., Ghaaowd, I., and McCartney, J.S. (2018). "Large-scale combination direct shear/simple shear device for tire-derived aggregate." ASTM Geotechnical Testing Journal. 41(2), 340-353. DOI: 10.1520/GTJ20160245.

- Gebhardt, M.A. (1997). Shear Strength of Shredded Tires as Applied to the Design and Construction of a Shredded Tire Stream Crossing, MS Thesis, Iowa State University.
- Geisler, E., Cody, W.K., and Niemi, M.K. (1989). "Tires for subgrade support." Annual Conference on Forest Engineering, Coeur D'Alene, ID. 1-5.
- Geosyntec. (2008). Guidance Manual for Engineering Uses of Scrap Tires. Prepared for Maryland Department of the Environment. Geosyntec Project No.: ME0012-11.
- Ghaaowd, I., McCartney, J.S., Thielmann, S., Sanders, M. and Fox, P.J. (2017). "Shearing behavior of tire derived aggregate with large particle sizes. I: Internal and concrete interface direct shear behavior." *ASCE Journal of Geotechnical and Geoenvironmental Engineering*. 143(10), 04017078. DOI: 10.1061/(ASCE)GT.1943-5606.0001775.
- Ghaaowd, I., Fox, P.J. and McCartney, J.S. (2020). "Shearing behavior of the interfaces between tire derived aggregate and three soil materials." *ASCE Journal of Materials in Civil Engineering*. 32(6), 04020120.
- Ghaaowd, I. and McCartney, J.S. (2020). "Pullout of geogrids from tire derived aggregate with large particle size." *Geosynthetics International*. 27(6), 671-684. 10.1680/jgein.20.00009.
- Hoppe, E.J. (1998). "Field study of shredded-tire embankment," *Transportation Research Record No. 1619*, Transportation Research Board, Washington, DC. 47-54.
- Humphrey, D.N. (1996). Investigation of Exothermic Reaction in Tire Shred Fill Located on SR100 in Ilwaco, Washington. Report to Federal Highway Administration, Washington, DC.
- Humphrey, D.N., Whetten, N., Weaver, J., Recker, K., Cosgrove, T.A. (1998). "Tire shreds as lightweight fill for embankments and retaining walls." *Prof. Conference on Recycled Materials in Geotechnical Applications*. Geotechnical Special Publication (GSP) 79, ASCE, Reston, Virginia. 51-65.
- Humphrey, D.N., Sandford, T.C., Cribbs, M.M., Gharegrat, H., and Manion, W.P. (1992). *Tire Chips as Lightweight Backfill for Retaining Walls - Phase I*. Report to the New England Consortium, 137 pp.
- Humphrey, D.N. and Manion, W.P. (1992). "Properties of tire chips for lightweight fill." *Grouting, Soil Improvement and Geosynthetics*, R.H. Borden, et al., eds., ASCE, Vol. 2, 1344-1355.
- Humphrey, D.N. and Nickels, W.L., Jr. (1997). Effect of tire chips as lightweight fill on pavement performance." *Proc. 14th International Conference on Soil Mechanics and Foundation Engineering*. Vol. 3: 1617-1620. Balkema, Rotterdam.
- Humphrey, D.N. and Sandford, T.C. (1993). "Tire chips as lightweight subgrade fill and retaining wall backfill." *Symposium on Recovery and Effective Reuse of Discarded Materials and By-products for Construction of Highway Facilities*. Denver, Colorado. 1-20.
- Humphrey, D., Sandford, T., Cribbs, M., and Manion, W. (1993). "Shear strength and compressibility of tire chips for use as retaining wall backfill." *Transportation Research Record*. Transportation Research Board, Washington, DC. 1422, 29-35.
- Jeremić, B., Putnam, J., Sett, K., Humphrey, D., Patenaude, S. (2004). "Calibration of elastic-plastic material model for tire shreds." *GeoTrans 2004*. ASCE. 760-767.
- NAVFAC (1986). *Soil Mechanics Design Manual 7 (DM7)*.

- Lee, K.L., and Seed, H.B. (1967). "Drained strength characteristics of sands." *Journal of the Soil Mechanics and Foundation Division*. SM6, 118-143.
- Lee, J.H., Salgado, R., Bernal, A., and Lovell, C.W. (1999). "Shredded tires and rubber-sand as lightweight backfill." *Journal of Geotechnical and Geoenvironmental Engineering*. 125(2), 132–141.
- Ling, H.I., Leshchinsky, D., Mohri, Y., and Wang, J. (2012). "Earthquake response of reinforced segmental retaining walls backfilled with substantial percentage of fines." *Journal of Geotechnical and Geoenvironmental Engineering*, 138(8), 934-944.
- Mahgoub, A. and El Naggar, H. (2019). "Using TDA as an engineered stress-reduction fill over preexisting buried pipes. *Journal of Pipeline Systems Engineering and Practice*. 10(1): 04018034.
- Manion, W.P. and Humphrey, D.N. (1992). "Use of tire shreds as lightweight and conventional embankment fill, Phase I – laboratory." Technical Paper 9I-I, Technical Services Division, Maine Department of Transportation, Augusta, ME.
- Matsuoka, H., Liu, S., Sun, D., and Nishikata, U. (2001). "Development of a new in-situ direct shear test." *Geotechnical Testing Journal*. 24(1), 92–102.
- McCartney, J.S., Gharaibeh, I., Fox, P.J., Sanders, M., Thielmann, S., and Sander, A. (2017). "Shearing behavior of tire derived aggregate with large particle sizes. II: Cyclic simple shear behavior." *ASCE Journal of Geotechnical and Geoenvironmental Engineering*. 143(10), 04017079. DOI: 10.1061/(ASCE)GT.1943-5606.0001781.
- Skempton, A.W. (1961). "Effective stress in soils, concrete, and rocks." *Pore Pressure and Suction in Soils*. Butterworths, London. 4-16.
- Stark, T.D., Reddy, K.R. and Marella, A. (2010). "Beneficial use of shredded tires as drainage material in cover systems for abandoned landfills." *Journal of Hazardous, Toxic, and Radioactive Waste Management*. 14(1), 47-60.
- Strenk, P.M., Wartman, J., Grubb, D.G., Humphrey, D.N., and Natale, M.F. (2007). "Variability and scale-dependency of tire-derived aggregate." *Journal of Materials in Civil Engineering*. 19(3), 233–241.
- Tandon, V., Velazco, D.A., Nazarian, S., and Picornell, M. (2007). "Performance monitoring of embankments containing tire chips: Case study." *Journal of Performance of Constructed Facilities*. 21(3), 207–214.
- Terzaghi, K. and Peck, R.B. (1948). *Soil Mechanics in Engineering Practice*. John Wiley.
- Tweedie, J.J., Humphrey, D.N., and Sandford, T.C. (1998a). "Full scale field trials of tire shreds as lightweight retaining wall backfill, at-rest conditions." *Transportation Research Record*. 1619, 64-71.
- Tweedie, J.J., Humphrey, D.N., and Sandford, T.C. (1998b). "Tire shreds as retaining wall backfill, active conditions." *Journal of Geotechnical and Geoenvironmental Engineering*. 124(11), 1061-1070.
- USTMA. (2020). 2019 U.S. Scrap Tire Management Summary. U.S. Tire Manufacturers Association. Washington, D.C.

- Xiao, M., Ledezma, M., and Hartman, C. (2013). "Shear resistance of tire-derived aggregate using large-scale direct shear tests. *Journal of Materials in Civil Engineering*. 04014110-1-8.
- Xiao, M., Bowen, J., Graham, M., and Larralde, J. (2012). "Comparison of seismic responses of geosynthetically-reinforced walls with tire-derived aggregates and granular backfills." *Journal of Materials in Civil Engineering*. 24(11), 1368-1377.
- Xiao, Y., Nan, B., McCartney, J.S., and Liu, H. (2019). "Thermal conductivity of sand-tire shred mixtures." *ASCE Journal of Geotechnical and Geoenvironmental Engineering*. 145(11), 06019012.
- Wartman, J., Natale, M.F., and Strenk, P.M. (2007). "Immediate and time-dependent compression of tire-derived aggregate." *Journal of Geotechnical and Geoenvironmental Engineering*. 33(3), 245-256.
- Wu, W.Y., Benda, C.C. and Cauley, R.F. (1997). "Triaxial determination of shear strength of tire chips." *Journal of Geotechnical and Geoenvironmental Engineering*. 123(5), 479-482.
- Wu, P.K., Matsushima, K., and Tatsuoka, F. (2007). "Effects of specimen size and some other factors on the strength and deformation of granular soil in direct shear tests." *Geotechnical Testing Journal*. 31(1), 1- 20.
- Yang, S., Lohnes, R.A., and Kjartanson, B.H. (2002). "Mechanical properties of shredded tires." *Geotechnical Testing Journal*. 25(1), 44-52.
- Zheng, Y., Fox, P.J., Shing, P.B., and McCartney, J.S. (2019). "Physical model tests on half-scale geosynthetic reinforced soil bridge abutments. II: Dynamic loading." *ASCE Journal of Geotechnical and Geoenvironmental Engineering*. 145(11), 04019095.